
Contacting strategies for molecular electronics

Inauguraldissertation

zur
Erlangung der Würde eines Doktors der Philosophie
vorgelegt der
Philosophisch-Naturwissenschaftlichen Fakultät
der Universität Basel

von

Cornelia Nef
aus Schönengrund AR



Basel, 2014

Genehmigt von der Philosophisch-Naturwissenschaftlichen Fakultät
auf Antrag von
Prof. Dr. Christian Schönenberger
PD Dr. Michel Calame
Prof. Dr. Ralf Krupke
Prof. Dr. András Halbritter

Basel, den 24. Juni 2014

Prof. Dr. Jörg Schibler
Dekan

»Woran arbeiten Sie?« wurde Herr K. gefragt. Herr K. antwortete: »Ich habe viel Mühe, ich bereite meinen nächsten Irrtum vor.«

Bertold Brecht

Contents

List of Symbols & Abbreviations	ix
List of Figures	xiii
Introduction	xvii
1. Charge transport at the nanoscale	1
1.1. Conductance of an atomic-sized contact	1
1.2. Quantum tunneling	3
1.3. Molecular junctions	5
1.3.1. A qualitative picture of different transport mechanisms	6
1.3.2. Changing molecular conductance	7
I COMBINING FORCE AND CONDUCTION MEASUREMENTS	9
2. Conducting atomic force microscopy: pulling on molecules	11
2.1. Making contact to a single molecule	11
2.2. Experimental details	13
2.2.1. Setup and sample preparation	13
2.2.2. Data processing	15
2.3. Signatures of single atomic and molecular junctions	16
3. Rupture forces and beyond	19
3.1. Breaking mechanism of atomic and molecular junctions	19
3.2. A statistical analysis to determine the breaking force	22
II GRAPHENE ELECTRODES FOR MOLECULAR ELECTRONICS	29
4. Why graphene is special	31
4.1. The graphene lattice	31
4.2. Band structure and basic electrical properties	32
4.3. Phonons in graphene	34
4.3.1. Heat transport	35

4.3.2. Energy dissipation and electron-phonon scattering	36
5. Chemically vapor deposition of graphene	39
5.1. The principle of chemical vapor deposition	39
5.2. Finding the right growth parameters	41
5.2.1. Copper foil pretreatment	41
5.2.2. Setup and conditions	42
5.3. Transferring the graphene onto a wafer	43
5.4. Characterization of CVD graphene	45
5.4.1. Imaging graphene	45
5.4.2. Transport measurements	46
6. Raman spectroscopy: characterizing graphene	49
6.1. A brief introduction to Raman spectroscopy	49
6.2. Raman active modes in graphene	50
6.3. Temperature dependence of graphene Raman spectra	52
6.4. Additional influences	54
7. pH sensitivity and chemical functionalization	55
7.1. Function principle and experimental setup	55
7.2. Passivation and pH sensitivity	57
7.3. Non-covalent functionalization	58
8. Controlled burning of graphene devices	61
8.1. The idea behind	62
8.2. Sample and electro burning setup	63
8.3. Heating influence on electrical properties	64
8.4. Small gaps in graphene	66
8.4.1. Imaging and Raman spectroscopy	66
8.4.2. Electrical measurements	68
8.5. Temperatures during electroburning	71
9. Towards molecular measurements	75
9.1. Stability and gating	75
9.2. Contacting molecules	77
9.2.1. Experimental conditions	78
9.2.2. Current-voltage characteristics	78
III BACKMATTER	81
10. Summary and outlook	83

Bibliography	85
Appendix A. Mechanically controlled break junction measurements	103
Appendix B. Experimental details of the graphene transfer	105
Appendix C. Experimental setup for Raman spectroscopy	107
Appendix D. Capacitance measurements	111
Appendix E. Cutting graphene with a He-FIB	113
Appendix F. Graphene fusion and switching	115
Appendix G. Level spectrum of the OPE Rod 1 molecule	117
Appendix H. Molecular I-V curves	119
Appendix I. Fabrication protocols	123
Curriculum Vitae	125
Publication list	127
Acknowledgments	129

List of Symbols & Abbreviations

Symbols	
α	Constant
β	Constant
ΔV_{CNP}	Shift of CNP [V]
ℓ_e	Electron mean free path [m]
ℓ_{ph}	Phonon mean free path [m]
$\epsilon_n(k)$	Energy [eV]
Γ	Coupling constant [eV]
γ	Constant
κ	Thermal conductivity [$\text{Wm}^{-1}\text{K}^{-1}$]
λ_Φ	Phase coherence length [m]
λ_F	Fermi wavelength [m]
λ_{inter}	Wavelength at the intersection [nm]
$\langle F \rangle$	Mean force [N]
μ	Mobility [$\text{cm}^2\text{V}^{-1}\text{s}^{-1}$]
μ_L, μ_R	Chemical potential [eV]
ω_0	Frequency shift [cm^{-1}]
$\bar{\Phi}$	Mean barrier height [eV]
\bar{F}_b	Mean breaking force [N]
Φ_b	Barrier height [eV]
ρ	Resistivity [Ω]
σ	Conductivity [S]
τ_j	Relaxation time [s]
Θ_{BG}	Bloch-Grüneisen temperature [K]
ε	Level position [eV]
ξ	Correction factor
A	Amplitude
A_\square	Area [m^2]
C	Capacitance [Fm^{-2}]
C_g	Gate capacitance [Fm^{-2}]
C_j	Heat capacity [$\text{Jkg}^{-1}\text{K}^{-1}$]
C_q	Quantum capacitance [Fm^{-2}]
C_{dl}	Double layer capacitance [Fm^{-2}]
C_{tot}	Total capacitance to the liquid gate [F]
E_0	Phonon energy [eV]
E_F	Fermi energy [eV]
E_{0-0}	Energy of the zero-zero singlet transition [eV]
E_{HOMO}	Position of the HOMO [eV]
E_{LUMO}	Position of the LUMO [eV]
F	Force [N]
$F(x)$	Force distribution function
F_b	Breaking force [N]
f_L, f_R	Fermi distribution
G	Conductance [G_0]
G_s	Sheet conductance [S]
G_{mol}	Molecular conductance [G_0]
G_{sd}	Source-drain conductance [S]
G_{ts}	Tip-sample conductance [G_0]
I	Current [A]
I_0	Optimum intensity [Wm^{-2}]
I_S, I_{AS}	Stokes, Anti-Stokes intensities [Wm^{-2}]
I_{sd}	Source-drain current [A]
J	Current density [Am^{-2}]
k	Wave vector [m^{-1}]

k_c	Force constant of the cantilever [Nm ⁻¹]
k_F	Radius of the Fermi sphere [m ⁻¹]
k_j	Junction force constant [Nm ⁻¹]
L	Length [m]
L_D	Device dimension [m]
N	Number of electrons
n	Charge carrier density [m ⁻²]
$P_{k,\sigma}$	Occupation probability
q	Heat flux density [Wm ⁻²]
q	Wave vector at K [m ⁻¹]
R_s	Series resistor [Ω]
R_{high}	Differential resistance at V_{high} [Ω]
R_{low}	Differential resistance at V_{low} [Ω]
s	Electron spin
sd	Standard deviation
T	Temperature [K]
t	Hopping amplitude
T_{ij}	Transmission probability
U_{SCF}	Charging potential [eV]
V_b	Bias voltage [V]
v_d	Drift velocity [ms ⁻¹]
v_F	Fermi velocity [ms ⁻¹]
V_g	Gate voltage [V]
v_k	Group velocity [ms ⁻¹]
V_T	Threshold Voltage [V]
$V_{+/0}$	Redox potential [V]
V_{CNP}	Reference voltage at which G_{sd} is minimal [V]
V_F	Deflection signal [V]
V_{high}	High bias voltage [V]
V_{low}	Low bias voltage [V]
V_{mod}	Modulation amplitude [V]
V_{off}	Offset voltage [V]
V_{ref}	Electrostatic potential in solution [V]

V_{sd}	Source-drain voltage [V]
W	Width [m]
z	Piezo displacement [m]
z_0	Optimum focus position [m]
z_F	Focus position [m]
z_R	Distance from optimum position with half intensity [m]

Constants

\hbar	Reduced Planck constant = $6.582 \cdot 10^{-16}$ eVs
a	Carbon-carbon bond length ≈ 0.142 nm
c	Speed of light $\approx 3 \cdot 10^8$ ms ⁻¹
e	Elementary charge = $1.602 \cdot 10^{-19}$ C
G_0	Quantum of conductance = $7.75 \cdot 10^{-5}$ S
h	Planck constant = $4.136 \cdot 10^{-15}$ eVs
k_B	Boltzmann constant = $1.381 \cdot 10^{-23}$ JK ⁻¹
m	Electron mass = $9.109 \cdot 10^{-31}$ kg

Chemical Symbols

$(\text{NH}_4)_2\text{S}_2\text{O}_8$	Aluminum persulfate
Al_2O_3	Aluminum oxide
Ar	Argon
Au	Gold
CH_4	Methane
$\text{Cu}_2\text{O}, \text{CuO}$	Copper oxide
Cu	Copper
C8S	Octanemonothiol
$\text{Fe}(\text{NO}_3)_3$	Iron nitrate
$\text{FeCp}2^{+/0}$	Ferrocenium tetrafluoroborate
H_2O	Water

H ₂	Hydrogen	HIBL	Helium-Ion-Beam Lithography
H ₃ PO ₄	Orthophosphoric acid	HIM	Helium Ion Microscope
K ⁺	Potassium ion	HOMO	Highest Occupied Molecular Orbital
KCl	Potassium chloride	ISFET	Ion Sensitive Field Effect Transistor
N ₂	Nitrogen	LA	Longitudinal Acoustic
O ₂	Oxygen	LO	Longitudinal Optical
OH	Hydroxyl	LUMO	Lowest Unoccupied Molecular Orbital
SiO ₂	Silicon dioxide	MCBJ	Mechanical Controlled Break Junction
Si	Silicon	MJ	Molecular Junction
S8S	Octanedithiol	PMMA	Poly-Methyl Methacrylate
Ti	Titanium	RIP	Remote Interface Phonon
Abbreviations			
AFM	Atomic Force Microscope	SAM	Self Assembling Monolayer
ALD	Atomic Layer Deposition	SEM	Scanning Electron Microscope
C-AFM	Conducting Atomic Force Microscope	STM	Scanning Tunneling Microscope
CNP	Charge Neutrality Point	TA	Transversal Acoustic
CNT	Carbon Nanotube	TO	Transversal Optical
CVD	Chemical Vapor Deposition	TSS	Tip-Sample-Separation
DS	Deflection Sensitivity	ZA	Out of plane Acoustic
EB	Electro Burning	ZO	Out of plane Optical
FET	Field Effect Transistor		
GFET	Graphene Field Effect Transistor		

List of Figures

1.1. Schematic conductor, its dispersion relation and occupation of states	2
1.2. Schematics of different tunnel barriers	4
1.3. Schematic of a molecular junction and its energy levels	5
2.1. Contact formation and rupture	12
2.2. Current and force curves for the breaking of a gold-molecule-gold junction	13
2.3. Schematic drawing of the C-AFM setup	14
2.4. Flow chart illustrating the data selection	16
2.5. Representative conductance-distance and force-distance curves for gold-gold and gold-molecule-gold contacts	17
2.6. Two-dimensional histogram from a single molecular junction	18
3.1. Details of force and conductance curves	20
3.2. Spring model and schematic force curve	21
3.3. Schematic force histograms	22
3.4. Two-dimensional conductance force histogram for gold-gold contacts	24
3.5. Two-dimensional conductance force histograms for gold-molecule-gold contacts	25
4.1. Graphene lattice	32
4.2. Band structure of graphene	33
4.3. Phonon dispersion of graphene	34
4.4. Graphene phonon modes	35
5.1. Sketch of graphene formation and CVD oven	40
5.2. SEM images of differently processed Cu foils	41
5.3. Conditions during graphene growth	42
5.4. Optical images of graphene grown at different temperatures	43
5.5. Graphene transfer	44
5.6. Images of graphene on Cu and SiO ₂ recorded with different techniques	46
5.7. Gate behavior of a graphene field effect transistor and schematic device setup	47
6.1. Rayleigh and Raman scattering	50

6.2. Scattering processes responsible for the most common graphene Raman peaks	51
6.3. Raman spectra of graphene	52
6.4. Temperature dependence of the graphene and silicon Raman peak positions	53
6.5. Generation of a electron-hole pair through the absorption of a phonon at different Fermi energies	54
7.1. Schematics of the setup and electrical circuitry of an electrolyte-gated GFET	56
7.2. Transfer curves for a as-prepared GFET at different pH buffer solutions	57
7.3. Transfer curves for passivated and activated GFETs	58
7.4. pH response of GFETs with phenol and fluorobenzene functionalization	59
7.5. Response of a crown ether-functionalized GFET to K^+ ions	60
8.1. Gated dependent current saturation	62
8.2. Shift of the 2D-band versus the distance from a heated graphene constriction	63
8.3. Optical and SEM images of a sample and evolution of the bias voltage during electroburning	64
8.4. Evolution of the differential resistance during the electroburning of graphene	65
8.5. Gate dependent resistance of a GFET before and after heating	66
8.6. Imaging and spectroscopy of the graphene gaps	67
8.7. Tunnel current through a graphene gap	69
8.8. Breaking yield of the electroburning process	71
8.9. Temperature evolution during the electroburning process	72
9.1. Stability of the $I - V$ characteristics of a graphene gap over time	76
9.2. Gate dependence of the $I - V$ curves of a graphene gap	77
9.3. Structure of OPE rod molecule	78
9.4. $I - V$ characteristics of molecules contacted with graphene electrodes	80
A.1. Structure of the (TATA) ² -BP and (TATA) ² -AZO molecules and UV-Vis spectra	103
A.2. MCBJ measurements of the (TATA) ² -BP molecule	104
C.1. Focus dependence of the graphene 2D-band	108
D.1. Schematics of a graphene capacitance device	111
D.2. Frequency dependent impedance measurement	112
E.1. Helium-ion-beam lithography on graphene	114

F.1. Gating and switching behavior in reformed graphene junctions	115
G.1. UV-Vis spectra and electrochemical data of the OPE Rod 1 molecule	117
H.1. $I-V$ curves of different devices exhibiting step-like features attributed to the presence of molecules	120
H.2. Modeled $I-V$ curve using the <i>Unrestricted Broadened One-Level Model</i>	122

Introduction to single molecule electronics

One way to describe molecular electronics is the manipulation of electric signals in devices where organic molecules play an active role. This concept does not only offer miniaturization, but as well new possibilities in the design of functionality. The first concrete model for such a device was proposed by Aviram and Ratner in 1974 [1]. They theoretically discussed a molecule, which should act as a rectifier. Following up on this idea, the field gained a lot of interest, as single molecules would make the smallest possible building block in electronics. The invention of the scanning tunneling microscope (STM) in 1981 by Binnig and Rohrer [2] brought the tool needed to perform the first transport measurements on single molecules [3, 4]. Contacting single molecules with maximum control is still a challenging task, but needed to fully understand the molecules electrical properties and its interaction with the environment.

In the last twenty years, new sophisticated tools to contact single molecules were developed, where mechanically controlled break junctions (MCBJ) [5, 6] and the already mentioned STM are the most common ones. They allow the formation of small contacts with a tunable nanometer-sized gap where single molecules can be trapped. Furthermore, the measurements may be repeated many times and thus large data sets can be collected. This is important, as a molecular junction (MJ) constituted by two atomic contacts and bridged by a single or a few molecules does not form a rigid system, in particular at room temperature. A major challenge consists therefore in understanding and optimizing the arrangement of stable and reproducible contacts. It is known that, for a given molecule, different electrical conductance values can be observed in MJs. This has been attributed to different molecular conformations [7, 8], contact natures, adsorption sides and geometries [8–12] or microscopical arrangements of a few molecules in the junction [13–15]. Also mechanical strain influences the MJ lifetime and stability [16, 17]. To get more insight into these effects, new tools are needed. One technique to gain insight into the contact stability is the conducting atomic force microscope (C-AFM) [18–20]. With it, electrical properties and force can be measured at the same time. This system and measurements concerning gold-gold and gold-octanedithiol-gold junctions is described in detail in [Part I](#).

Until now, gold is the preferred electrode material within the field, as it allows a covalent or coordinative binding of the molecules for several binding groups [21], is inert to the most chemical environments and is easy to handle. Gold however also presents major disadvantages: the relative thick metal electrodes lead to a large screening of a backgate potential; the existence of too many binding geometries leads to ill-defined metal-molecule-metal conductances; and the mobility of surface atoms at room temperature strongly limits the junctions mechanical stability [22, 23]. A particularly promising approach to overcome these issues is based on using carbon nanotubes (CNTs) [24–26] and graphene [27–31] as electrodes. Organic molecules can strongly couple to such electrode systems by $\pi - \pi$ stacking [27, 32, 33] or through covalent bonds [24, 30] and their thickness is similar to the size of the molecules investigated. Graphene is especially interesting, as its planarity will in particular grant an easier access for gating experiments as well as facilitate optical and scanning probe imaging. Furthermore, it can be produced in large scale through chemical vapor deposition (CVD) [34–36] or growth on silicon carbide [37], a prerequisite to gather the large statistics required in molecular electronics investigations. The basic properties of single layer graphene, its production through CVD and the fabrication of nanometer-sized gaps for the use as electrodes in molecular electronics are described in [Part II](#). Furthermore we briefly discuss Raman spectroscopy of graphene, the properties of graphene field effect transistors (FETs) and the first results of using our graphene electrodes to contact molecules.

Charge transport at the nanoscale

Microscopic systems do not always behave as their macroscopic counterparts. One example is the well known Ohm's law, which states that the conductance of a conductor is inversely proportional to its length and directly proportional to its cross section. This is only true above a certain length scale. If the device dimension L_D becomes smaller than the phase coherence length λ_ϕ , we enter the *mesoscopic* regime. Here, quantum interference effects like weak localization can occur, which alter the resistivity. An other important length scale is the mean free path ℓ_e , which is the distance a charge carrier travels before its initial momentum is destroyed. The regime where $L_D \gg \ell_e$ is called *diffusive* and charge transport is mainly limited by elastic scattering of the charge carriers on impurities. When $L_D < \ell_e$, the transport is called ballistic and is only limited by scattering at the boundaries. At even smaller length scales, if $L_D \sim \lambda_F$, where λ_F is the Fermi wavelength, classical or semi-classical arguments do not hold anymore and one has to deal with the full quantum picture [38].

In this chapter we will discuss the electrical properties of nanoscale systems. In particular charge transport through atomic-sized contacts, tunneling barriers and molecular junctions.

1.1. Conductance of an atomic-sized contact

For a contact consisting only of a few or even a single atom the scattering approach [38, 39] can be used to estimate the current flow through it. It is assumed, that the electrodes act as an ideal reservoir with constant temperature and chemical potential, that inelastic scattering is restricted to the electrodes and that phase-coherence is preserved over the entire sample.

In a simplified one dimensional picture we can describe the atomic-sized conductor as a scattering center connected to the electrodes by ballistic leads as shown in [Figure 1.1](#). In the scattering center, a charge carrier of the i -th mode on the left of the conductor is scattered into the j -th mode on the right of the conductor with a certain probability T_{ij} . First we look at a conduction for one pair of modes with

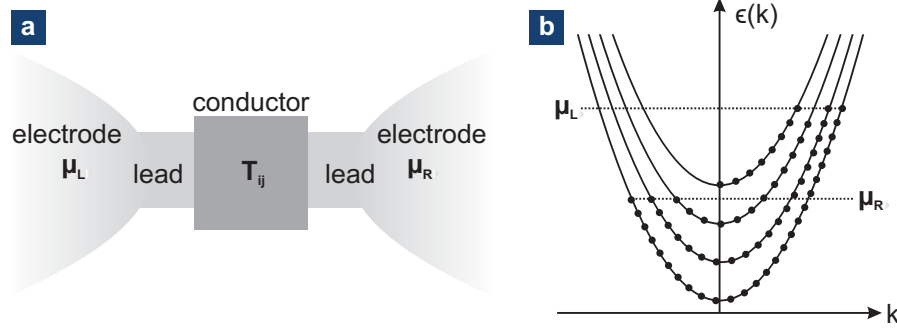


FIGURE 1.1.: **a** A conductor with transmission probability T_{ij} is connected to two contacts with chemical potential μ_L and μ_R by ballistic leads. **b** Dispersion relations and illustration of the occupation of states for different transverse modes. The $+k / -k$ (right moving / left moving electrons) states are filled up to μ_L / μ_R as denoted by the dots.

$T_{ij} = 1$. For one-dimensional electron transport, each electron contributes to the charge density with one elementary charge e per length L . Thus the current I becomes

$$I = \sum_{k,s} \frac{e}{L} P_{k,s} v_k, \quad (1.1)$$

where k is the wave vector, s is the electron spin, $P_{k,s}$ is the occupation probability and v_k is the group velocity of the state. The sum over all allowed states can be replaced by an integral over the energy $\epsilon_n(k)$ multiplied with the k -space density of levels $\frac{L}{2\pi}$ and with $\frac{\partial \epsilon_n(k)}{\partial k} = \hbar v_k$. For an electron to move between the electrodes, there must be filled states on one side and empty states on the other side. The probability for an electron moving from left to right is thus given by $f_L(1 - f_R)$ and the probability for electrons moving from right to the left is given by $f_R(1 - f_L)$, where f_L and f_R are the Fermi distribution of the left and the right electrode respectively. The total current is given by subtracting the current to the right from the current to the left. The over all occupation probability can be rewritten as $P_{k,s} = f_L(\epsilon_n(k)) - f_R(\epsilon_n(k))$ and [Equation 1.1](#) becomes

$$I = \frac{2e}{h} \int [f_L(\epsilon_n(k)) - f_R(\epsilon_n(k))] d\epsilon, \quad (1.2)$$

where h is the Planck constant and the factor 2 is due to spin degeneracy. At low temperature the Fermi distributions can be approximated by Heaviside functions with $f_L(\epsilon) = 1$ below $E_F + \frac{eV}{2}$ and 0 above and $f_R(\epsilon) = 1$ below $E_F - \frac{eV}{2}$ and 0 above, where E_F is the Fermi energy and V_b is the voltage applied between the

contacts. Thus Equation 1.2 leads to

$$I = \frac{2e^2}{h}V. \quad (1.3)$$

Thus the conductance G of a single mode which is fully transparent is $G_0 = \frac{2e^2}{h} \approx 77.5 \mu\text{S}$, which is called the quantum unit of conductance. If more than one mode is populated and transmission occurs with a certain probability, the conductance can be seen as a superposition of the individual modes leading to

$$G = \frac{2e^2}{h} \sum_{ij} T_{ij}. \quad (1.4)$$

The number of conductance channels and their transmission probabilities for a monoatomic contact depend on the valence orbital structure of the material [40]. For gold (Au), one mode with a transmission $T_1 = 1$ was found. Consequently the conductance of an Au contact is $1 G_0$ per atom. If the diameter of an Au contact is decreased atom by atom, a stepwise change of the conductance, with steps $\approx 1 G_0$ is observed [41].

1.2. Quantum tunneling

If two electrodes are separated by a small gap or a thin insulating film a small current will flow, as an electron can tunnel through a potential barrier higher than its kinetic energy with a finite probability. A generalized formula for this effect was proposed by Simmons [42]. His model describes tunneling through a potential barrier of arbitrary shape (see Figure 1.2) by the following formula [42]

$$J = J_0 \left\{ \underbrace{\bar{\Phi} \exp\left(\frac{-2d\beta}{\hbar} \sqrt{2m} \sqrt{\bar{\Phi}}\right)}_{J_L/J_0} - \underbrace{(\bar{\Phi} + eV_b) \exp\left(\frac{-2d\beta}{\hbar} \sqrt{2m} \sqrt{\bar{\Phi} + eV_b}\right)}_{J_R/J_0} \right\} \quad (1.5)$$

$$\text{with} \quad J_0 = \frac{e}{4\pi^2 \hbar d^2 \beta^2},$$

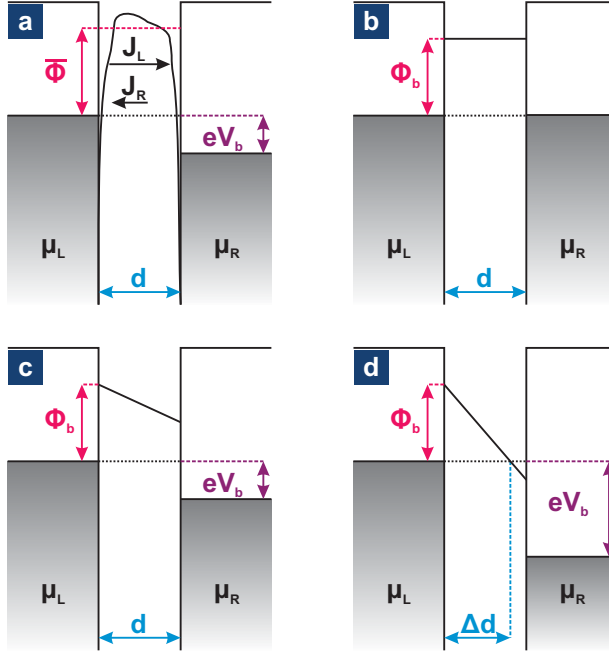


FIGURE 1.2.: Potential barrier with thickness d between two electrodes with the same work function, μ_L and μ_R are the electrochemical potentials. **a** General barrier with the mean height $\bar{\Phi}$ and an applied potential of eV_b . The current density from the left J_L and from the right J_R electrode are shown in Equation 1.5. **b** Rectangular barrier with height Φ_b and $V_b = 0$ **c** $eV_b < \Phi_b$ and **d** $eV_b > \Phi_b$, this leads to an effective barrier width Δd .

where J is the current density, e is the elementary charge, \hbar is the reduced Planck's constant, $\bar{\Phi}$ is the mean barrier height, m is the electron mass, V_b is the potential applied and ξ is a correction factor depending on geometrical details. For many cases $\xi = 1$ is a good approximation and we will neglect it from now on. We assume now a rectangular barrier with height Φ_b and apply a voltage $V_b < \Phi_b/e$. In this case $\bar{\Phi} = \Phi_b - eV_b/2$ and using Equation 1.5 we can calculate the current I as follows

$$I = \frac{A_{\square} e}{4\pi^2 \hbar d^2} \left\{ \left(\Phi_b - \frac{eV_b}{2} \right) \exp \left(\frac{-2d}{\hbar} \sqrt{2m} \sqrt{\Phi_b - \frac{eV_b}{2}} \right) - \left(\Phi_b + \frac{eV_b}{2} \right) \exp \left(\frac{-2d}{\hbar} \sqrt{2m} \sqrt{\Phi_b + \frac{eV_b}{2}} \right) \right\}, \quad (1.6)$$

where A_{\square} is the area of the junction. For small bias, this can be simplified to

$$I \propto V_b \exp \left(\frac{-2d\sqrt{2m\Phi_b}}{\hbar} \right). \quad (1.7)$$

When the bias applied exceeds the barrier height ($V_b > \Phi_b/e$), the barrier changes its shape from trapezoidal to triangular. This is also known as field emission or Fowler-Nordheim tunneling. In this case Equation 1.6 derived above is not valid

anymore and the current is described through [43]

$$I \propto V_b^2 \exp\left(-\frac{4d\sqrt{2m\Phi_b^3}}{3\hbar e} \left(\frac{1}{V_b}\right)\right). \quad (1.8)$$

Thus a plot of $\ln(I/V_b^2)$ versus $1/V_b$ will yield a linear decrease for this regime, but a logarithmic growth for the regime where $V_b \approx 0$. The transition between the two regimes corresponds to the voltage required to change the shape of the barrier from trapezoidal to triangular. This method to deduce it is called transition voltage spectroscopy [43].

1.3. Molecular junctions

An organic molecule normally consist of mainly carbon atoms, arranged in chains or rings with other atoms attached. The overlap of the atomic wavefunctions forms molecular orbitals. Electrons occupy these orbitals according to the Pauli principle. The last filled level is called the HOMO (highest occupied molecular orbital) and the next higher one is called the LUMO (lowest unoccupied molecular orbital). The energy gap in between is called the HOMO-LUMO gap, which size depends mostly on the molecular structure and is typically in the order of a few electron-volts [44].

To form a molecular junction (MJ), the molecule has to be connected to two electrodes. A simple representation of this is shown in Figure 1.3. Here two electrodes are assumed to have continuous (metallic) states and are of the same material. The interaction between the electrodes and the molecule alters the molecular levels. A small charge transfer from the electrode to the molecule can occur, leading to a level shift. Furthermore, the overlap of the molecular orbitals with the dense levels of

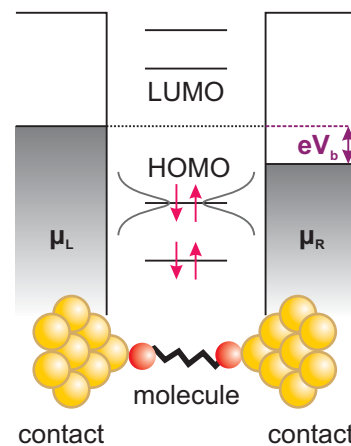


FIGURE 1.3.: Schematic of a molecular junction with the energy levels of the electrodes and the molecule, a small voltage is applied.

the electrodes leads to a broadening of the molecular levels. The strength of this is described by the coupling constant Γ . Applying a voltage leads to a difference of the chemical potential $\mu_L - \mu_R = eV$ and a voltage drop over the junction. If the molecule is conjugated, most of the voltage drop is expected to occur over the contacts [44].

1.3.1. A qualitative picture of different transport mechanisms

The conductance behavior of a molecular junction is dominated by the coupling to the electrodes Γ and the position of the nearest molecular orbital. If either the HOMO or the LUMO is aligned between the chemical potentials of the electrodes resonant transport occurs. Normally this is not the case for small bias voltages, as μ falls in the HOMO - LUMO gap as depicted in Figure 1.3. This allows us to distinguish between non-resonant processes, where the charge is never transferred onto the molecule and resonant processes, where the charge transport occurs over the molecular orbital [44, 45].

Also the different coupling regimes lead to a distinction in transport. For a weak coupling, it is possible to probe the position of the molecular orbital nearest to the chemical potential of the electrodes. To do so a gate is swept, while the bias voltage is held constant. The gate shifts the positions of the molecular levels, but does not affect metallic electrodes. Thus the molecular orbitals can be shifted into resonance. In the strong-coupling regime the electrons can move efficiently from electrode to electrode without localizing on the molecule. In this case no gate dependence will be observed [23]

The combination of these two quantities leads to four basic conductance mechanisms in molecular junctions. However, the transition between them is smooth and also depends on other parameters, like the length of the molecule, bias voltage, charging energies and temperature.

- If the nearest molecular orbital is far from the electrodes potential and the coupling is weak, one can describe the electrical transport through the molecule as *tunneling*. In these junctions resonant transport is difficult to observe as field-induced breakdown occurs before the needed bias is reached [43]. A lower barrier height is observed in comparison with vacuum tunneling as conduction is facilitated through the exponential tail of the level broadening [46]. The conductance of a tunnel junction decreases exponentially with the length of the molecule and is temperature independent [47].
- A higher coupling leads to *molecule-dependent tunneling*. The high Γ leads to a mixing of the molecular orbitals with the electrode levels. For small molecules like hydrogen (H_2) full hybridization can take place and it is not possible any-

more to distinguish between molecule and electrodes. For this case conductance close to one G_0 was observed [48].

- Low coupling, but a molecular orbital close to the chemical potential of the electrodes can be described through *hopping* transport. In this case a small bias can be enough to bring the molecular level into resonance and electrons can move one by one. This leads to a step like characteristic in current versus voltage curves [49, 50]. Hopping transport is thermally activated and thus strongly temperature dependent. Contrary to the tunneling transport it only shows a weak length dependence [47].
- If in addition to a molecular orbital close to the chemical potential of the electrodes the coupling is large, the molecule can be charged easily. A chemical reaction takes place and the molecule gets oxidized or reduced followed by a conformational change. This model is called *polaronic* and could manifest itself through hysteresis in the current-voltage characteristics or the observation of negative differential resistance. [45, 51, 52].

Tunneling and *molecule-dependent tunneling* are 1-step processes. This means that charge transport can be described as a single tunneling process from electrode to electrode. This is favored by small molecules and low bias voltages. On the other hand, *hopping* and *polaronic* transport are 2-step processes, where the charge tunnels from the first electrode to the molecular level followed by a second tunneling step from the molecule to the other electrode. This occurs mainly for large molecules or at high bias.

1.3.2. Changing molecular conductance

For the same molecule, different conductance values can be observed in molecular junctions. This has been attributed to different molecular conformations [7, 8], contact geometries [8, 9] or microscopical arrangements of a few molecules in the junction [13–15]. Force modulations also influence the conduction and the contact stability [16, 53].

Still, there are several possibilities to control the conductance of a MJ in a reproducible way. An important point is the choice of a proper binding group. Ideally, it should not disturb the transport through the molecule, provide a mechanically strong contact and be in electrical contact to the electrodes. Different linker groups [16, 18, 54, 55] as well as direct covalent binding to the gold electrodes [56, 57] were studied. As electrode material, gold is the most common one as its chemical inertness allows measurements under ambient conditions. Other metals like platinum and silver have also been used to create MJs [58–60]. The reactivity of these metals with

oxygen however limits these experiments. Another approach is based on carbon nanotubes (CNTs) [24–26] and graphene [27–30]. Organic molecules can strongly couple to such electrodes by π - π stacking [27, 32, 33] or through covalent bonds [24, 30].

Furthermore, the molecule itself can be designed to have special transport characteristics. Saturated molecules are composed of σ -bonds (consisting of s-orbitals), where the electrons are strongly localized to the carbon atoms [14, 61]. They act as insulators over a wide range of applied voltages. Conjugated molecules contain π -bonds (consisting of p-orbitals). There, the electrons are delocalized and thus the HOMO-LUMO gap is smaller, leading to a higher conductance [62, 63]. Twisted angles in the otherwise conjugated backbone [64] or interference effects [65–67] also influence the conductance of the molecule. Externally, the molecular conductance can be changed by applying an electrostatic [27, 68] or electrochemical [69] gate which shifts the energy levels. The molecular structure can be changed in situ by chemical or light induced [31, 70] reactions.

PART I

**COMBINING FORCE AND CONDUCTION
MEASUREMENTS**

Conducting atomic force microscopy: pulling on molecules

The atomic force microscope (AFM) was developed in 1986 by Binnig, Quate and Gerber [71]. Since then it has become a widely used tool for imaging surfaces, sensitive force measurements and nanomanipulation. Recently, it has also been used to contact single molecules [18–20].

Herein, the experimental details for conducting atomic force microscopy (C-AFM) measurements of gold-gold and gold-octanedithiol-gold junctions are discussed.

2.1. Making contact to a single molecule

Several experimental techniques can be used to contact single molecules, among which mechanically controlled break-junctions (MCBJ) [6] and scanning tunneling microscopy (STM) [4] are the most common ones. To test the electrical properties of the molecule, it is important to identify if a single molecule is contacted, ensure a proper attachment between the molecule and the electrodes and control the environment. For this the break junction method can be used. In the break junction method two tips (in case of the MCBJ) or a tip and a surface (for STM) are moved into contact and then are slowly moved apart from each other. For gold, this retraction leads to the formation of a neck in the material, which can be reduced to a single atom at the end [41]. Figure 2.1 shows a cartoon representation of this process. As discussed in section 1.1, narrowing the contact area atom by atom results in a stepwise reduction of the conductance of the junction, seen as conductance plateaus in conductance versus distance traces.

The same technique can be used with C-AFM to study additionally the mechanics involved in the formation of an atomic contact, as it measures the force and the conductance simultaneously as a function of the distance. It was reported that the force follows a constant slope with relaxations correlated with the stepwise reduction of the conductance [72]. The force at the last conductance plateau is assumed to be

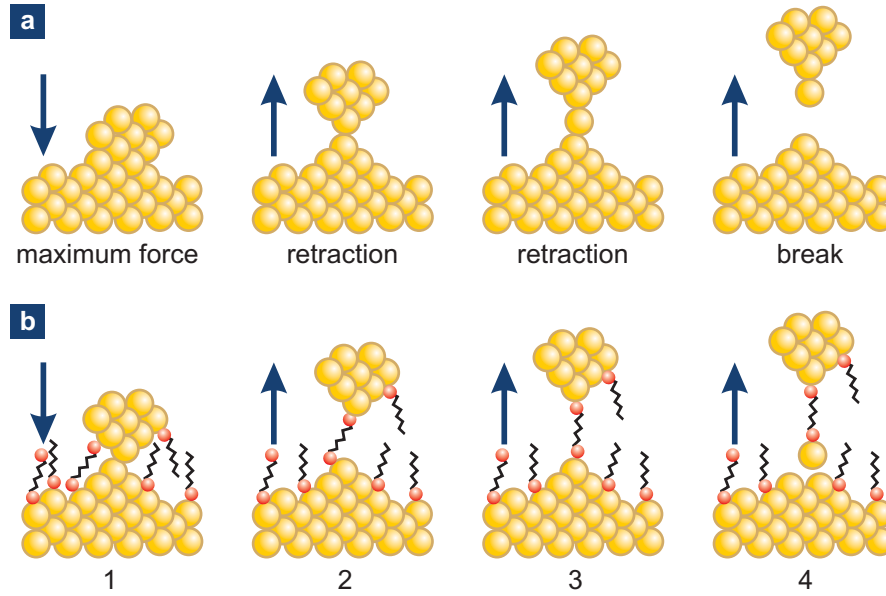


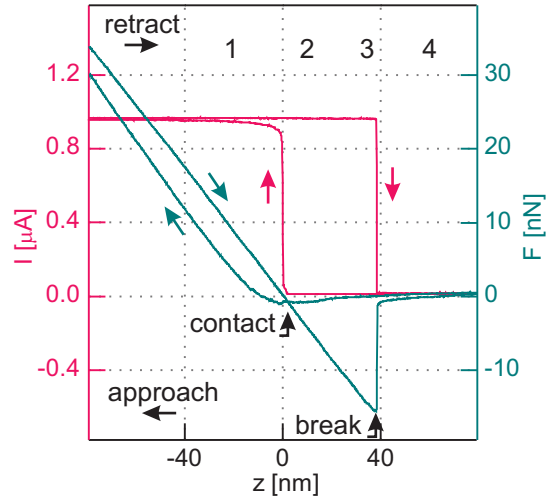
FIGURE 2.1.: Contact formation and rupture in a schematic representation for **a** a gold-gold and **b** a gold-molecule-gold junction.

the breaking force of a single gold-gold atom contact, which was 1.5 nN in agreement with theory [73].

To form molecular junctions, molecules need to be present during the gap formation. This can be achieved by either performing the experiment in a solvent containing the molecules or by preparing a self assembled monolayer (SAM) on one or both electrode surfaces. While a gold-gold contact is formed, molecules with binding groups on both sides can attach to the tip and the substrate **1**. If the tip is further retracted, the gold-gold contact will break, leaving the molecules as the sole bridge between the two electrodes **2**. Further retraction leads to a stretch of the junction **3** and finally it breaks **4** [4]. This is depicted in Figure 2.1. The situation, where one or a few molecules are sandwiched between the electrodes leads to a conductance plateau in the current versus distance measurement, similar to the plateaus observed for gold contacts.

A typical measurement curve is shown in Figure 2.2. The zero of the piezo displacement z (in z direction) is defined as the point where the cantilever touches the surface while not being bent which corresponds to zero force. We now describe the data in more detail, starting with the approach curves for current (pink) and force (turquoise). As long as no contact between tip and sample is established ($z > 0$ nm), the current and the force are below the detection limit. At $z \approx 20$ nm before the contact point, a small dip can be observed in the force curve. We attribute this dip to electrostatic forces between tip and sample possibly caused by the bias voltage ap-

FIGURE 2.2.: Conductance (pink) and force (turquoise) curves for the breaking of a gold-S8S-gold junction. The numbers correspond to the schematics in Figure 2.1. The horizontal axis shows the piezo displacement. The mechanical and the electrical contact form at the same displacement. Note that in the subsequent figures sign convention is reversed and the force in the breaking region is represented with a positive sign. Adapted with permission from [74]. Copyright 2012 Institute of Physics.



plied ($V_b = 10$ mV here). After the contact is established, the force increases linearly with z and the current jumped to saturation, as there is an overload of the amplifier. In this region a gold-gold contact consisting of multiple atoms is established between tip and sample, as schematically depicted by Figure 2.1. Once the preset maximum force is reached, the cantilever is paused for two seconds and then is retracted. A linear force-distance behavior develops again and extends to negative force values due to the adhesion between tip and sample. In this regime atomic junctions and molecular junctions (MJs) can form as described in Figure 2.1. When both electrodes finally come apart, the force and current jump back to zero.

2.2. Experimental details

Two AFM setups were built during my work. Furthermore a protocol for preparing the samples and cantilevers was established. To handle the large amount of data a filtering algorithm was developed.

2.2.1. Setup and sample preparation

The experiments were carried out at room temperature on a commercial instrument (NanoWizard I, JPK Instruments, Berlin, Germany), equipped with a $100 \mu\text{m}$ x and y closed-loop scanner. A second system was set up, but not used for the measurements shown herein, as its force resolution was unsatisfactory (FlexAFM, Nanosurf, Liestal, Switzerland with a $10 \mu\text{m}$ scanner). For both machines the piezo scanner is on the tip side.

A gold (Au) coated silicon (Si) wafer represents the first electrode. This substrate

is functionalized with a SAM, containing octanemonthiol (C8S) to prevent a contamination of the Au surface by the environment. To measure MJs, octanedithiol (S8S) was added, as they are expected to bridge the electrodes [6, 75, 76]. The second electrode is a Au-coated Si cantilever with a nominal force-constant $\approx 4 \text{ Nm}^{-1}$. The chosen force constant is a compromise between the force resolution and the prevention of movement due to thermal activation and the cantilever sticking to the substrate. The thermal movement was estimated using a formula suitable for optical deflection detection [77], resulting in a thermal movement of $\approx 0.37 \text{ \AA}$. This is considerably smaller than the radius of a gold atom ($\approx 1.44 \text{ \AA}$). The cantilever was as well passivated with a C8S SAM. The gold coating is done by e-beam evaporation of a 10 nm titanium (Ti) adhesion layer followed by a 100 nm thick Au layer at a rate of 1 \AA s^{-1} . To protect the freshly coated surface from contamination, the samples and cantilevers were immediately immersed into the functionalizing solution. This solution contains 58 mM C8S in ethanol for the measurements of gold-gold contacts (for passivation) and the C8S experiments and 55 mM C8S and 3 mM S8S for the S8S measurements. The S8S molecules were used as received from Sigma-Aldrich, the C8S molecules were distilled before use. The samples were kept in this solution until the measurements were performed, typically between 12 and 72 hours. Before immersing the samples in mesitylene, wherein the measurements were performed, the samples were rinsed with ethanol thoroughly. The surface of our substrate is relatively rough (root mean square of 1.6 nm over an area of $1 \mu\text{m}^2$) and has a grain size of $\approx 10 - 20 \text{ nm}$, thus we do not expect a full, homogeneous coverage of the SAM [78].

A schematic drawing of the setup is shown in Figure 2.3. During a measurement, the cantilever is pushed towards the substrate with a velocity of $\approx 200 \text{ nms}^{-1}$ until a maximum force of 100 nN for the gold-gold and 15 nN for the gold-S8S-gold contacts is reached. A smaller force for the molecule measurements is used to protect the SAM from a harsh reorganization. The maximum force is maintained for 2 s. Then the cantilever is retracted at a speed of $\approx 15 \text{ nms}^{-1}$ allowing the formation of few atoms or molecules junctions. During the retraction, the force F between the probe and the sample is measured by multiplying the deflection signal V_F of a laser beam focused on the backside of the cantilever with the deflection sensitivity (DS) and the force

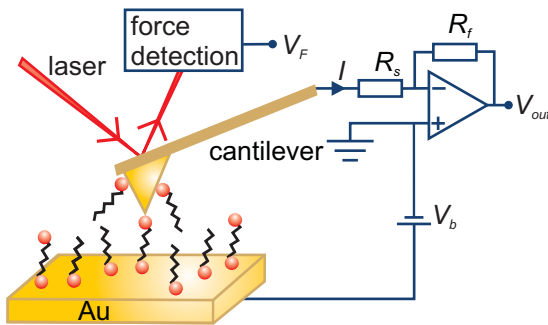


FIGURE 2.3.: Schematic drawing of the C-AFM setup and amplifier. Both the sample and the cantilever are gold coated and functionalized with a SAM. The series resistor R_s has either $R_s = 13 \text{ k}\Omega$ or $R_s = 1 \text{ G}\Omega$, depending on the conductance range, $0.1 - 10 G_0$ or $10^{-6} - 10^{-4} G_0$ respectively. Reproduced with permission from [74]. Copyright 2012 Institute of Physics.

constant k_c of the cantilever. The DS is obtained from the linear regime of a force-distance curve and k_c is determined using the thermal noise method implemented in the AFM system [77]. Simultaneously, the current I through the tip-sample contact is measured with a home-built amplifier and the conductance $G_{tip-sample}$ can be calculated by $G_{tip-sample} = I/(V_b - I \cdot R_s)$, where V_b is the applied bias voltage. The series resistor R_s limits the current flowing through the junction and is needed to prevent the formation of shorts during full contact. This resistor is adjusted depending on the conductance range ($13 \text{ k}\Omega$ for $[0.1 - 10 G_0]$ and $1 \text{ G}\Omega$ for $[10^{-6} - 10^{-4} G_0]$). The bias voltage applied was $V_b = 50 \text{ mV}$ for the gold junctions and $V_b = 100 \text{ mV}$ for the MJs. Typical currents for gold-gold and gold-molecule-gold junctions were in the range of $4 - 5 \mu\text{A}$ and 100 pA respectively, where the detection limits are $0.3 \mu\text{A}$ and 0.8 pA .

2.2.2. Data processing

Because of microscopic structural rearrangements, no contact is like the previous one in atomic and molecular junctions. Large datasets are therefore needed to provide sufficient statistics. We collect between 1000 and 2000 curves at five or more different positions on the substrate per measurement series. A home-written data filtering program based on previous work [79] is used for curve processing. Typically 10 to 20% of the curves pass the filter and are used for further analysis. This system ensures that no systematic bias influences the data through manual selection.

Figure 2.4 shows a flow chart illustrating data treatment flow. The curve processing and filtering macro used, is based on Ref. [79] and is written in IGOR Pro (IGOR Pro 6.0.1.0, Wavemetrics Inc., Portland, OR, USA). Force-distance ($F(z)$) and current-distance ($I(z)$) curves are measured. Both $F(z)$ and $I(z)$ curves are shifted vertically until the final 5% of datapoints (where the cantilever is out of contact), is zero. The z-piezo height is smoothed using a sixth order polynomial. For an AFM the z-piezo height and the tip-sample-separation (TSS) differ, as the cantilever is bent through interactions with the sample surface. The TSS can be calculated by subtracting the corrected metric cantilever deflection from the z-piezo height. To define the contact point (TSS= 0), the average TSS value in the contact area is used. For representation purposes, the $F(z)$ curves are flipped vertically resulting in positive pulling forces and negative pushing forces.

The curves are filtered using the following criteria:

1. The final parts of the $F(z)$ and the $I(z)$ curves in the non-contact area have to be flat (5% of the points). The maximum standard deviation is set to 200 pN for the force and as 5% of the maximum value for the current.
2. A TSS threshold value is defined after which no significant forces are allowed

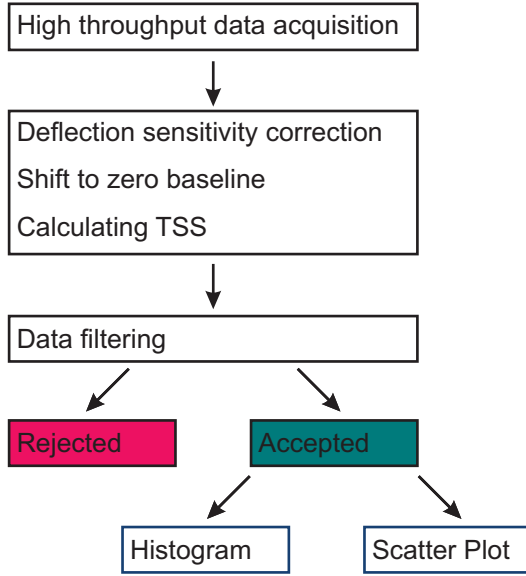


FIGURE 2.4.: Flow chart illustrating the steps of the filtering algorithm applied. Adapted with permission from [74]. Copyright 2012 Institute of Physics.

to occur during pulling (the standard deviation has to be to less than 10%). This value is set to 2 nm, about twice the length of an octanedithiol molecule.

3. During opening cycles, the force has to correspond to a pulling regime until a TSS of 2 nm is reached. This ensures that only traces with a good mechanical contact are analyzed.
4. No or little metal indentation should occur when the tip hits a clean gold surface: the TSS should not be negative. To account for noise and rearrangements of the gold atoms, the threshold is set to -0.5 nm.
5. To ensure electrical contact, a minimum current of 10 times the signal standard deviation has to be reached when the maximum force is applied.

2.3. Signatures of single atomic and molecular junctions

Representative retraction force $F(z)$ and tip-sample conductance $G_{ts}(z)$ curves for gold and S8S samples are shown for the regions of interest in Figure 2.5. The conductance curves $G_{ts}(z)$ show plateaus at multiples of $G_0 = \frac{2e^2}{h}$. Along the plateau, the force curve increases linearly to finish by an abrupt drop corresponding the position where the conductance plateau breaks down. This leads to a sawtooth-like shape for the force curves. Most curves (1-4) show forces between 1 and 2 nN. Curve 5 is an example where no clear plateaus can be observed. Here the maximum conductance is higher ($> 10 G_0$), which means that a larger contact area is present. As a consequence the forces reach higher values (≈ 4.5 nN) as well. If the contact area remains

large during retraction, the cantilever can accumulate more elastic energy. As a consequence, when the contact breaks without a step-wise narrowing of the tip-substrate constriction, larger maximal forces appear in the breaking process [38, 80]. For each curve, the position of the last conductance plateau appearing at G_0 is indicated by a vertical arrow, showing its final z -coordinate before breaking. This corresponds to the situation where the Au bridge is composed of a single Au atom in width [41, 81]. Plateaus appearing at larger conductance values are indicated by arrowheads.

In the presence of dithiolated molecules (Figure 2.5 lower panel), a last conductance plateau is observed at $G_{ts} = G_{mol} \approx 1.1 \cdot 10^{-5} G_0$. Features at lower conductance values are not statistically relevant as will be shown when discussing the histograms for the whole dataset. This plateau is assumed to correspond to the situation where the last molecule bridges the gap between the electrodes and we can interpret the conductance G_{mol} as representative of a MJ where transport is dominated by a single molecule [4]. The conductance thus obtained for octanedithiol is in good agreement with previously reported values [14, 75, 82, 83]. Curve 5 in the lower panel of Figure 2.5 is an example where no plateaus appear in that conductance regime and corresponds to the case where no molecular junction is formed. This occurs in

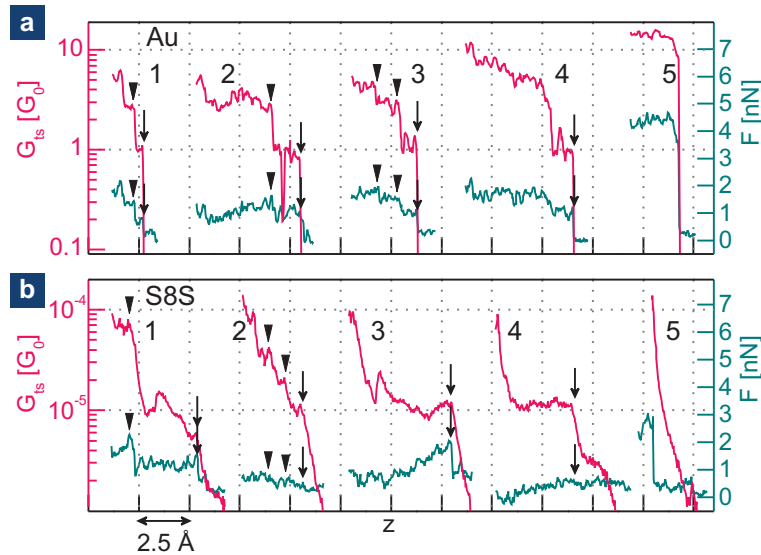


FIGURE 2.5.: **a** Region of interest for typical retraction curves observed on gold samples passivated with a C8S SAM. The tip was pushed on the surface with a maximum force of 150 nN. **b** Characteristic curves of samples covered by a S8S SAM. The maximum pushing force was 15 nN to avoid large disturbance in the SAM. The curves are separated from each other by an offset in the z -direction. Plateaus at multiples of a certain conductance, ($G_0 = \frac{2e^2}{h}$ for **a** and $G_{mol} = 1.1 \cdot 10^{-5} G_0$ for **b** occurring coincidentally with jumps in the force curves are marked with arrows and arrowheads (multiples). Adapted with permission from [74]. Copyright 2012 Institute of Physics.

about 40% of the curves. If we now focus on the force traces, we observe that except for curve 3, the slope is smaller than the calibrated force constant of the cantilever $k_c = 4.2 \text{ Nm}^{-1}$ and no clear jumps are observed. It is known, that a breakdown of the junctions can occur spontaneously at room temperature [76], without the application of an external force. This seems to be the case for most of the measured curves. However we also note that for about 20% of the conductance curves showing conductance plateaus, the force is first constant (on average) and then rises linearly until it drops down at the position corresponding to the end of the conductance plateau. Curve 3 in Figure 2.5, lower panel is representative for this scheme. We will further analyze this type of curves in section 3.1.

While simple histograms built from individual curves give a useful overview, they do not show how force and conductance relate to each other. Two-dimensional histograms (scatter plots) help to visualize this interplay. They are built by binning both, the conductance and the force range. The corresponding bin sizes are $\Delta F = 100 \text{ pN}$ for the force data and $\Delta G_{ts} = 0.05 G_0$ for the gold-gold conductance data and $\Delta \log(G_{ts}/G_0) = 0.02$ for the MJs conductance data. For the gold-molecule-gold junction data a logarithmic scale was chosen to better visualize the conductance peak [84]. In these histograms, we concentrate on the stretching regime, which means that only conductance points with a corresponding positive force are represented. Each point in the measured curves contributes a count in the bin belonging to its conductance and corresponding force value. As an example, a scatter plot for a single curve (curve 3 in Figure 2.5 lower panel) is shown in Figure 2.6. The top and right panels show one-dimensional conductance and force histograms respectively. A clear peak at $1.1 \cdot 10^{-5} G_0$ is observed in the conductance histogram and emphasized with a Gaussian fit. The solid force histogram shows the overall histogram minus the background (force values from $2 \cdot 10^{-6} G_0$ to $8 \cdot 10^{-6} G_0$). A cluster in the two-dimensional histogram shows us if a certain conductance is favored, as for a single molecule contact, and at which force it occurs.

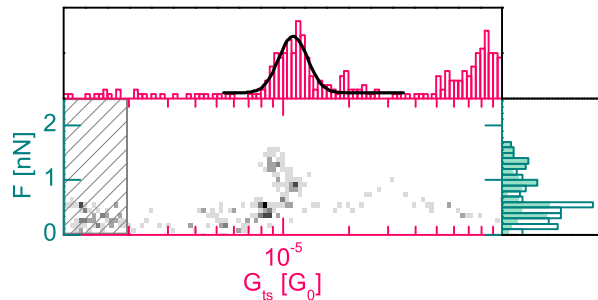


FIGURE 2.6.: Two-dimensional histogram for a single MJ curve (Figure 2.5 curve 3, lower panel). For the solid histogram, the background was subtracted. A Gaussian fit to the conductance peak is shown. Adapted with permission from [74]. Copyright 2012 Institute of Physics.

Rupture forces and beyond

Measuring the force acting on a junction in parallel to the current through the junction allows us to determine the breaking force of the system. In this chapter we show how we deduce the breaking force for atomic and molecular junctions and suggest a breaking mechanism for the formation of MJs. For this we use the two-dimensional histograms introduced in [section 2.3](#)

3.1. Breaking mechanism of atomic and molecular junctions

To get an idea of the differences in the breaking mechanisms of atomic and molecular junctions, we first concentrate on single curves. [Figure 3.1](#) shows curve 2 from the top panel and curve 3 from the bottom panel of [Figure 2.5](#).

For an atomic contact the average slope of the force curve $F(z)$ during a conductance plateau (shaded gray area) corresponds to the calibrated force constant of the cantilever ($k_c = 3.2 \text{ Nm}^{-1}$ for this experiment, dashed black line). This means that, upon retraction, the tip-sample-separation (TSS) stays constant and only the cantilever is bent. The right panel shows the force distribution for $F(z)$ during the last conductance plateau at $1 G_0$. For a noiseless, linearly increasing force vs distance curve, the distribution should be flat. The noise in the curve leads to a trapezoidal shape for the distribution, instead of a sharp cut off, as shown by the solid line in [Figure 3.1](#). The counts enclosed by the solid line is equivalent to the counts in the histogram. The distribution is symmetric around the mean force, which is denoted by $\langle F \rangle$. An open star symbol (\star) shows its position along the force trace $F(z)$. The breaking force F_b corresponds to the maximum force reached immediately before a sharp drop in conductance and is observed at the end of the last conductance plateau. F_b is indicated by a solid star symbol (\star) in the conductance trace. We denote the breaking force as the maximum force minus the standard deviation (sd) of the force noise along the conductance plateau. For this particular curve we obtain $F_b \approx 1.2 \text{ nN}$ for a gold-gold contact, slightly below the 1.4 nN [20] and 1.5 nN [72, 85] found in earlier experiments and slightly above the calculated forces of 0.9 nN [86] and 1.1 nN [87]. Note that this is the breaking force obtained from a single $F(z)$ curve. In the

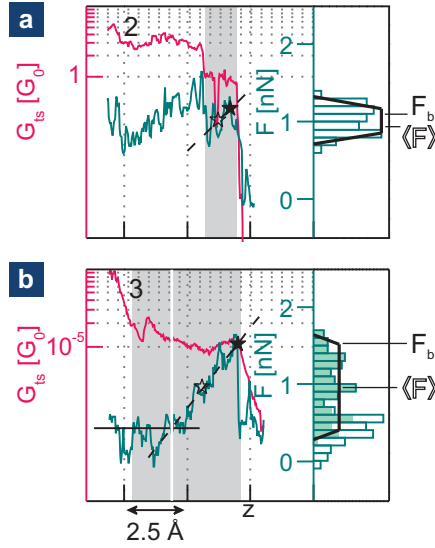


FIGURE 3.1.: **a** Details of curve 2 from Figure 2.5 top panel and **b** curve 3 from Figure 2.5 bottom panel. The dashed line shows the force constance of the cantilever, the solid line is horizontal. Gray areas emphasize the distance intervals corresponding to the last conductance plateaus. On the right, histograms show the force distribution corresponding to the gray areas. Adapted with permission from [74]. Copyright 2012 Institute of Physics.

discussion of Figure 3.4 below, we will provide a statistical analysis over ensembles of conductance and force traces.

MJs show a different behavior. Most of the force curves show a slope smaller than the calibrated force constant of the cantilever and no clear jumps in the force are visible. But $\approx 20\%$ of the curves (as already mentioned in section 2.3) show first a constant force, followed by a linear increase and a break at exactly the position where the conductance plateau ends. We will now discuss one of this curves in detail (Figure 3.1 lower panel). The extension of the last conductance plateau is emphasized by a grey shaded area. In the corresponding force curve, the vertical line shows the limit between a regime where the force remains constant on average (solid line) and a regime where it increases linearly (dashed line). The mean force constant in the linear regime obtained from a fit to the data is $k_c = 4.1 \pm 0.2 \text{ Nm}^{-1}$. Remarkably, this slope corresponds to the cantilever force constant k_c (dashed line) which was $k_c = 4.2 \text{ Nm}^{-1}$ in this measurement. The force histogram (right panel) was obtained from the force trace in the distance interval corresponding to the conductance plateau. The linear force region leads to a large force peak close to zero, whereas the linearly increasing regime (solid histogram) leads to a trapezoidal force distribution. In analogy to the analysis done for gold-gold contacts, we deduce a mean force (\star) and breaking force (\blackstar) from the linearly increasing regime of the $F(z)$ trace. We obtain in this case a breaking force $F_b \approx 1.5 \text{ nN}$, close to the value observed for Au-Au contacts.

To gain further insight in the mechanics of junction formation, we can look at the setup as a simple series connection of two springs (Figure 3.2 top left panel). The first spring is the cantilever with a spring constant k_c , the second spring, k_j represents either the atomic gold-gold contact or the molecular junction (Au-molecule-Au). k_c is known and assumed to be constant over the measurement. Thus, what we measure depends solely on k_j . If $k_j \gg k_c$ the $F(z)$ trace has a slope of exactly k_c , else if

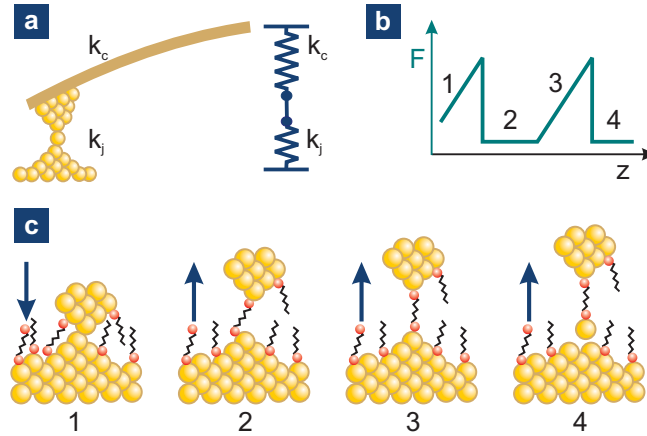


FIGURE 3.2.: **a** Spring model for the cantilever and the contact. **b** Schematic force curve corresponding to the steps depicted in Figure 2.1. **c** Contact formation and rupture for a gold-molecule-gold junction. Adapted with permission from [74]. Copyright 2012 Institute of Physics.

$k_j \ll k_c$ no force increase is observed. For cases in between these two extremes a slope of the $F(z)$ trace smaller than k_c is expected.

The breaking mechanism for gold-gold junctions has been described as a stepwise reduction in conductance correlated with relaxations in the force [72, 85]. Our measurements agree well with these earlier findings. In the following discussion, we focus on MJs. The general case where the slope of the force trace is smaller than k_c is difficult to assess given the large number of possible microscopic arrangements. However, for force traces such as that shown in Figure 3.1 lower panel, the situation is more favorable: we propose that a rearrangement of the molecule takes place during the pulling of the cantilever, as depicted in Figure 3.2 lower panel. A corresponding schematic force trace is shown in Figure 3.2 top right panel. At point **1** the tip is still in contact with the sample, while molecules can already bind covalently to both electrodes [88]. When the gold bond breaks, the molecule is not necessarily fully stretched in the junction and the force will decrease: we enter regime **2**. As the cantilever is further retracted, the molecule will migrate and align itself between the Au contacts. Based on our data, we speculate that the migration process does not require a substantial force. At room temperature the surface gold atoms are mobile: Au-bound molecules without a strong local molecular ordering will therefore also be mobile. Upon stretching, we can thus anticipate a migration of the molecules to the narrowest part of the junction without the need for a substantial extra mechanical force. This scenario is also supported by recent calculations showing the large mobility of a molecular phase adsorbed on Au atomic contacts due to the fluctuations of the atomic positions in the narrowest part of the contact [89]. In this regime, any unstretched molecule will act as a very soft spring. Once the narrowest position

between electrodes is reached, the molecule will fully extend and a further retraction of the cantilever lead to a linear increase of the force **3**. We observe that the slope corresponds to k_c . This means that the junction composed by the metal contacts and the stretched molecule is now behaving as a stiffer spring than the cantilever. Once the breaking force is reached, the cantilever separates from the substrate and the force goes back to zero **4**.

3.2. A statistical analysis to determine the breaking force

As already emphasized in [section 3.1](#), the linear part of a force curve leads to a trapezoidal force histogram. If we neglect the force noise, the distribution is flat. For the MJs this leads to a rectangular histogram, which extends from zero to the breaking force F_b . In case of the atomic junctions the histogram starts at a higher value, as a certain force is needed to establish a monoatomic contact. The number of counts (height) of the histogram depends on the sampling rate and the slope of the force curves. For the atomic contacts the slope nicely follows k_c and thus is constant. For the MJs this is only true for 20% of the cases as discussed in [section 3.1](#). On the other hand, the breaking force is only reached for this special cases and the others only contribute to the background at low values in the force histogram. For a data set, where many force curves contribute, the overall force histogram is constituted by a sum of many such rectangular histograms with distinct breaking forces F_b . A schematic of a force histogram over many curves is shown in [Figure 3.3](#) for atomic and molecular junctions. The turquoise rectangles show the values corresponding to regions in the $F(z)$ curves where $k_j \gg k_c$. The background coming from the other regions is shown in blue. For a normally distributed breaking force, the overall distribution function $F(x)$ follows the integral of a Gaussian distribution:

$$F(x) = \frac{A}{\sqrt{2\pi}sd} \int_{-\infty}^x e^{-1/2\left(\frac{t-F_b}{sd}\right)^2} dt \quad (3.1)$$

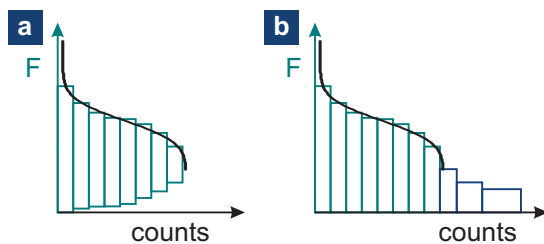


FIGURE 3.3.: Schematic for histograms for **a** atomic and **b** molecular junctions. The turquoise rectangles show the values corresponding to regions in the $F(z)$ curves where $k_j \gg k_c$. The background coming from the other regions is shown in blue.

where A is the amplitude, \overline{F}_b is the mean value and sd is the standard deviation. Introducing the error function (erf), we can write:

$$F(x) = \frac{A}{2} \left[1 + \operatorname{erf} \left(\frac{x - \overline{F}_b}{\sqrt{2}\sigma} \right) \right] \quad (3.2)$$

The fitting parameters are the amplitude A , the mean breaking force \overline{F}_b and its standard deviation sd . $F(x)$ is fitted to the force histograms derived from the whole data set. The upper limit of the fit is the maximum force reached in the histogram. To avoid the regions before an atomic junction is formed and with large background for MJs, we restrict the fit to the upper flank of the force histogram with a limit set to 0.7 nN. Note that the fit is robust with respect to this lower limit: the resulting value for \overline{F}_b varies by less than the standard deviation when the limit is changed by as much as ± 0.3 nN.

We first focus on the data for gold-gold contacts in [Figure 3.4](#). This scatter plot is built from 194 curves. The data shows a clear cluster in the scatter plot and a peak in the conductance histogram at $\approx 0.95 G_0$ (mean of a Gaussian fit to a log-normal distribution [[62](#)]). The value is slightly lower than the conductance quantum $1 G_0$ which can be attributed to a small resistance in series arising from wires and contacts [[38](#), [90](#)]. While less clear than at $1 G_0$, a clustering around $\approx 2 G_0$ and $3 G_0$ can still be seen, arising from the conductance plateaus visible in the individual conductance traces ([Figure 2.5](#)). The force histogram on the right panel (open bars) includes all forces corresponding to data points with a conductance between $0.25 G_0$ and $5 G_0$. The second force histogram (solid bars) corresponds to a conductance range extending from $0.5 G_0$ to $1.5 G_0$ where atomic contacts with a single Au atom are formed. The crosshatched region to the left of the scatter plot is not taken into account for the force histograms. The threshold corresponds to the conductance noise level. Fits of [Equation 3.2](#) to the upper flank of the force histograms for the overall ($0.25 G_0$ to $5 G_0$) and plateau ($0.5 G_0$ to $1.5 G_0$) regions are shown in [Figure 3.4](#) top panel. Histograms and corresponding fits for different conductance ranges are shown in the lower panel of [Figure 3.4](#). Each histogram belongs to interval of an integer value of $G_0 \pm 0.5 G_0$. The open star symbols in the upper panel indicate the position of the corresponding mean breaking force \overline{F}_b plotted at the mean conductance value. The error bars correspond to the standard deviation. We note that the distribution of \overline{F}_b broadens (increase in standard deviation) with increasing conductance while \overline{F}_b itself only grows slightly. At higher conductance more atoms contribute to the contact and larger forces can appear. From the scatter plot and the corresponding force histogram, we can thus estimate the average breaking force \overline{F}_b more easily than by analyzing all individual traces. Using the procedure described above and for the force histogram corresponding to conductances ranging between $0.5 G_0$ and $1.5 G_0$, we obtain $F_b = 1.45 \pm 0.23$ nN in good agreement with values reported experimentally

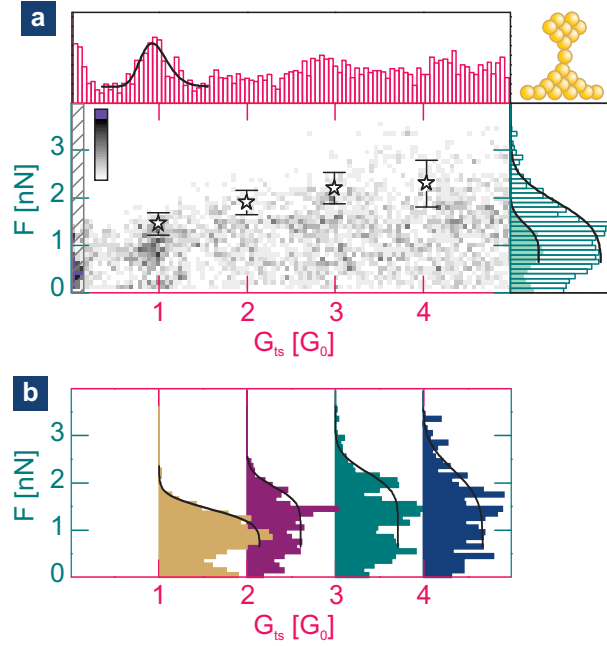


FIGURE 3.4.: **a** Two-dimensional normalized histogram providing an overview over tip-sample conductance G_{ts} and force F for gold-gold contacts (194 curves). The conductance (top panel) and force (right panel) 1D normalized histograms corresponding respectively to the full conductance and force ranges are shown as well. An open star symbol shows the mean breaking force \bar{F}_b for conductance intervals extending $\pm 0.5 G_0$ around multiples of G_0 . The 1D force histogram corresponding to the first conductance interval is shown as solid bars in the left panel. The histograms corresponding to the other intervals are shown in **b**. Adapted with permission from [74]. Copyright 2012 Institute of Physics.

for gold-gold contacts [20, 72, 85].

Figure 3.5 shows a scatter plot for octanedithiols (S8S, upper panel, 115 curves) as well as control measurements with only octanemonothiols (C8S, lower panel, 114 curves) together with the corresponding conductance and force histograms. The conductance histograms, force histograms and scatter plots are normalized to the number of data curves and shown at the same scale. We first consider the data for octanedithiols (S8S) in the upper part of the figure. A clear peak in the conductance histogram can be seen close to $10^{-5} G_0$ which corresponds to the last conductance plateau observed in individual conductance traces. A fit to a log-normal distribution [62] provides a conductance $G_{ts} \approx G_{mol} = 1.1 \cdot 10^{-5} G_0$ which we interpret as a characteristic value for the molecular junction. The force histogram built from the data over the whole conductance range above noise threshold (open bars) does however not show a clear peak but rather a shoulder at around 1 nN. Looking at the scatter plot helps better understanding the correlation between force and conductance during the breaking of the junction. At low conductance values, the force mostly

remains below 0.7 nN (dashed line). For conductance values larger than $\approx 0.8 G_{mol}$, we clearly see that the maximum force can reach higher values as emphasized by the second horizontal dashed line at 1.6 nN. The two regions are also indicated by the arrows in the conductance histogram. The forces of the conductance region below $0.8 G_{mol}$ result in a shoulder in the force histogram (arrow). The higher force values above $\approx 0.8 G_{mol}$ can be attributed to the formation of MJs. The mean force in the background region (from $2 \cdot 10^{-6} G_0$ - $8 \cdot 10^{-6} G_0$) is 0.3 ± 0.4 nN (open diamond). The second force histogram in the right panel (solid bars) is obtained by subtracting the histograms corresponding to the two conductance intervals: below and above $0.8 G_{mol}$, it is also shown in Figure 3.5 lower panel in turquoise. Both histograms

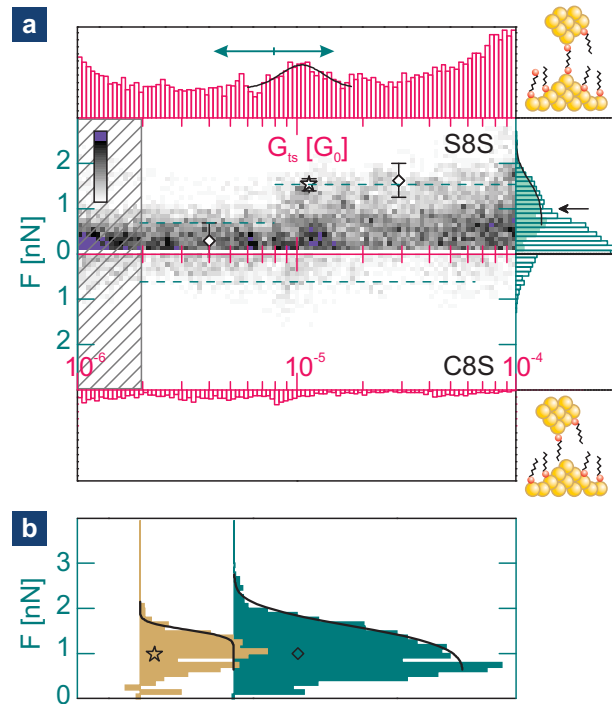


FIGURE 3.5.: **a** Two-dimensional normalized histogram providing an overview over tip-sample conductance G_{ts} and force F for gold-octanedithiol-gold junctions (upper panel 115 curves) and gold-octanemonthiol-gold junctions (lower panel, 114 curves, mirrored for easier comparison). The conductance and force 1D normalized histograms corresponding respectively to the full conductance and force ranges are shown as well. The diamond symbols show the mean force value \overline{F}_b over the conductance intervals $2 \cdot 10^{-6} G_0$ to $8 \cdot 10^{-6} G_0$ and for the interval $8 \cdot 10^{-6} G_0$ to $1 \cdot 10^{-4} G_0$. The open star symbol shows \overline{F}_b for a conductance interval extending $8 \cdot 10^{-6} G_0$ to $1.6 \cdot 10^{-5} G_0$. The 1D force histogram obtained by subtracting the normalized force histograms corresponding to the upper and lower conductance ranges is shown in solid bars. **b** shows the force histograms corresponding to the intervals of $8 \cdot 10^{-6} G_0$ to $1.6 \cdot 10^{-5} G_0$ and $8 \cdot 10^{-6} G_0$ to $1 \cdot 10^{-4} G_0$ respectively. Adapted with permission from [74]. Copyright 2012 Institute of Physics.

have been normalized to the number of conductance bins contributing before the subtraction. This histogram is fitted using the same procedure as described above (solid line). The average force above $0.8 G_{mol}$ corresponds to 1.6 ± 0.4 nN (open diamond). The beige histogram shown in the lower panel of [Figure 3.5](#) is for a conductance range of $8 \cdot 10^{-6} G_0$ to $1.6 \cdot 10^{-5} G_0$. Note how well the fits reproduce the flanks of the histograms.

To estimate the junction breaking force, we restrict the analysis to the force data corresponding to the peak in conductance, i.e. $8 \cdot 10^{-6} G_0 - 1.6 \cdot 10^{-5} G_0$ (beige histogram). Performing this, we obtain an average breaking force $\overline{F}_b = 1.5 \pm 0.1$ which is very close to that obtained for gold-gold junction. This further supports the hypothesis that the gold-gold bond is breaking in the MJs and not the sulfur-gold bond [[9](#), [76](#), [91](#)]. The force data for the MJs do not show a tendency for broadening with increasing conductance as observed for gold-gold contacts. We also observe that the most probable conductance value of $G_{mol} = 1.1 \cdot 10^{-5} G_0$ is in remarkable agreement with the value of $1.2 \cdot 10^{-5} G_0$ attributed to a single S8S molecule junction in earlier work [[14](#)]. Shall few molecules bridge the gap simultaneously and equally contribute to the junction conductance, we would expect clear conductance plateaus at integer multiples of G_{mol} . Such plateaus are only rarely observed at a value of $G_{ts} = 2G_{mol}$ (see e.g. curve 2 in [Figure 2.5](#) lower panel). We infer from these observations that we mostly observe the breaking of MJs consisting of a single molecule. This is also supported by the fact that we operate at a slow gap opening speed and that due to thermal fluctuations a dissociation of the MJ can spontaneously happen [[76](#)], which lowers the probability to have few molecules bridging the gap simultaneously.

We finally consider the lower panel where the monothiol (C8S) data are mirrored for easier comparison to the dithiol data. We observe here that the force mostly remains below 0.7 nN over the whole conductance range (dashed line) while the force histogram shows no shoulder. There is therefore no clear evidence for the formation of mechanically stable MJs in this conductance range. We observe that a small peak around $8 \cdot 10^{-6} G_0$ is visible in the conductance histogram with the corresponding force data being slightly larger than the background. The force however does not reach the values observed in the presence of dithiols and the signal is weak. It has been proposed that molecular bridges may form due to an interdigitation of neighboring alkane chains [[92](#)]. We however do not think that this is a realistic scenario here. As compared to molecular junctions built from conjugated compounds where intermolecular interactions in the form of stacking effects have been reported [[93–95](#)], the Van der Waals interaction between neighboring thiolated alkane chains is substantially weaker.

In summary we have investigated the formation and breaking of gold-gold and gold-molecule-gold junctions using a C-AFM, measuring electrical transport and mechanical properties simultaneously. We show that scatter plots (two-dimensional histograms) are a powerful method to analyze the data and correlate force and conduc-

tance. Using this representation, we can clearly identify the force-conductance region where molecular junctions are formed. We observe that gold-gold and gold-SSS-gold contacts break on average at a very similar force. This supports the assumption that the gold-gold bond is the weakest point in a alkanedithiol-based molecular contacts. We also showed that the mechanism of junction formation is a dynamic process which can be probed by C-AFM. This is particularly striking in about 20% of the measurements which support a scenario where the molecules can migrate along the metal contacts before the junction breaks, thanks to the mobility of surface atoms.

PART II

**GRAPHENE ELECTRODES FOR
MOLECULAR ELECTRONICS**

Why graphene is special

The experimental discovery of graphene in 2004 by Novoselov et al. [96] led to an outburst of scientific activity. But what is it, that makes this material, consisting of a monolayer of hexagonally arranged carbon atoms so interesting? Besides its astonishing mechanical strength [97] it also shows special electrical behavior. It is a two-dimensional system, in which the charge carriers can be tuned seamlessly from holes to electrons and a high carrier mobility can be reached. These properties can be even maintained after functionalizing the surface of graphene devices [33].

Furthermore, the experimental isolation of graphene turned out to be straightforward, only needing a piece of graphite and adhesive tape. Possibilities to grow graphene on large scale either by graphitization of silicon carbide [37] or chemical vapor deposition (CVD) [34, 36] makes it also attractive for industrial applications.

In this chapter we will introduce the main electrical properties of single-layer graphene as well as its phonons and the resulting effects on thermal conductance. Furthermore we will briefly discuss electron-phonon scattering in graphene.

4.1. The graphene lattice

Graphene is a one-atom thick layer of carbon atoms, arranged in a honeycomb lattice. The $2s$ orbital is hybridized with two of the three $2p$ orbitals to form three sp^2 orbitals. Overlapping of the sp^2 orbitals of neighboring atoms leads to σ bonds whereas the remaining p orbitals form π bonds. In this structure the π electrons are not assigned to one double bond anymore, but are delocalized between all carbon atoms.

In terms of crystallography this structure can be described as a triangular lattice with a basis of two atoms per unit cell with the following lattice vectors [98]:

$$\mathbf{a}_1 = \frac{a}{2}(3\hat{x} + \sqrt{3}\hat{y}), \quad \mathbf{a}_2 = \frac{a}{2}(3\hat{x} - \sqrt{3}\hat{y}), \quad (4.1)$$

where $a \approx 0.142$ nm is the carbon-carbon bond length (see Figure 4.1). The reciprocal

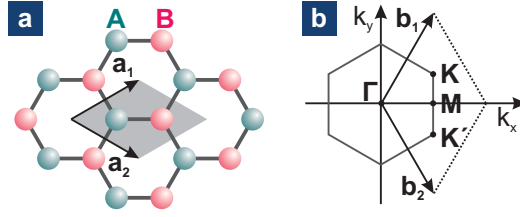


FIGURE 4.1.: **a** Graphene lattice in real-space with the primitive unit cell shown in gray. The different colors show the carbon atoms belonging to the different sublattices. **b** First Brillouin zone of the reciprocal lattice.

lattice vectors are then given by:

$$\mathbf{b}_1 = \frac{2\pi}{3a}(\hat{k}_x + \sqrt{3}\hat{k}_y), \quad \mathbf{b}_2 = \frac{2\pi}{3a}(\hat{k}_x - \sqrt{3}\hat{k}_y). \quad (4.2)$$

The points at the corners of the Brillouin zone (K and K') are of particular interest as we will see in [section 4.2](#). They are inequivalent, but energetically degenerate. [Figure 4.1](#) shows the graphene lattice in real and reciprocal space.

On an isotropic substrate, graphene belongs to the D_{6h}^1 space-group in the Schoenflies notation [99]. At the Γ point the group of the wave vector is D_{6h} and at the K (or K') point it is D_{3h} .

4.2. Band structure and basic electrical properties

To calculate the band structure of graphene, the tight binding model can be used, including nearest (i.e. intersublattice $A - B$, amplitude t) and next-nearest (i.e. intrasublattice $A - A$, amplitude t') neighbor hopping [100]. The following formula is obtained for the conduction (+) and valence (-) band:

$$\epsilon_{\pm}(\mathbf{k}) = \pm t\sqrt{3 + f(\mathbf{k})} - t'f(\mathbf{k}), \quad (4.3)$$

$$f(\mathbf{k}) = 2 \cos(\sqrt{3}\hat{k}_y a) + 4 \cos\left(\frac{\sqrt{3}}{2}\hat{k}_y a\right) \cos\left(\frac{3}{2}\hat{k}_x a\right).$$

As $t' \ll t$ it is often neglected. Expanding the energy dispersion around K (or K' , where we use $\mathbf{k} = \mathbf{K} + \mathbf{q}$) we obtain

$$\epsilon_{\pm}(\mathbf{q}) = \pm \hbar v_F |\mathbf{q}| + \mathcal{O}(q/K)^2, \quad (4.4)$$

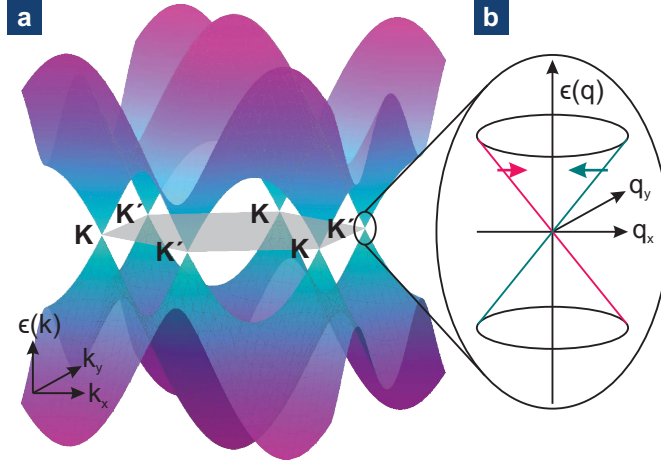


FIGURE 4.2.: **a** Band structure of single-layer graphene in the Brillouin zone and **b** zoom on the dispersion close to K and K' showing the Dirac cones. The arrows represent the different pseudospins at the two branches. Note that the pseudospin is inverted when going from K' to K .

with $v_F = \frac{3ta}{2} \approx 10^6 \text{ ms}^{-1}$ for the empty graphene band [98, 101]. Thus, graphene is a zero-bandgap semiconductor with a linear dispersion for long wavelengths. Its band structure and the linear dispersion close to K or K' are shown in Figure 4.2. This energy dispersion resembles the dispersion relation of massless Dirac particles. Therefore K and K' are also called Dirac points and the band structure in their vicinity is called Dirac cone. The existence of two equivalent sublattices (A and B) leads to a chirality in graphene charge carriers, which can be described as a pseudospin. The pseudospin is inverted for the K and K' points.

Exactly at the Dirac point, one would expect the carrier density n to be zero. However, in reality this is not the case, as it is influenced by other effects like doping, thermal broadening and defects. Still, a region with equal low electron and hole density can be observed experimentally, which is called the charge neutrality point (CNP). As the conduction and valence bands are touching each other, a graphene transistor is ambipolar, meaning that the charge carriers can be tuned smoothly from electrons to holes. The gate induced charge carrier density can be estimated as follows:

$$n = C_g(V_g - V_{off})/e, \quad (4.5)$$

where C_g is the capacitance per area of the gate, V_g is the gate voltage applied, V_{off} is an offset of the CNP due to chemical doping and e is the elementary charge. The

field effect mobility μ is given by

$$\mu = \frac{1}{C_g} \frac{\partial \sigma}{\partial V_g} \quad (4.6)$$

where the two-dimensional conductivity σ is defined as

$$\sigma = \frac{IL}{V_{sd}W} \quad (4.7)$$

by Ohm's law with the current I , the source-drain voltage V_{sd} , the length L and the width W of the graphene channel. μ can be deduced from a field effect transfer curve, where the steepest slope in a σ versus V_g plot is taken for the calculation. For ultra-clean suspended graphene samples, mobilities over $10^6 \text{ cm}^2\text{V}^{-1}\text{s}^{-1}$ were measured [102]. Surface adsorbates, defects and the interaction with the substrate lower this value, and typical values for graphene on silicon dioxide (SiO_2) range between $1000 \text{ cm}^2\text{V}^{-1}\text{s}^{-1}$ and $10000 \text{ cm}^2\text{V}^{-1}\text{s}^{-1}$ [102].

These special electrical characteristics of graphene lead to the observation of room temperature quantum Hall effect [103], ballistic transport [104–106] or Klein tunneling [107].

4.3. Phonons in graphene

As we have seen in section 4.2, the graphene unit cell contains two carbon atoms. This leads to six phonon branches, three acoustic (A) and three optical (O) branches. One of each corresponds to out-of-plane modes (ZA and ZO). The other vibrations are in-plane and are classified as longitudinal (LA and LO) and transversal (TA and TO). The phonon dispersion relation of graphene is shown in Figure 4.3.

At the zone center Γ , the LO and TO modes are degenerate and correspond to

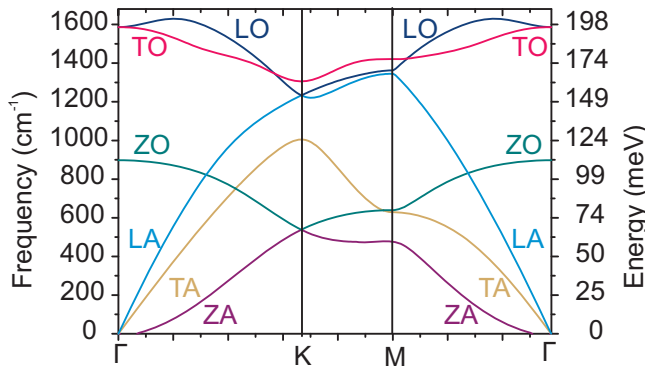


FIGURE 4.3.: Calculated phonon dispersion relation of graphene. Adapted with permission from [108], Copyright 2008 by the American Physical Society.

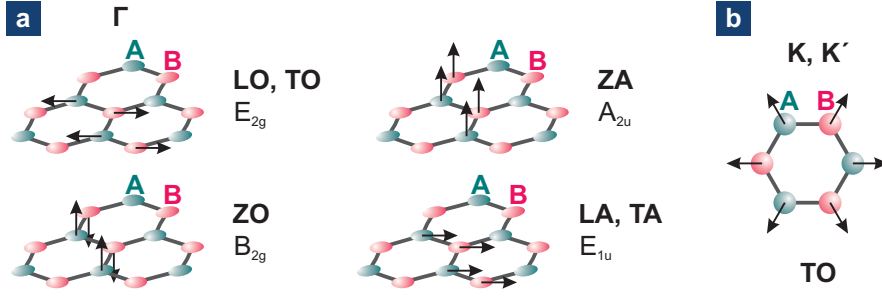


FIGURE 4.4.: **a** Γ -point phonon modes of graphene and **b** TO phonon at the K or K' point. The different colors show the sublattices A and B , the arrows show the movement of the atoms.

vibrations of the sublattice A against the sublattice B . They belong to the E_{2g} point group. The ZO phonon is an out-of-plane movement of sublattice A against sublattice B . It belongs to the B_{2g} group. For the ZA (A_{2u} group), LA and TA (E_{1u} group) phonons both sublattices move synchronously and they are infrared-active. Close to the K or K' point, the TO phonon corresponds to a breathing mode of the lattice, which belongs to the A'_1 group [99, 109]. The vibrations of the other phonons at the K and K' points are more complex and belong to the E' (LA and LO) and the E'' (ZA and ZO) groups. The phonon movements at the Γ point and the breathing mode are shown in Figure 4.4.

Another important effect arising from an abrupt change in the screening of atomic vibrations by electrons is the presence of Kohn anomalies at the high symmetry points in graphene [108, 110]. More precisely for the TO and LO phonon at the Γ point and for the TO phonon at the K point. Kohn anomalies are associated with a strong electron-phonon coupling. This means that an electron-hole pair can be created by absorbing a phonon. The electron-hole pair then recombines while emitting a phonon at a slightly reduced energy. This process leads to a shorter lifetime and a softening of the phonons.

4.3.1. Heat transport

Heat transport can be conducted by both, electrons and phonons. Comparable to electric transport, thermal transport can be diffusive or ballistic (see chapter 1), depending on the device dimension L_D in comparison with the mean free path of the main heat carriers (ℓ_{ph} , for phonons, which is ≈ 100 nm at room temperature or ℓ_e for electrons, which is ≈ 20 nm at room temperature [111]). In the diffusive regime ($L_D \gg \ell_{ph,e}$) the thermal conductivity κ is defined by Fourier's law:

$$q = -\kappa \nabla T, \quad (4.8)$$

where q is the heat flux density and ∇T is the temperature gradient. Normally κ is treated as a constant, but this is only true for small temperature variations. In a wider temperature range $\kappa(T) = \kappa_e(T) + \kappa_p(T)$ is a function of the temperature T and is given by the sum of the electron κ_e and phonon κ_p contributions. In metals, the electronic contribution κ_e is dominant, as there is a large amount of free electrons. The electron contribution κ_e can be deduced from the Wiedemann-Franz law:

$$\kappa_e/(\sigma T) = \pi^2 k_B^2 / (3e^2), \quad (4.9)$$

where σ is the electrical conductivity, k_B is the Boltzmann constant and e is the elementary charge. In graphene, due to its strong covalent bonds, heat transfer over the lattice vibrations is very efficient and heat conduction is dominated by the phonons [112]. However, in highly doped samples the electron contribution can become significant. At which n κ_e starts to become significant is strongly dependent on μ . The phonon contribution κ_p is expressed by

$$\kappa_p = \sum_j \int C_j(\omega) v_k^2(\omega) \tau_j(\omega) d\omega, \quad (4.10)$$

where j is the phonon branch, C_j is the heat capacity for branch j , v_k is the group velocity and τ_j is the relaxation time. In real samples the thermal conductivity is not only limited by phonon-phonon scattering due to anharmonicity and electron-phonon scattering (intrinsic), but also by scattering on edges, defects, impurities and grain boundaries (extrinsic). For suspended graphene, values for κ were found in the range from 2000 to 5000 $\text{Wm}^{-1}\text{K}^{-1}$ [113, 114]. Due to the coupling to the substrate and scattering on the interface, supported samples show a lower value ($\approx 600 \text{Wm}^{-1}\text{K}^{-1}$ on silicon dioxide (SiO_2)) [115]. This is still higher than in copper ($\kappa \approx 400 \text{Wm}^{-1}\text{K}^{-1}$), which is one of the best metal heat conductors [112].

4.3.2. Energy dissipation and electron-phonon scattering

At high current densities, heat will be generated in the Graphene channel due to Joule heating (we will examine this effect in more detail in [chapter 8](#)). This heat can be dissipated over different pathways, including the environment, the electrodes and the substrate. The heat flow to the environment can be assumed to be small, especially for experiments performed in vacuum [116]. The interfacial thermal resistance, which is a measure of an interface's resistance to thermal flow, between graphene and SiO_2 is only $\approx 4 \cdot 10^{-8} \text{Km}^2\text{W}^{-1}$ [116]. Thus, for non-suspended samples, most of the heat dissipates directly into the substrate and only a minor part is evacuated over the contacts [111, 116, 117].

The heat produced through Joule heating originates from electron-phonon scattering of hot electrons. For non-suspended graphene devices, three kind of phonons can contribute to this process. The acoustic and optical phonons of the graphene as well as remote interface phonons (RIPs) forming at the SiO₂ graphene interface [118–120]. The scattering with the acoustic phonons can be considered as elastic and the phonon-limited resistivity $\rho(T)$ depends linearly on the temperature $\rho(T) \propto T$ above the Bloch-Grüneisen temperature Θ_{BG} and is proportional to $\rho(T) \propto T^4$ below [121]. Θ_{BG} marks the characteristic temperature scale for low electron density systems (comparable to the Debye temperature for metals) and is given by

$$\Theta_{BG} = \frac{2\hbar v_k k_F}{k_B}, \quad (4.11)$$

where \hbar is the reduced Planck constant, v_k is the phonon velocity, k_F is the radius of the Fermi sphere and k_B is the Boltzmann constant. In graphene Θ_{BG} reaches from 100 K to 1000 K, depending on the charge carrier density [121]. For scattering with the optical graphene phonons and RIPs, the temperature dependence of the resistivity can be described over a Bose-Einstein distribution ($\rho(T) \propto \left(\frac{1}{e^{E_0/k_B T} - 1}\right)$), where E_0 is the phonon energy [118, 119]. Scattering with optical phonons and/or RIPs is considered as an important heat dissipation mechanism in graphene devices.

Chemically vapor deposition of graphene: flakes above the micron scale

The method used first to produce graphene is the mechanical exfoliation [96]. Samples fabricated with this procedure show high quality, but are limited in size. Thus new methods for the production of graphene up to industrial scale evolved during the last years. This includes chemical exfoliation [122], graphitization of silicon carbide [37] and chemical vapor deposition (CVD) on copper (Cu) [34, 35].

To fabricate graphene electrodes it is important to have large areas of monolayer graphene. That the graphene is defect free and shows a high charge carrier mobility is desirable, but not needed. Thus we decided to rely on CVD graphene, which offers the possibility to grow large-area, polycrystalline films [34–36]. The growth of graphene on a Cu surface leads to films consisting of mostly monolayer, as the process is believed to be self-limiting [34] and charge carrier mobilities close to the ones of exfoliated graphene have been reported [34, 123]. After growth, the graphene has to be transferred from the metal foil, where growth takes place, to a substrate more suitable for transport measurements. Ideally, the transfer process should not lead to damage or contamination of the graphene. Thus not only the growth, but as well the transfer are crucial for the fabrication of high quality devices made from CVD graphene.

In this chapter we will discuss the principles of CVD graphene growth on Cu, as well as the parameters and transfer technique used in our group. Furthermore we will characterize our CVD graphene by imaging techniques and transport measurements.

5.1. The principle of chemical vapor deposition

Chemical vapor deposition on transition metals attracted a lot of attention in the last years as a method to grow large continuous graphene films [36]. Growth on copper foils seem to be particularly promising, as it leads to monolayer graphene in a reproducible way. Growth on Cu has been introduced by Li et al. in 2009 [34] and

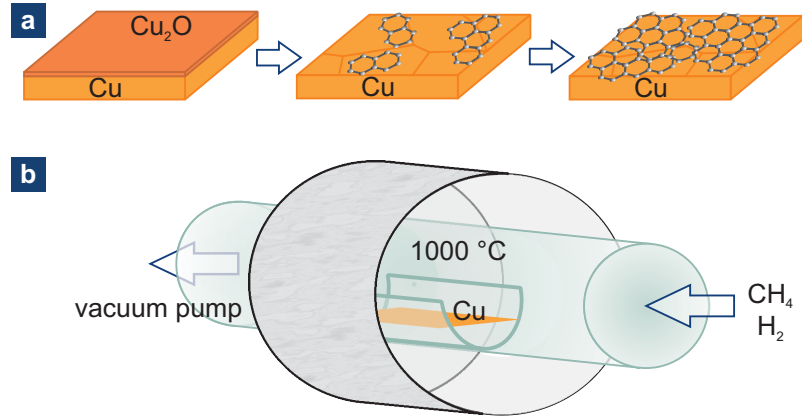


FIGURE 5.1.: **a** Sketch of graphene formation via CVD on Cu foil. First the copper oxide is reduced. When the growth temperature is reached, the CH_4 is added and graphene growth starts at several nucleation sides. This continues until all the Cu is covered by graphene and its catalytic action gets inhibited. **b** Schematic drawing of the CVD oven.

most of the later work (including ours) is based on their findings.

In this process a copper foil is used as both, substrate and catalyst. The advantages of Cu are its low carbon solubility and its possibility to form weak bonds to carbon. The low carbon solubility inhibits multilayer growth through precipitation and the weak attraction between the carbon and the Cu stabilizes the carbon on the Cu surface. In a first step, the native copper oxide (Cu_2O and CuO) will be reduced during heating up the foil in a hydrogen (H_2) environment. When the growth temperature is reached ($\approx 1000^\circ\text{C}$), methane (CH_4) is added as the carbon source and the H_2 acts as a control reagent. The CH_4 gets decomposed into carbon atoms and H_2 , where the Cu acts as a catalyst:



The carbon solubility in bulk Cu is very low, while the diffusion of the carbon atoms on the Cu surface is high. Thus the process is surface based [124]. Experiments using isotopic labeling of the CH_4 precursor gas have indeed shown, that at low pressure the graphene grows radially, starting at several nucleation sides [125]. As soon as the whole Cu surface is covered, its catalytic action is inhibited and the growth is self-limiting. The graphene grown with this process is mostly monolayer, but polycrystalline. Some recent research focused on the optimization of the growth process to form bigger mono-crystalline areas [126–128]. A self-limiting process also means, that growth time and cooling rates do not affect the graphene thickness. However, for graphene growth at ambient pressure the process is not self-limiting as

kinetics start to play an important role [129]. A sketch showing the main steps in graphene growth is shown in [Figure 5.1](#).

5.2. Finding the right growth parameters

Optimizing graphene growth is time consuming, as there are many parameters which have to be tuned in a systematic way. For our purpose monocrystallinity or extraordinary high charge carrier mobilities are not needed, but it is important to find a reproducible and reliable process. The setup of the low-pressure CVD system and the development of a protocol for graphene growth and transfer, as described herein, was conducted in teamwork with Dr. Wangyang Fu.

5.2.1. Copper foil pretreatment

As substrate and catalyst for the graphene growth we use polycrystalline copper foil (25 μm , 99.8% from Alfa Aesar). We also tried thicker (50 μm) and purer (99.999%) copper foil, but could not observe a difference in the graphene properties (the characterization of the graphene will be discussed in [section 5.4](#)). The thicker foil makes the handling easier and allows longer annealing times, but also the etching during transfer is prolonged. Prior to growth, the copper foil is washed in acetone and in 2-propanol. The copper foil has a native oxide. This can be reduced either prior to the growth by etching in orthophosphoric acid (H_3PO_4) or through annealing in the CVD oven in hydrogen (H_2) atmosphere. We could not observe a difference in the graphene properties if the additional wet etching step was performed. A short

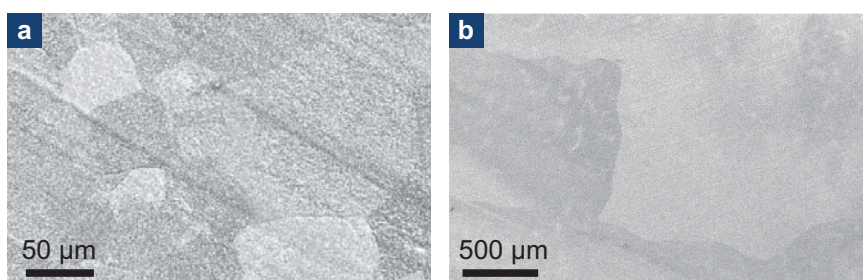


FIGURE 5.2.: **a** SEM image of a piece of Cu foil after annealing for 15 min in H_2 environment at 1000 $^\circ\text{C}$. The grain size is in the order of tens of μm . The white spots correspond to native copper oxide, the grooves ranging from the top left to the bottom right corner come from the rolling of the Cu foil during manufacturing. **b** SEM image of a piece of Cu foil after 30 min annealing in H_2 atmosphere at 1000 $^\circ\text{C}$ and subsequent graphene growth (15 min at 1000 $^\circ\text{C}$). The grain size is in the range of mm.

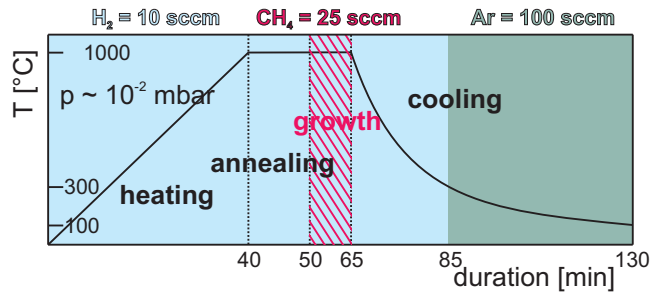


FIGURE 5.3.: Schematic illustrating the conditions during graphene CVD.

annealing step was always performed to allow for the Cu surface to rearrange and increase the Cu grain size. [Figure 5.2](#) left panel shows a scanning electron microscope (SEM) image of the Cu foil after 15 min annealing in H_2 atmosphere at 1000°C . We think that the white spots correspond to copper oxide which could have formed when transferring the Cu foil from the oven to the SEM in ambient conditions. The grooves going from the top left to the bottom right corner are due to the rolling of the copper foil during its manufacturing. [Figure 5.2](#) right panel shown a SEM image of a Cu foil after 30 min annealing in H_2 atmosphere at 1000°C and subsequent graphene growth (15 min at 1000°C). The grain size is an order of magnitude bigger than for the image discussed before and no oxide is visible as the graphene layer prevents oxidation.

5.2.2. Setup and conditions

A schematic drawing of the growth setup is shown in [Figure 5.1](#). For first tests we used an ambient pressure system consisting of a Carbolite MTF single zone tube furnace and gas bottles connected over Kobold variable area flowmeters. Later on we set up a low-pressure system consisting of a Carbolite HZS horizontal split 3 zone tube furnace, Aalborg GFM thermal mass flow meters, a LNI Schmidlin NMH_2 1000 hydrogen generator and a rotary pump. This setup is based on the one used by the group of Prof. Dr. András Kis at the EPF Lausanne.

Reproducible growth conditions are found for the following conditions: 10 sccm H_2 during the whole process (except cooling $< 300^\circ\text{C}$) and an annealing time of 10 min, 25 sccm CH_4 during growth and a growth time of 5 min at a base pressure of ≈ 0.015 mbar. To cool down faster, the oven is opened after growth and when the temperature drops below 300°C the H_2 channel is closed and the further cooling is performed at a 100 sccm Ar flow. A schematic for these conditions is shown in [Figure 5.3](#). During heating, annealing and the first cooling step the pressure raised to 0.3 mbar, due to the H_2 flow. During the growth a pressure of 0.8 mbar is measured and the cooling under Ar flow leads to a pressure of ≈ 1 mbar. If the annealing time is prolonged, the Cu foil shows larger grains (see [Figure 5.2](#)), but no remarkable difference is observed for the graphene quality. Also no differences in the graphene properties are observed for lower cooling rates.

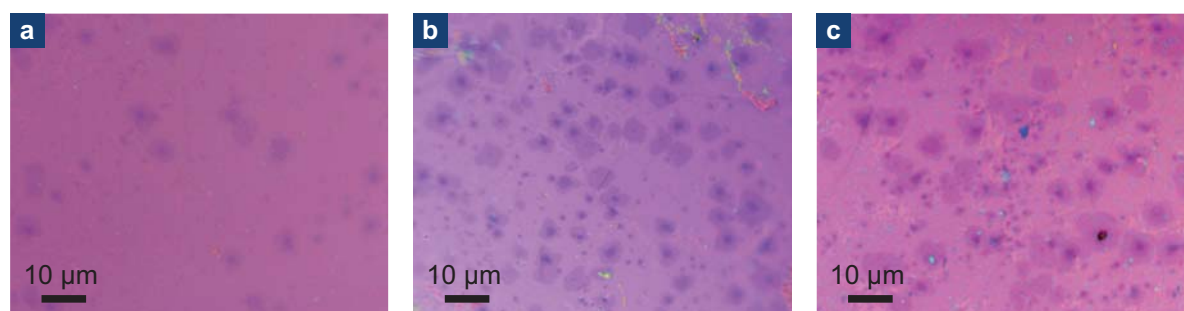


FIGURE 5.4.: Optical images of transferred graphene grown at **a** 1010 °C **b** 1030 °C and **c** 1050 °C.

These growth conditions were found after trying different approaches. We started with CVD growth at ambient pressure with typical flow rates of 20 sccm hydrogen during heating, annealing, growth and cool down and additionally 140 sccm methane during a growth time of 20 min. These values are the minima which can be reached with the Kobold flowmeters. Raman spectroscopy (we will describe the Raman spectroscopy of graphene in detail in [chapter 6](#)) was used to identify graphene growth. However under these conditions, growth yield was only $\approx 50\%$ and the as-grown graphene showed many bilayer regions and a large defect density. We attribute this to a too high partial pressure of CH_4 [129]. As the Kobold flowmeters do not allow a well-controlled CH_4 flow at low rates, we switched to argon (Ar) with a concentration of 200 ppm of CH_4 . Unfortunately, yield in graphene growth was even lower under these conditions, but Raman spectroscopy showed that the graphene grown is mostly monolayer and shows a smaller defect density. A further possibility is the graphene growth at low pressure [34]. The first tests (at a base pressure of $\approx 10^{-2}$ mbar) resulted in monolayer graphene with a high yield. To investigate the temperature dependence on the graphene quality, we performed growth at 1010 °C, 1030 °C and 1050 °C. At all temperatures the graphene showed a low defect density, but at the two higher temperatures more bilayer flakes were observed as shown in [Figure 5.4](#).

5.3. Transferring the graphene onto a wafer

To perform electrical measurements, the CVD graphene has to be transferred from the Cu foil, where growth takes place, to an insulating substrate. It is important to have a procedure where the graphene quality is not decreased by contaminants or rupture and large areas can be transferred. Several methods have been proposed during the last years [35, 125, 130–134].

We use a wet transfer adapted from the process described by Li et al. [125].

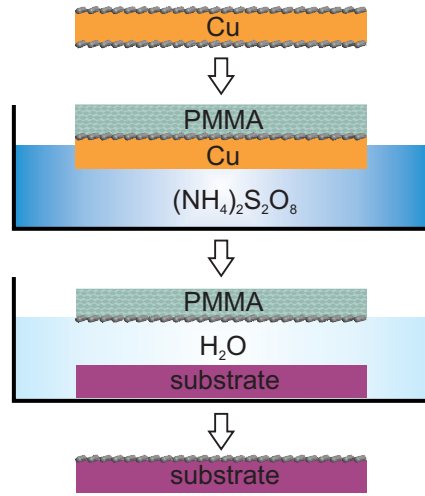


FIGURE 5.5.: Wet transfer of graphene from Cu foil to an insulating substrate

The process established after some rounds of optimization is briefly described in the following and the main steps are illustrated in [Figure 5.5](#). The experimental details and the different approaches tried are described in [appendix B](#).

- First, the as-grown graphene is spin coated with a poly-methyl methacrylate (PMMA) layer of 300 nm thickness.
- Then the graphene layer on the backside of the Cu foil is removed using an argon/oxygen (Ar/O_2) plasma.
- To etch the copper foil, the PMMA/graphene/Cu stack is placed on the Cu etchant.
- After the Cu is etched fully away, the PMMA/graphene stack is washed in several water baths.
- As a next step the graphene is placed onto a clean Si/SiO_2 wafer, either by fishing the graphene with the substrate or by placing the substrate below the graphene and removing the water gently.
- The sample is dried, and as a last step, the PMMA layer is dissolved.

This process leads to clean and continuous graphene in $\approx 50\%$ of the conducted transfers. In the other cases the graphene surface is not clean on a large scale or the graphene layer has many holes. Transfer processes where the graphene is never in direct contact with a polymer were demonstrated recently [135, 136]. This could help to improve the cleanliness of the graphene surface. Also different annealing procedures [56, 137] or plasma cleaning [138] were proposed to enhance the graphene surface quality.

5.4. Characterization of CVD graphene

Several techniques can be used to investigate the graphene quality. The most common ones are imaging techniques, Raman spectroscopy and electrical measurements. Making graphene visible is actually not a trivial task as it is only one atom thick. Its optical contrast varies strongly with the SiO₂ thickness and the light wavelength [139]. But once the right parameters are found optical microscopy is straight forward and even allows to distinguish between mono- and bilayer graphene [140, 141]. More sophisticated tools like the STM even allow to image graphene at atomic resolution [137]. Raman spectroscopy probes the graphene phonons and thus gives not only insight into the number of layers, but also defects and edge structures. It will be addressed in detail in chapter 6. We also want to test the electrical properties of our graphene, namely the doping and charge carrier mobility. This is important, as its ambipolar behavior and possibly high charge carrier mobilities make graphene special (see as well chapter 4). However, grain boundaries, defects and contaminations are expected to decrease the mobility and to lead to a doping of the graphene.

5.4.1. Imaging graphene

We use different imaging techniques to investigate the properties of our CVD grown graphene. This includes optical and scanning electron microscopy (SEM), atomic force microscopy (AFM) and scanning tunneling microscopy (STM). STM and optical microscopy are performed on graphene transferred to SiO₂, whereas the other techniques are performed before and after transfer. Example images of all four techniques are shown in Figure 5.6.

SEM proved to be a versatile and fast tool to check if defects and contaminations were already there before transfer, as well as to check for bilayer flakes and grain boundaries. However as it can lead to the deposition of amorphous carbon it is not favorable to look at the graphene prior to fabrication and measurement of the samples. If the right thickness is chosen for the gate oxide (≈ 300 nm), graphene exhibits a nice contrast for optical microscopy and the number of layers can be determined [139–141]. For us, this technique is especially helpful to control the cleanliness after transfer and during sample fabrication. AFM (FlexAFM (Nanosurf, Switzerland) in combination with PPP-XYNCHR (Nanosensors, Switzerland) cantilevers) is used to look at the roughness of the copper foil and to investigate the graphene after transfer. It is more time consuming than the other techniques, but offers a higher lateral and vertical resolution. The copper step edges have a height of > 2 nm and up to 600 nm deep grooves are observed on the Cu foil. The STM measurements were performed by Samuel Bouvron at the University of Konstanz. He achieved atomic resolution over an area of 40 nm x 40 nm, showing that our graphene has no vacancies over this region.

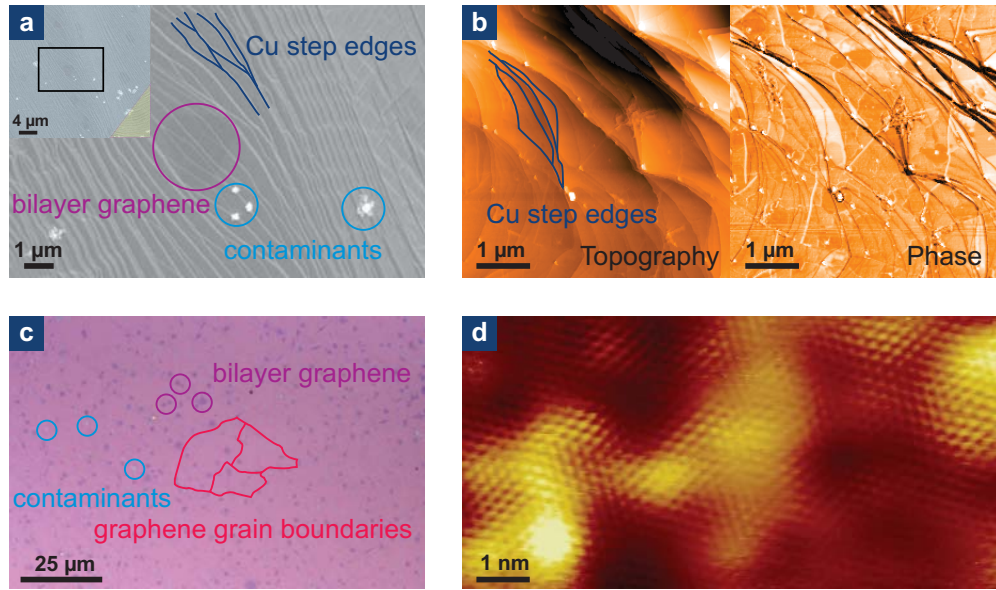


FIGURE 5.6.: **a** SEM and **b** AFM topography and phase images of CVD graphene on Cu ($25\ \mu\text{m}$) directly after growth. **c** Optical and **d** STM images of graphene after transfer to SiO₂. The step edges of the copper are clearly visible with a height $> 2\ \text{nm}$ (highlighted in dark blue). Graphene bilayer flakes are visible before and after transfer (highlighted in purple). Contaminations are highlighted in blue and graphene grain boundaries in pink. The STM image in **d** shows atomic resolution and was recorded by Samuel Bouvron at the University of Konstanz.

5.4.2. Transport measurements

A relatively easy way to determine some of the basic electric properties of graphene is the fabrication of a field effect transistor (FET). This allows to measure the field effect mobility μ and the intrinsic doping of the graphene. To fabricate graphene transistors, a first lithography step (either UV- or e-beam lithography, protocols see [appendix I](#)) is used to fabricate an etch mask for the graphene (in this case we fabricated a quadratic device). The etching is done by a O₂/Ar plasma. A second fabrication step is needed to deposit the electrodes. For this 50 nm Au with a 5 nm Ti adhesion layer are used. The doped Si substrate is used as a back gate. The left panel of [Figure 5.7](#) shows a schematic of the device. The right panel shows the resistivity (turquoise triangles) and conductivity (black circles) of a graphene FET (GFET) during sweeping the gate voltage (V_g) under an applied bias $V_b = 100\ \text{mV}$. Note that this measurement was done in a two-terminal configuration, but that we assume the contact resistance to be small ($\approx 200\ \Omega$). The contact resistance was estimated comparing the two-terminal and four-terminal resistance of similar devices. For this particular device we extracted a μ of $735.8\ \text{cm}^2\text{V}^{-1}\text{s}^{-1}$ from the linear fit (pink line) shown in [Figure 5.7](#) and using [Equation 4.6](#). Typical values we measured for μ on

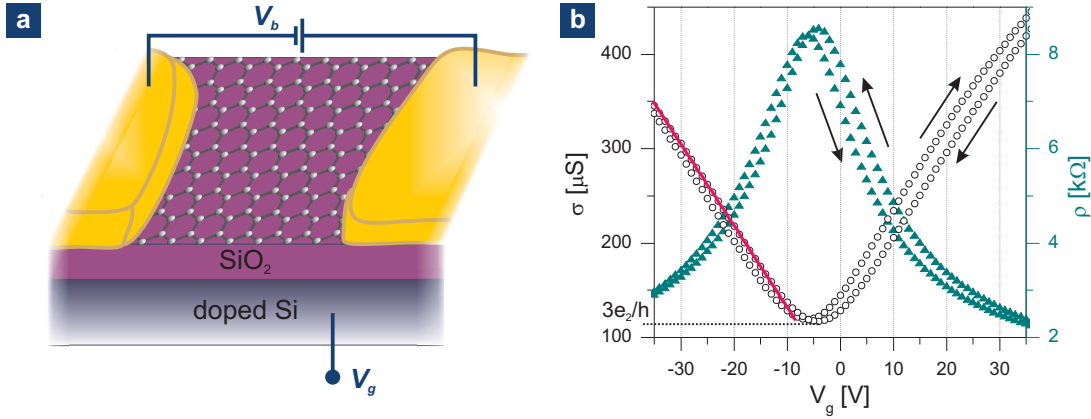


FIGURE 5.7.: **a** Illustration of a graphene FET, with bias voltage V_b and gate voltage V_g . **b** Conductivity and resistivity of a graphene field effect transistor versus gate voltage.

similar devices were between $300 \text{ cm}^2\text{V}^{-1}\text{s}^{-1}$ and $3000 \text{ cm}^2\text{V}^{-1}\text{s}^{-1}$ [33]. In the same study, we also performed Hall measurements which lead to mobilities in agreement with the ones deduced by the field effect. These values for μ are similar to typical values found for exfoliated graphene, whereas the highest reported values for μ are one order of magnitude bigger [102]. For the device in Figure 5.7 the charge-neutrality point (CNP) is at $\approx -5 \text{ V}$, thus the graphene is slightly n-doped. However, this differs quite substantially from sample to sample and n-doped and p-doped devices have even been found on the same sample. We observed a change in the position of the CNP when measuring the device in vacuum and ambient conditions. Normally the devices become more p-doped under ambient conditions. This could be due to the absorption of gas molecules on the graphene [142]. Note that performing Raman spectroscopy can shift the CNP position towards 0 V . This may be due to heating caused by the laser. It is well known that heating can move contaminants [143], further the heating could also have an influence on the absorption and desorption of gases [142]. The conductance minimum of this device is at $\frac{3e^2}{h}$, which is in agreement with the typical values found experimentally clustering between $\frac{2e^2}{h}$ and $\frac{4e^2}{h}$ [98, 144]. Theory predicts a value of $\frac{4e^2}{\pi h}$ [98]. These measurements show that the CVD graphene grown by our process exhibits the typical graphene electrical behavior and has a decent charge carrier mobility.

Raman spectroscopy: characterizing graphene

Raman spectroscopy is a versatile tool for studying the properties of graphene [109, 110, 145]. It allows the determination of the number of layers and can be used to detect defects and edge chirality. Furthermore it is sensitive to perturbations such as doping, strain and temperature. As Raman spectroscopy is fast, non-destructive and relatively easy to use, it has become one of the most important tools for graphene characterization in research.

In this chapter the basics of Raman spectroscopy and the Raman modes for graphene will be introduced. In particular we will investigate the effect of temperature on the graphene Raman signal and discuss briefly the influence of other aspects.

6.1. A brief introduction to Raman spectroscopy

Light scattering is classified according to the change in energy experienced by the scattered photon. The inelastic scattering of a photon on a phonon with an energy shift $> 1 \text{ cm}^{-1}$ is called Raman scattering [146]. The electromagnetic field of the incoming light leads to a perturbation of the system. This perturbed state does not have to correspond to a stationary state and is called a virtual state. The system will then relax to a vibrational state by emitting a photon with an energy shifted by the difference between the ground state and the vibrational state. This is called Stokes scattering. If the system directly relaxes to the ground state no energy shift occurs, this is called Rayleigh scattering. A third process is the anti-Stokes scattering. For which the system already has to be in a vibrational state and is then excited to a virtual state by absorbing a photon. It can then relax to the ground state by emitting a photon which is shifted to a higher energy. The probability of this process depends on the phonon occupation of the excited state, which is usually low at room temperature for graphene phonons. The possible scattering processes are depicted

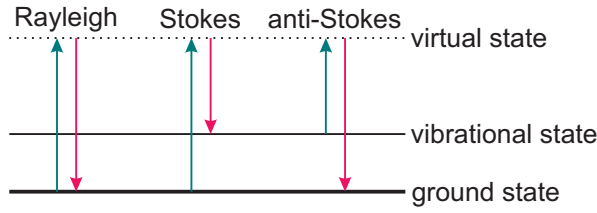


FIGURE 6.1.: Rayleigh and Raman scattering

in [Figure 6.1](#). In the Stokes process a phonon is created, whereas in the anti-Stokes a phonon is annihilated. If the stationary state corresponds to an electronic state, the process is enhanced and is called resonant Raman scattering. Due to its linear gapless electric dispersion, Raman scattering in graphene is always resonant. This makes it possible to observe a signal even from a single layer of graphene [\[145\]](#).

As the momentum has to be conserved, first order Raman processes are only allowed for phonons near the Γ point (where $k \approx 0$). Scattering on multiple phonons or defects can lead to higher order Raman processes, if the overall momentum is conserved. The interaction of the incoming light with a phonon is only possible under certain circumstances. For elastic scattering (as in infrared spectroscopy) the vibrational state has to be polarizable to interact with the electric field of a photon. In an inelastic process, like Raman scattering, the derivative of the polarizability with respect to the vibration coordinate has to be non-zero. The form of the polarizability tensor can be determined by the space symmetry of the scattering source [\[146\]](#).

Raman processes lead to sharp Lorentzian peaks in the energy spectrum of the scattered light. The peak area depends on the number of scattering events. The width of a Raman peak is mainly determined by the finite lifetime of the corresponding phonon (due to anharmonicity or electron-phonon coupling). Other effects like the electron-hole dispersion anisotropy (phonons emitted in different directions have different frequencies) or the electronic momentum uncertainty also play a role [\[109\]](#). Raman peaks are quite sensitive to the phonon properties (their lifetimes and energies) which makes Raman spectroscopy a powerful tool for material characterization.

6.2. Raman active modes in graphene

We have seen in [section 6.1](#) that first order Raman processes are only allowed in the vicinity of the Γ point. Of the optical graphene phonons (see [section 4.3](#)), only the in plane phonons (LO and TO) belong to a point group which is Raman active. They are degenerate at an energy of $\approx 1580 \text{ cm}^{-1}$, leading to a distinct peak in the Raman spectrum of graphene, called the G-band. Also the breathing mode (TO phonon at the K point) is Raman active. As it lies at the K point, due to momentum conservation, it needs a defect (can also be an edge or grain boundary) or another phonon for its activation. Its combination with a defect leads to the D-band at $\approx 1350 \text{ cm}^{-1}$. The intensity of this band gives us a qualitative measure

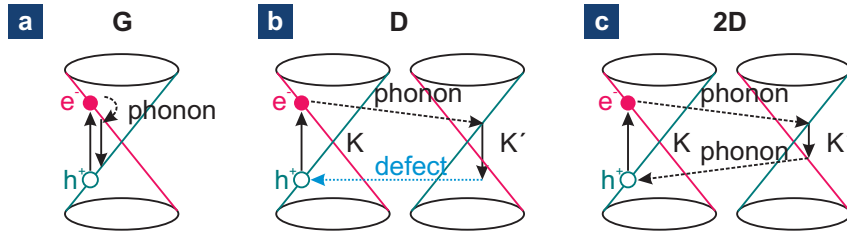


FIGURE 6.2.: **a** One-phonon scattering process responsible for the G-peak, **b** intervalley scattering on a defect and a phonon leading to the D-peak and **c** two-phonon scattering in graphene Raman spectra.

of the number of defects, grain boundaries and edges in the graphene. The more disordered the graphene is, the larger the D-band will be. For amorphous carbon the D-band will disappear, as no carbon rings are present anymore [109]. A two-phonon scattering process of the breathing mode phonon gives a resonance at $\approx 2700 \text{ cm}^{-1}$, called the 2D-band. The exact positions of both, the D-band and the 2D-band depend on the energy of the laser used, and shift linearly to higher wavenumber with increasing laser energy [109, 110]. Figure 6.2 shows the scattering processes leading to the main Raman peaks in graphene. Other, less important peaks are the D'-band and the D''-band (attributed to LO and LA phonons respectively) at $\approx 1620 \text{ cm}^{-1}$ and $\approx 1100 \text{ cm}^{-1}$ respectively, as well as their combinations with the D-band phonon [109].

Raman spectroscopy can be used to determine the number of layers and their stacking [109, 110]. For exfoliated graphene samples, the shape and size of the 2D-band depends on the number of layers. For bilayer graphene, two phonon modes exist at both the K and K' point. This leads to four possible scattering processes with slightly different energies, building a peak consisting of four Lorentzians instead of one as for monolayer graphene. For graphene with non Bernal stacking, as often present in CVD grown samples, this behavior can change and more care when assigning the number of layers has to be taken. In CVD graphene the peaks are generally broader than for exfoliated graphene. Instead of the peak shape, the intensity ratio of the G- and 2D-band gives a good measure for the number of layers [110]. For monolayer graphene the intensity of the 2D-band is higher than the intensity of the G-band, for bilayer it is similar and for more than two layers the G-band is larger. However, for samples containing a lot of defects this is not true anymore.

Raman spectra of graphene containing one, two and three layers are shown in Figure 6.3. The Raman measurements were performed on CVD graphene grown on Cu foil and then transferred to a Si/SiO₂ wafer as described in chapter 5. The experimental details of our Raman microscope are given in appendix C. A map showing the fraction between the area of the 2D- and the G-band as well as map representing the integral over the defect induced D-band are shown as well. The 2D

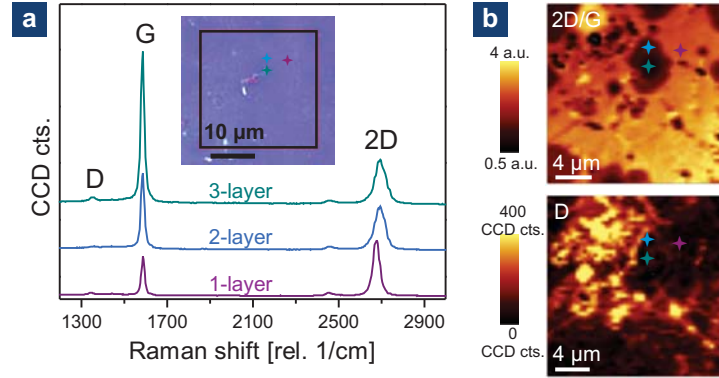


FIGURE 6.3.: **a** Raman spectra of graphene containing one, two and three layers. **b** Maps showing the ratio between the areas of the 2D- and G-band as well as the area of the D-band

over G ratio allows to distinguish the number of layers easily. The D-band shows the accumulation of defects in top left of the examined region. The origin of these defects is unclear.

6.3. Temperature dependence of graphene Raman spectra

Thermal expansion and anharmonic phonon-phonon interactions lead to a temperature dependence of the phonon frequency and line width. A phonon softening is observed for all three of the main graphene Raman bands. Thus Raman spectroscopy can act as a local thermometer for graphene [147]. As the G-band is dependent on the carrier density (we will further discuss this in section 6.4), which can change during heating (a systematic study is shown in section 8.3), this peak is not favorable for temperature measurements. The 2D- and D-band positions are not sensitive to the carrier density and thus better options. The 2D-band shows a larger shift than the D-band, as it involves two phonons. This makes it the first choice for temperature measurements.

Another method to deduce the local temperature is to look at the ratio of the intensities of the Stokes (I_S) and the Anti-Stokes (I_{AS}) signal, as [146]:

$$\frac{I_S}{I_{AS}} \propto \exp\left(\frac{\hbar\omega_0}{k_B T}\right). \quad (6.1)$$

However, at room temperature or below, this method is limited by the small intensity of the Anti-Stokes signal because of the low phonon population.

The positions and widths of the Raman peaks are deduced by fitting them to

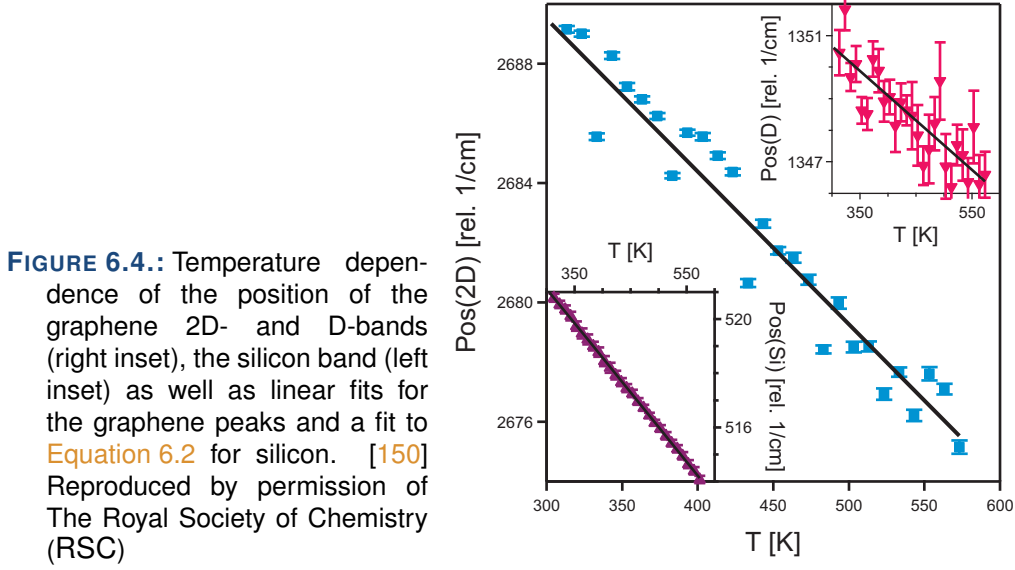


FIGURE 6.4.: Temperature dependence of the position of the graphene 2D- and D-bands (right inset), the silicon band (left inset) as well as linear fits for the graphene peaks and a fit to Equation 6.2 for silicon. [150] Reproduced by permission of The Royal Society of Chemistry (RSC)

a Lorentzian function. Figure 6.4 shows the peak positions of the 2D-band (blue squares), the D-band (right inset) and the silicon (Si) peak at $\approx 520 \text{ cm}^{-1}$ (left inset) for a CVD graphene sample on a Si/SiO₂ wafer during external heating. Fitting a line to the 2D-band and D-band positions leads to a slope of $-0.051 \pm 0.002 \text{ cm}^{-1}\text{K}^{-1}$ and $-0.016 \pm 0.002 \text{ cm}^{-1}\text{K}^{-1}$ respectively. This is between the $-0.034 \text{ cm}^{-1}\text{K}^{-1}$ and $-0.070 \text{ cm}^{-1}\text{K}^{-1}$ reported for the 2D-band by other groups [147, 148]. For the 2D-band one would expect the shift to be twice the shift of the D-band as two phonons contribute to the scattering process. However this is not observed here. One reason could be that fitting the D-peak gives a huge error (error bars are shown in Figure 6.4) and thus the deduced shift could be unreliable. We also observe a broadening of the graphene peaks with increasing temperature. This can be explained by the shorter phonon lifetimes at elevated temperature due to enhanced electron-phonon and phonon-phonon scattering. For the G-band we do not observe a significant shift, however this has been reported by other groups [147, 149]. As the G-band position is also influenced by the local doping, this discrepancy could be explained by a change in the doping due to the heating in ambient conditions (we will come back to this effect in section 8.3).

The shift of the Si peak at $\approx 520 \text{ 1/cm}$ was fitted with a model for inelastic scattering based on three phonon processes [151, 152].

$$Pos(Si) = \omega_0 + \gamma \left(1 + \frac{2}{e^x - 1} \right), \quad (6.2)$$

with $x = \hbar\omega_0/k_B T$, where ω_0 is the Raman frequency shift at 0 K, γ is a constant, \hbar is the reduced Planck constant, k_B is the Boltzmann constant and T is the temperature.

At the temperature scale of our experiment, the frequency dependence of the Si peak on T is almost linear. We found values of $\omega_0 = 536.7 \pm 0.1 \text{ cm}^{-1}$ and $\gamma = -5.07 \pm 0.02 \text{ cm}^{-1}$, in agreement with the values $\omega_0 = 528 \text{ cm}^{-1}$ and $\gamma = -4.24 \text{ cm}^{-1}$ reported earlier [152]. The data and the fit are shown in Figure 6.4 left inset.

6.4. Additional influences

Graphene Raman spectra are not only influenced by the local disorder or temperature. If the graphene is stretched, the carbon-carbon distance becomes longer and all phonons soften [109]. If the expansion due to strain is only in one direction, the G-band splits into two peaks, corresponding to a parallel and a perpendicular phonon mode. Further, the D-band intensity due to electron scattering on an edge is largely dependent on the edge structure [109, 110]. Scattering on a zigzag edge is an intravalley process and thus does not add to the D-band, whereas scattering on an armchair edge is an intervalley process and thus contributes to the D-band. Moreover, armchair edges show the strongest D-peak if the incident laser light is polarized along the edge. The ratio between the maximum and the minimum intensity (depending on the laser polarization) is used as a measure of the edge disorder [109].

Another important effect arises from the Kohn anomalies in graphene. The process described in section 4.3 is strongly dependent on the doping of the graphene as illustrated in section 6.4. The generation of an electron-hole pair is only possible as long as the phonon energy is at least twice the Fermi energy $\hbar\omega_0 \geq 2|E_F|$. Otherwise no free states are accessible. Thus, at high doping electron-phonon coupling is suppressed leading to a stiffening of the G-band accompanied by a narrowing of the peak due to a longer phonon lifetime [110, 145]. For the D- and 2D-band this process is suppressed due to momentum conservation.

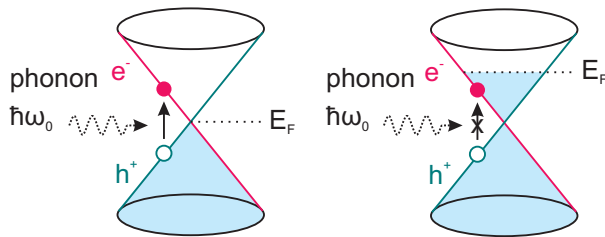


FIGURE 6.5.: Generation of an electron-hole pair through the absorption of a phonon at different Fermi energies. The process is only allowed for $\hbar\omega_0 \geq 2|E_F|$ (left panel).

pH sensitivity and chemical functionalization

Physical or chemical adsorption of various molecules has been demonstrated to dope the graphene effectively without reducing its charge carrier mobility [33, 142]. Thus, graphene is predicted to be the ultimate material for sensing- and bioapplications, due to its large surface to volume ratio and special electrical and mechanical properties [102, 153, 154]. One possibility to achieve this goal is the use of graphene field effect transistors (GFETs). Such devices transduce chemical surface reactions into an electrical response via electrostatic gating of the device by chemical or biological species bound to the graphene surface [155–157]. However, to bring these devices towards application, a deeper understanding of the sensing mechanism and specific functionalization are crucial.

In this chapter we will discuss our sensors based on GFETs. We will look at the proton sensitivity of pristine and functionalized graphene as well as specific functionalization for ion sensing. The work described here was lead by Dr. Wangyang Fu. The author of this thesis contributed in the development of the chemical vapor deposition (CVD) of graphene, its transfer and characterization as well as discussions.

7.1. Function principle and experimental setup

We saw in section 5.4 that the graphene conductance can be tuned by applying an electrostatic gate. This gate is coupled to the graphene over the gate capacitance C_g . Sensing in GFETs can be achieved through an electric potential induced by the sensing targets [158]. If graphene is immersed into solution, an electrical double layer forms on top of its surface with a capacitance C_{dl} . The total capacitance to the liquid gate C_{tot} is composed of C_{dl} and the quantum capacitance of graphene C_q in series ($C_{tot} = C_{dl} + C_q$), where $C_{tot} \gg C_g$. Therefore, the transconductance ($\frac{\partial \sigma}{\partial V_{ref}}$, where σ is the conductance and V_{ref} is the liquid potential) is enhanced and the GFET is very sensitive to changes in V_{ref} [158]. If a charged species binds to the graphene

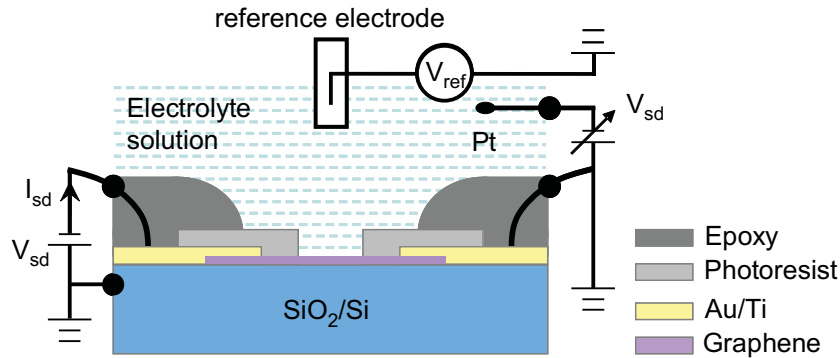


FIGURE 7.1.: Schematics of the experimental setup and the electrical circuitry of the electrolyte-gated GFET. The gate voltage V_g is applied to the solution via a Pt wire. The electrostatic potential V_{ref} in solution is monitored by the reference calomel electrode. Reused with permission from [32]. Copyright 2011 American Chemical Society

surfaces it dopes the graphene and the conductance versus V_{ref} curve is shifted. This is the same principle as used in ion-sensitive field effect transistors (ISFETs) [159]. pH sensing for example can be described through the side-binding model [160]. In this model, the terminal OH groups on the surface can be neutral in the form of OH, protonized to OH_2^+ or deprotonized to O^- . At a large pH the equilibrium is shifted towards a deprotonized surface which is negatively charged. As a consequence, the transfer curve (which is the current through the FET vs. the gate voltage) is expected to shift to more positive voltage.

GFETs are fabricated from CVD grown graphene, which was transferred onto a Si/SiO₂ wafer (see chapter 5 for details). Standard photolithography is used to define metal contacts. To operate the device in electrolyte environment it is sealed with a micrometer-sized liquid channel (made of photoresist AZ2070 nlof) and an epoxy layer (Epotek 302-3M, Epoxy Technology) after wire bonding. As electrolyte we use standard pH buffer solutions (Tritisol pH 2 – 9, Merck). The solutions were purged with pure N₂ for 2 h before measurement. The gate voltage V_g is applied through a platinum wire and the electrostatic potential in the solution is monitored by a commercial calomel reference electrode (REF200, Radiometer analytical). Electrical conductance is measured with a small source-drain voltage (V_{sd}) of 10 mV to 50 mV applied. For this a Keithley 2600A source meter is used. For the measurements shown, the current between the platinum wire and the graphene was never exceeding 10 nA and is thus at least two orders of magnitude lower than the source-drain current I_{sd} . Figure 7.1 provides a cross-sectional view on the device together with a schematic of the electrical circuit.

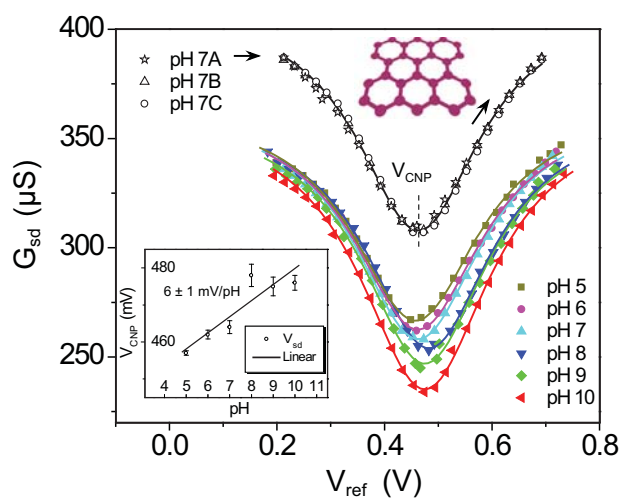
7.2. Passivation and pH sensitivity

Proton sensing with GFETs has been demonstrated by various groups, however the values reported for the pH sensitivity reach from 12 mV/pH to 99 mV/pH [155, 156, 161, 162]. This later value is even higher than the theoretical maximum (59.2 mV/pH at room temperature), predicted by thermodynamics, the Nernst limit [163]. As already mentioned, this shift is due to the reaction of protons with the OH groups of the sensor surface. As a perfect graphene surface does not exhibit any OH groups, a GFET should be insensitive to a pH change in the solution. To resolve this discrepancy we looked at variably functionalized GFETs.

Figure 7.2 shows the transfer curves of the liquid gated GFET for different pH buffer solutions. An ambipolar behavior typical for graphene is observed. The data in the upper part of the Figure 7.2 serves to illustrate the excellent degree of reproducibility (these curves are vertically shifted for clarity). The transfer curves are fitted with a Gaussian curve to extract the reference voltage V_{CNP} at which the source-drain conductance (G_{sd}) is minimal. The dependence of V_{CNP} versus pH is plotted in the inset. V_{CNP} shifts to higher voltages, with decreasing proton concentration, in agreement with the side binding model [160]. We find a sensitivity of 6 ± 1 mV/pH, which is considerably smaller than that found by other groups [155, 156, 161, 162].

The observed pH sensitivity can be reduced by passivating the graphene surface with molecules. It has been shown that small conjugated molecules can bind to graphene with a binding energy of $\approx 0.5 - 1$ eV [164, 165]. For the passivation, the device is rinsed in fluorobenzene for 30 s and is dried. As compared to the as-prepared device, no pH shift is observable (< 1 mV/pH, see Figure 7.3 left panel). Until now we kept the graphene surface as hydrophobic as possible. To increase the pH response, we functionalize the surface with OH groups. For this we grow a thin aluminum oxide (Al_2O_3) layer on top of the graphene using atomic layer deposition (ALD, Savannah

FIGURE 7.2.: G_{sd} as a function of V_{ref} measured in different pH buffer solutions for the as-prepared GFET. The transfer curve shifts to more positive V_{ref} with increasing pH, as specified in the inset. A sensitivity of 6 ± 1 mV/pH is deduced. Error bars represent the standard deviation from three subsequent measurements taken for each pH value. As an example, the three data sets obtained for pH 7 are shown on the top. Reused with permission from [32]. Copyright 2011 American Chemical Society



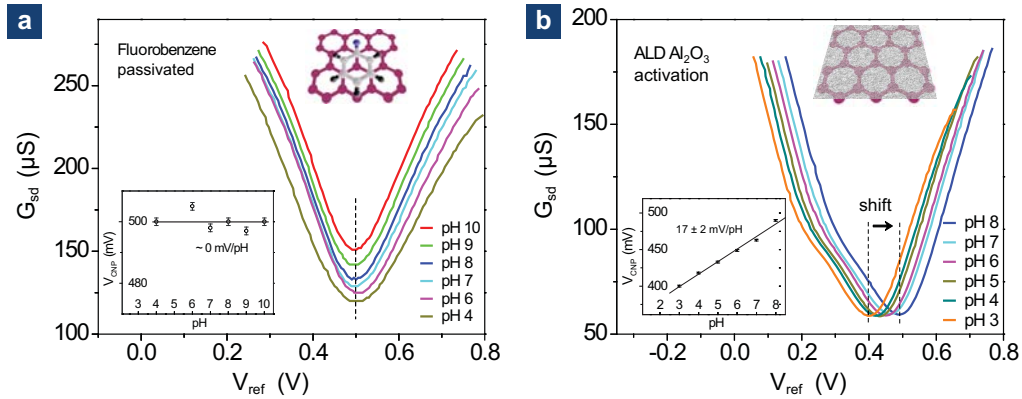


FIGURE 7.3.: Transfer curves for a GFET **a** passivated with fluorobenzene and **b** activated with a Al_2O_3 ALD coating. For **a** no shift of V_{CNP} with pH is observed. For **b** V_{CNP} shifts with 17 mV/pH. Reproduced by permission from [32]. Copyright 2011 American Chemical Society

100 from Cambridge NanoTech). We apply a protocol that involves the activation of the graphene with nitrogen dioxide at room temperature before growth, using trimethylaluminum as precursor gas [166]. Because of the non optimal wetting on graphene the layer is expected to be < 2 nm and may even be discontinuous. After depositing the ALD layer we found a pH sensitivity of 17 mV/pH (see Figure 7.3 right panel). In the case of an Al_2O_3 layer with a large density of hydroxyl groups a sensitivity of ≈ 40 mV/pH is expected [159]. We ascribe the reduced sensitivity found in our experiments to the possibly low quality of the Al_2O_3 layer.

These measurements reveal a clear systematic. Adding OH groups to the surface increases the pH sensitivity, whereas for a hydrophobic coating the sensitivity goes to zero. This suggests that the fluorobenzene molecules are able to suppress the chemical activity of residual free bonds due to defects in the graphene. This picture leads to the conclusion that indeed the ideal defect free graphene surface should have no pH response. In practice however, some defects will always be present, yielding in a reduced pH sensitivity. Measuring the pH sensitivity of a device fabricated with exfoliated graphene lead to a sensitivity of 8 ± 1 mV/pH. This is similar to the 6 ± 1 mV/pH measured for CVD graphene. This is a further proof for the excellent surface quality of CVD graphene.

7.3. Non-covalent functionalization

We have shown in Ref. [32] (see section 7.2) that perfect graphene is chemically inert and that proton sensing can be activated by adding an oxide layer. To unlock the potential of graphene for sensing applications with GFETs for other species, as ions

or proteins, functionalization of graphene with specific recognition moieties is needed. Various functionalization schemes were already published, ranging from covalent to non-covalent methods [158]. However, it is not clear to what extent the extraordinary electrical properties of graphene are preserved through these processes. Thus it is important to test the mobility of GFETs before and after functionalization.

The devices are fabricated using CVD graphene on Cu (see chapter 5). The graphene is etched into shape directly on the Cu foil and then glued on a glass substrate using epoxy (Epotek 302-3M, Epoxy Technology) with the copper facing upwards. Then the copper is etched using a 0.1 M ammonium persulfate solution. Silver paint is used to contact the graphene device and the contacts are sealed with epoxy. Using this fabrication scheme the upper graphene surface stays free of resist residues. This is important because resist contaminations could hinder surface functionalization. The samples are measured in liquid environment with same setup as described in section 7.1 and Figure 7.1.

As mentioned in section 7.2 we use fluorobenzene to passivate our GFETs. First we want to demonstrate that a similar technique can be used to activate the proton sensitivity of a GFET. For this phenol is used to functionalize the graphene surface by $\pi - \pi$ stacking. This is done by immersing a fresh GFET into a 1 M solution of phenol in ethanol during 5 min. Afterwards the sample is rinsed in ethanol for another 5 min. The small phenol molecules are chosen, as a higher density of OH groups is expected in comparison to larger molecules. The electrical transfer curves for a phenol-activated (top panel) and a fluorobenzene-passivated device are shown in Figure 7.4. The sheet conductance G_s is measured in a van der Pauw configuration $G_s = \frac{\ln(2)}{\pi} \frac{I_{12}}{V_{34}}$. For the phenol-activated device a shift of V_{CNP} to the right with

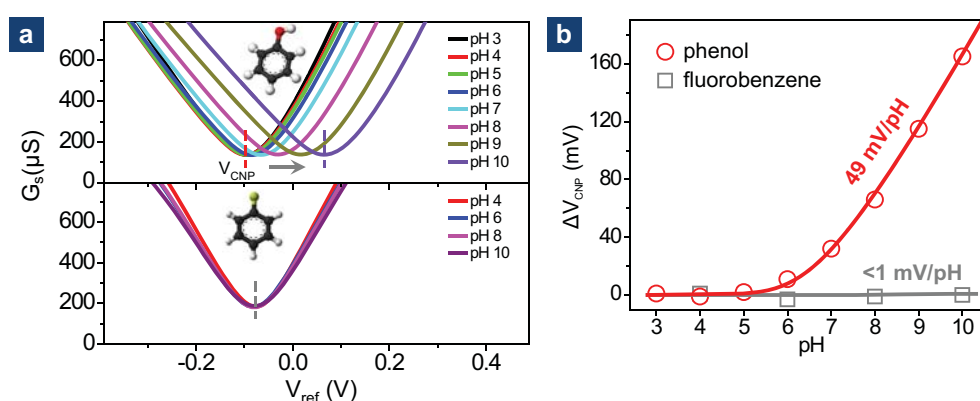


FIGURE 7.4.: pH response of GFETs with phenol and fluorobenzene functionalization. **a** G_s versus V_{ref} measured in different pH buffer solutions for phenol-activated (top panel) and fluorobenzene-passivated (lower panel) devices. **b** Change of the surface potential Φ_0 versus the pH of the buffer solution. The red curve is a fit to the single-reaction model. [33] Reproduced by permission of The Royal Society of Chemistry (RSC)

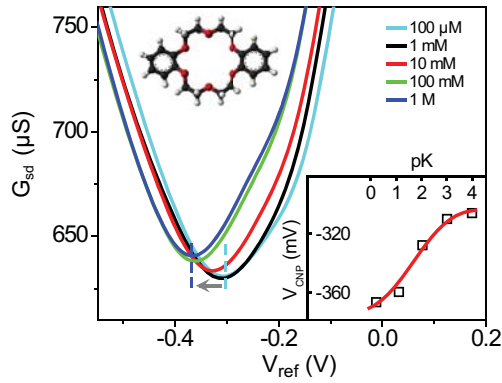


FIGURE 7.5.: Response of a crown ether-functionalized GFET to K^+ ions. G_{sd} versus V_{ref} measured at different K^+ concentrations. The inset shows the change of the V_{CNP} . [33] Reproduced by permission of The Royal Society of Chemistry (RSC)

higher pH is observed, whereas no shift is observed for the fluorobenzene-passivated device. In the right panel of Figure 7.4 the shift of the CNP ($\Delta V_{CNP} = V_{CNP}(\text{pH}) - V_{CNP}(\text{pH}=3)$) of the GFET is depicted as a function of pH for the two different functionalizations. As expected no pH response ($< 1 \text{ mV/pH}$) is observed for the passivated device. On the other hand, the GFET decorated with phenol molecules shows a nonlinear pH response. It is flat in the beginning and rises with a slope of 49 mV/pH at $\text{pH} > 8$, similar as for Al_2O_3 surfaces [159].

Finally, to demonstrate ion sensing, the GFET is functionalized in 0.1 M solution of dibenzo-18-crown-6-ether in chloroform for 5 min and then rinsed in ethanol for 5 min. Potassium chloride (KCl) solutions (in deionized water) at concentrations from $100 \mu\text{M}$ to 1 M are used for the measurements. For all concentrations the pH remained constant at 5.5. The source-drain conductance (G_{sd}) versus V_{ref} at different potassium ion (K^+) concentrations is shown in Figure 7.5. The position of the CNP shifts toward negative potential with increasing K^+ concentration. The shift of V_{CNP} is plotted in the inset as a function of pK , which is the negative logarithm of the K^+ concentration. As fabricated GFETs do not show a significant K^+ sensitivity ($< -3 \text{ mV}$).

The aromatic functionalization does not only endow the GFETs with a significant pH or K^+ response, but also preserves the high graphene mobility. For six samples we measured the electron and hole mobility before and after functionalization. Only for two samples a reduction of the electron mobility by $\approx 20\%$ and once a reduction of the hole mobility by $\approx 15\%$ was observed. In all other cases the mobility changed by less than 10% or was even enhanced after functionalization. This shows that aromatic functionalization preserves the excellent electrical properties of graphene while adding specific sensitivity.

Controlled burning of graphene devices

The use of graphene as an electrode material has been proposed to be the future of molecular electronics [167] and has been the subject of various theoretical studies [165, 168–170]. First experiments using carbon nanotubes (CNTs) [24–26], few-layer graphite [27–29] and chemical vapor deposited (CVD) graphene [30, 31] to contact molecules show that using materials made from sp^2 carbon is indeed a promising approach. The electrodes are claimed to be stable and allow gating, optical and chemical access. Furthermore the topography can be accessed by scanning probe techniques. Two main approaches are used to fabricate these electrodes. One is the so-called electroburning (EB), where the current in a system is increased until electrical breakdown [25, 27]. So far, electrodes fabricated through EB showed a limited yield, reaching at the very best 50% [25, 171]. The other approach is beam-based lithography. A fine patterning of graphene is possible using advanced beam-based nanofabrication and in particular via helium-ion-beam lithography (HIBL), see e.g. Refs. [172, 173]. The fabrication of nanoscale gaps via direct cutting of CNTs using HIBL was for instance very recently demonstrated [26]. We tested the influence of HIBL on the graphene Raman spectra. This study is shown in [appendix E](#). Carbon electrodes have also been fabricated using electron-beam based methods [24, 30]. Beam-based techniques remain however delicate to control for gaps below 5 nm and an improvement of the yield comes at the cost of increased complexity and lower speed [174].

CVD graphene (see [chapter 5](#)) allows graphene production on a larger scale. This is a prerequisite to gather the large statistics required in molecular electronics investigations. For the use as electrodes, small gaps in a graphene constriction need to be fabricated. We focus on the development of an EB process of CVD graphene with a high yield.

In this chapter we will review the idea of EB and look at the changes in the electrical properties of graphene due to Joule heating. We will discuss the experimental requirements for EB, characterize the graphene gaps and look at the yield of the process. Additionally, we will show the evolution of the temperature during gap formation deduced from Raman spectroscopy measurements and EB performed simultaneously.

8.1. The idea behind

It is well known that controlled electromigration of metals, the movement of atoms due to momentum transfer of high energy electrons, can lead to nm-spaced gaps, suitable to contact molecules [175–177]. A similar technique can be used to fabricate small gaps in CNTs and graphene [171, 178]. However, the underlying process is different in this case.

At high bias, a current saturation was observed for CNT [178, 179] and graphene FETs [117, 180, 181]. This effect can be explained by scattering of the charge carriers on SiO₂ surface phonons [180] or graphene optical phonons [181]. The resulting heating is called Joule heating. For graphene, the tendency of the current I to saturate at high bias voltages V_b changes with the applied gate voltage V_g as shown in Figure 8.1. At high electron densities more scattering occurs and the heating effect is stronger. If the current is raised further, electrical breakdown occurs and the graphene breaks. In high vacuum, the mechanism is a current induced sublimation of the carbon atoms [182, 183]. In the vicinity of oxygen, the breakdown is likely to be a consequence of the oxidation of carbon atoms, triggered by the local self-heating caused by the large current densities [25, 27, 178]. Thus the process can be controlled by adjusting the partial oxygen pressure [25]. A constriction in the graphene leads to a local heating, as the current density is the highest at the constriction [149]. This gives a possibility to control the position where the EB takes place. To test how well the heating is localized at a graphene constriction, Raman spectroscopy can be used as it has been shown to act as a local thermometer for graphene [147] (see section 6.2). We performed Raman scans on a constriction (400 nm in width and 800 nm in length) while applying a bias. Figure 8.2 shows the shift of the graphene 2D-band in respect

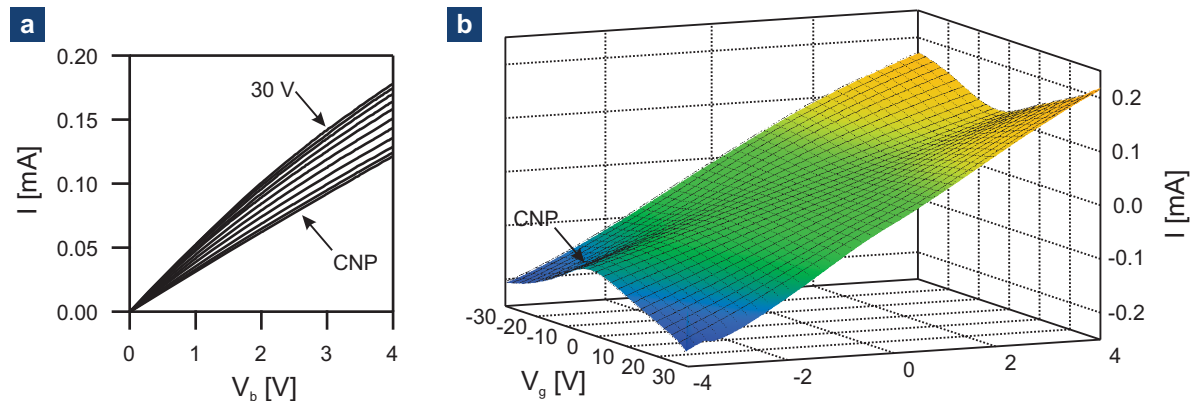
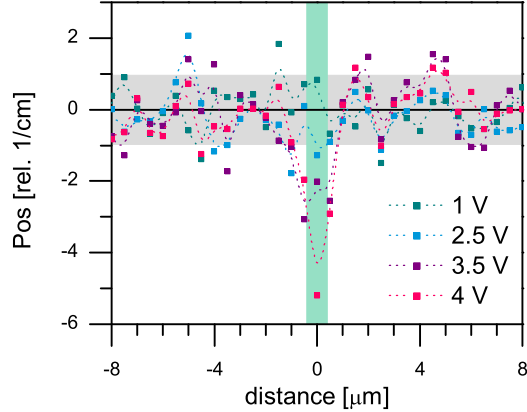


FIGURE 8.1.: **a** I versus V_b characteristics at different V_g , from 2.5 V (CNP) to 30 V (step size = 2.5 V). **b** Surface plot of I as a function of V_b and V_g . The CNP is observed at ≈ 2.5 V. Measured on a graphene FET in vacuum.

FIGURE 8.2.: Shift of the 2D-band (in respect to $V_b = 0.5$ V) versus the distance from a graphene constriction heated over Joule heating at different V_b . The data is plotted as squares were a spline serves as a guide to the eye. The junction area is emphasized as a turquoise background, the gray area shows the standard deviation of all data points.



to its position when $V_b = 0.5$ V, as a function of the distance from the constriction and at different bias ($V_b = 1.0, 2.5, 3.5, 4.0$ V). The data is plotted as squares where a spline serves as a guide to the eye. The light turquoise area illustrates the dimension of the constriction while the gray area shows the standard deviation of all data points. We chose $V_b = 0.5$ V as the reference as we do not expect substantial heating at this bias (see also [Figure 8.1](#)). The measurements are performed with the device in the p-doped regime at a high charge carrier density. As the laser spot size of our Raman microscope is ≈ 400 nm the resolution of our system is really at the edge of resolving the constriction. For $V_b = 1.0$ V and $V_b = 2.5$ V no shift substantially higher than the noise floor is observed. For $V_b = 3.5$ V a slight shift to lower values is observed directly at the constriction. This shift becomes more clear for $V_b = 4.0$ V, which corresponds to a temperature increase of ≈ 100 K. As no large shifts are observed outside the constriction area, these measurements are in agreement with a scenario where the heating is localized to the constriction. To really prove this, measurements with a better resolution would be needed.

8.2. Sample and electro burning setup

For our samples we use single-layer graphene obtained from CVD growth on copper [\[34–36\]](#) and transferred onto doped silicon substrates coated with 300 nm of thermal oxide [\[35, 125, 132\]](#). Patterning is done either using electron-beam-lithography or UV-lithography, followed by argon/oxygen plasma etching. The graphene is shaped into 400 nm to 600 nm or $2 \mu\text{m}$ wide constrictions. Contacts are patterned by an additional lithography step followed by the evaporation of 40 nm of gold with a 5 nm titanium adhesion layer. The details of the fabrication are given in [appendix I](#). In contrast to the required custom design for samples made from exfoliated graphene, the same predefined masks can be used to produce 100 - 400 devices on one chip with our CVD graphene process. An optical image of a device and a scanning electron

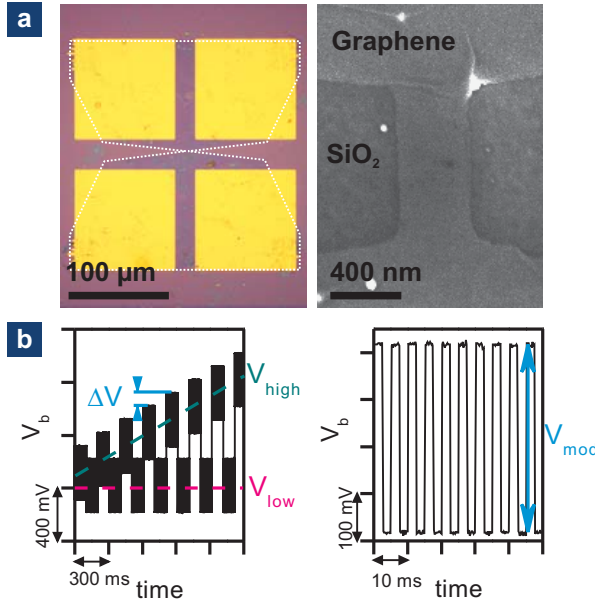


FIGURE 8.3.: **a** Optical (left) and scanning electron microscopy (right) images of a typical sample. The white dashed line in the optical image shows the borders of the graphene flake. **b** Bias voltage V_b during the EB process. We alternate a high bias V_{high} and low bias V_{low} voltage superposed with a modulation V_{mod} to measure the differential resistance. V_{high} is increased in steps of ΔV . [150] Reproduced by permission of The Royal Society of Chemistry (RSC)

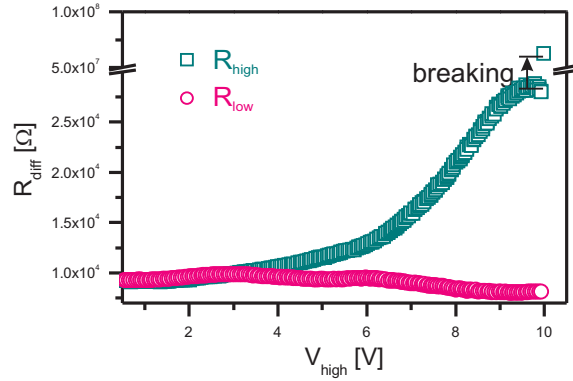
microscopy (SEM) picture of a constriction is shown in [Figure 8.3](#) top panel. The wider devices are used for Raman spectroscopy performed at the same time as the EB procedure. The initial resistance of the devices at low bias and floating back gate is typically between $2\text{ k}\Omega$ and $20\text{ k}\Omega$.

To burn the graphene constrictions a process was adapted from previous studies on gold electromigration [177]. The bias voltage is alternated between a high and a low value (V_{high} and V_{low}) to which a modulation (V_{mod}) is superimposed to measure the differential resistance ($R = \frac{\Delta I}{V_{mod}}$, where I is the measured current) at high bias (R_{high}) and at low bias (R_{low}). Both, V_{low} and V_{mod} are set to 0.4 V . V_{high} is ramped stepwise with $\Delta V = 0.1\text{ V}$, as shown in [Figure 8.3](#) lower panel. The alternating bias voltage V_b allows us to distinguish between effects which change the resistance of the graphene constriction and affect both R_{high} and R_{low} from Joule heating which only influences R_{high} . The whole process is done in vacuum, at a pressure of $\approx 1 \cdot 10^{-5}\text{ mbar}$ to reduce the amount of oxygen close to the sample.

8.3. Heating influence on electrical properties

We first investigate the heating process in the junction. [Figure 8.4](#) shows the evolution of R_{high} and R_{low} for a typical burning process of a highly doped sample. R_{high} increases, whereas R_{low} stays almost constant. We observe this until the graphene bridge breaks and R_{high} jumps to a high value (arrow), faster than the time resolution of our setup (which is 10 ms). With the setup used for breaking, this resistance value can not be resolved anymore and just represents the noise level (detection limit

FIGURE 8.4.: Differential resistance at high bias R_{high} (dark cyan squares) and low bias R_{low} (pink circles) during EB of a device. [150] Reproduced by permission of The Royal Society of Chemistry (RSC)



≈ 50 nA). At this point V_b is set back to 0 V. The graphene constrictions are burned in a single step without the use of a feedback procedure for the bias voltage. EB was preformed in 2-terminal and 4-terminal measurements, but no difference in the resistance behavior during EB could be observed. The contact resistance is in the order of a few hundred Ohms and thus an order of magnitude smaller than the graphene resistance. The current needed to break the constriction increases with increasing constriction width. The breakdown current observed is ≈ 1 mA per μm width in agreement with literature [181, 184, 185].

Figure 8.5 (left panel, black symbols) shows the gate behavior of graphene constrictions right after fabrication, where the different symbols represent two different devices. The charge neutrality point (CNP) can be clearly seen at a gate voltage $V_g \approx -50$ V for the first device, and is close to 0 V for the second. This is due to slight differences in the fabrication process, leading to distinct surface doping. If the EB procedure is applied, but stopped before the electrical breakdown, the behavior of R versus V_g changes dramatically for the heavily doped sample. Additional peaks appear at ≈ -15 V and ≈ 45 V. We attribute this effect to the redistribution of surface contaminants. It has been shown, that applying high current densities can move particles on top of the graphene [143, 186]. This results in a cleaning of the graphene surface. In particular cases, this mechanism has been implemented to prepare clean graphene structures showing ballistic transport [104–106].

In our samples, most of the heat is generated at the constriction and contaminants could move away to the colder contact areas. Applying a second heating step does not lead to further significant changes. This is shown in the inset of Figure 8.5. To ensure that the resistance is only influenced by heating and not by doping contaminants, we focus on results for annealed devices, where the EB was performed directly after a heating cycle. Close to the CNP, the resistance is most sensitive to changes occurring through cleaning effects. Thus, if the burning procedure is performed close to the CNP and without a previous cleaning cycle, the resistance behavior can be quite different from the one shown in Figure 8.4. In this case we often observe a decrease in both, R_{high} and R_{low} . After heating, the gate behavior changes within minutes to hours for

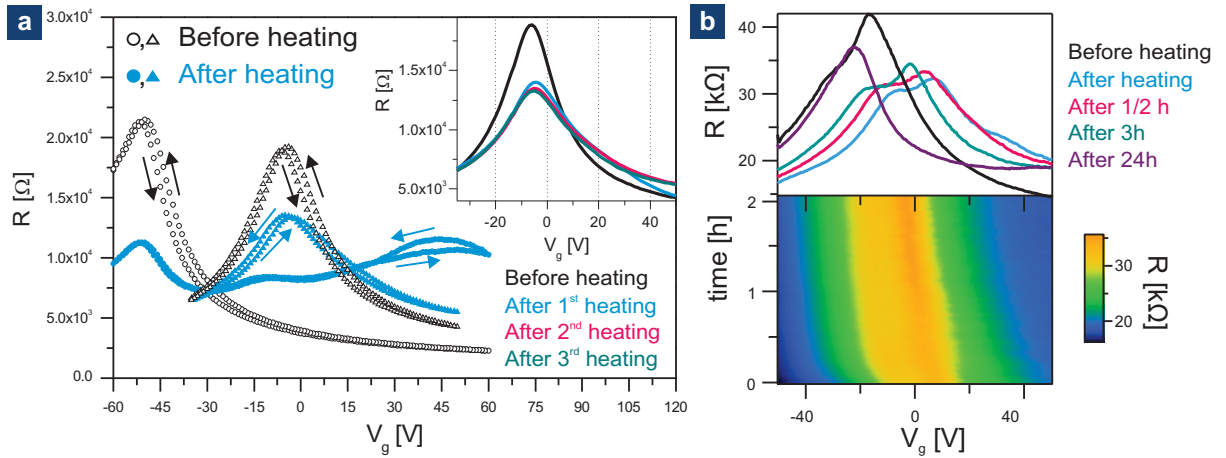


FIGURE 8.5: **a** Gate dependent resistance before (black open symbols) and after (blue solid symbols) heating the sample while performing the EB process but stopping it before breakdown. Two different samples are shown (circles and triangles). The inset shows gate sweeps after a second and third heating step for the second device. **b** Time dependence of R versus V_g after heating in vacuum (10^{-5} mbar). $t = 0$ corresponds to the situation directly after heating. [150] Adapted with permission of The Royal Society of Chemistry (RSC)

samples stored in vacuum at room temperature. This shows that the contaminants can slowly diffuse back to the constriction. This is illustrated in Figure 8.5 right panel, where R after a cleaning procedure is plotted versus V_g and time.

8.4. Small gaps in graphene

After EB the graphene tunnel junctions were further analyzed using Raman spectroscopy, as well AFM, SEM and electrical measurements were performed. The gaps show tunneling characteristics, which can be described through the Simmons model (see section 1.2).

8.4.1. Imaging and Raman spectroscopy

Figure 8.6 top panel shows the Raman spectra on the graphene electrodes (blue) and on the broken constriction (purple). The inset shows an intensity map for the graphene 2D peak. As the resolution of the Raman microscope is ≈ 400 nm, the constriction can only be hardly seen. The spectrum on the graphene electrode shows the signature of monolayer graphene, exhibiting a small defect induced peak (D-band). A larger D-band is observed in the spectrum on the constriction due to scattering at

the edges and/or on defects introduced through the EB process. A slightly enhanced background between the D- and the G-band and a substantial change in the G to 2D intensity ratio is observed at the constriction. This indicates the presence of disordered graphene or amorphous carbon, which could have been created during EB. The SEM image on the right shows the bridge after EB (lighter gray: graphene; darker gray: substrate), the gap is visible as a thin line emphasized by the arrows. We performed a topological analysis of the freshly burned gaps using AFM. For this we used a Dimension 3100 (Veeco, USA) in combination with PPP-NCHR cantilevers, which have a nominal tip curvature < 10 nm (Nanosensors, Switzerland). The measurements were performed with the kind help of Dr. Monica Schönenberger in ambient conditions, where atomic resolution imaging is not possible. This analysis provides an upper limit for the gap size. An image of a typical device is shown in [Figure 8.6](#) lower panel left. A cross section through the graphene channel (lower panel middle, turquoise line) gives an apparent graphene thickness of 0.7 nm, in agreement with the thickness for monolayer graphene reported in the literature [137, 187]. We measured cross sections along different positions on the gap (two examples shown in the right

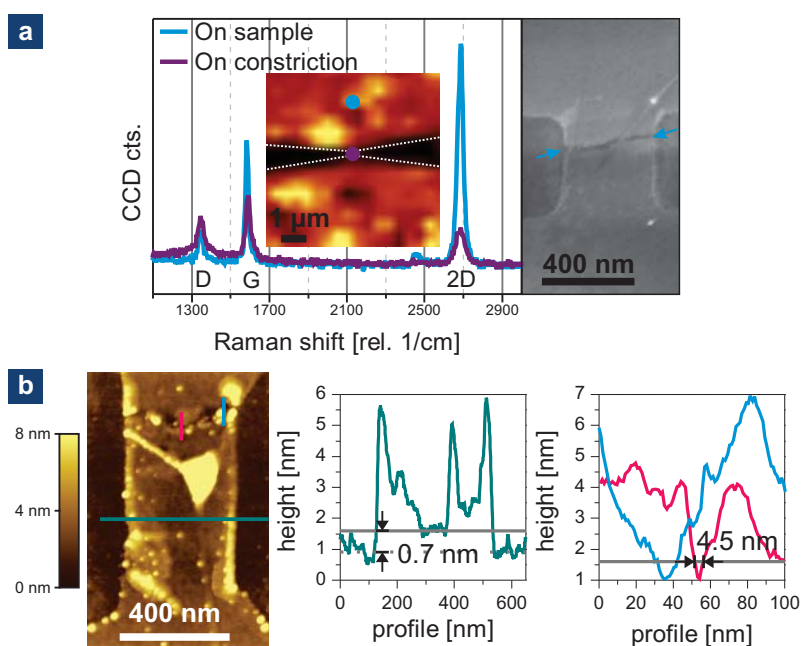


FIGURE 8.6.: **a** Raman spectra recorded on the graphene electrode (blue) and on the burned constriction (purple). The inset shows a map of the integral over the graphene 2D-band, where the white dashed line shows the border of the graphene. A SEM image of the graphene constriction after EB (lighter gray graphene, darker gray substrate) is shown on the right. **b** AFM image and height profiles across the graphene channel and over the gap. The gap size is estimated to be 4.5 nm wide. [150] Reproduced by permission of The Royal Society of Chemistry (RSC)

lower panel). The gap size is measured at the graphene height (determined from the cross section over the graphene channel). The narrowest slit was found to be ≈ 4.5 nm wide. These measurements also show that the gap size is not homogeneous along the slit. This value is rather an upper boundary than an exact number, as tip convolution can affect the recorded topography.

8.4.2. Electrical measurements

In [Figure 8.7](#) (left panel), current-voltage characteristics for a typical sample are plotted. Before breaking (blue, right axis) the sample shows a linear behavior with a resistance of $13,8$ k Ω . After EB (purple, left axis), the device shows S-shaped $I - V$ curves characteristic for tunneling. The linear fit to the low bias part (± 0.3 V) yields a 220 M Ω resistance. Assuming a rectangular barrier, the tunnel curves can be fitted with the Simmons model [42] (see [section 1.2](#)). As we have seen in [section 1.2](#) this model is only valid for small V_b . To determine the limits for the fitting, transition voltage (V_T) spectroscopy is used (as described in [section 1.2](#)). The corresponding plot of $\ln(I/V^2)$ versus $(1/V)$ (Fowler-Nordheim plot) and the Simmons fit to the corresponding low bias region are shown in [Figure 8.7](#), right panel device 1 for $V_T = \pm 0.4$ V. The values deduced from this fit are as follows: area $A_{\square} = 0.35$ nm², gap size $d = 1.3$ nm and potential barrier height $\Phi_b = 0.26$ eV. The parameters A_{\square} and Φ_b are quite sensitive to changes in the fitting range and the initial parameter set. For a small initial A_{\square} , a local minimum is found. If a high initial A_{\square} is chosen, the fit diverges. For the fit described above a small initial A_{\square} was chosen. However, the parameter d seems to be more robust.

We now also look at two additional devices showing different resistances than device 1. The resistance of the devices is determined from a linear fit to the low bias region (± 0.3 V). We obtain 19 G Ω and 100 G Ω for devices 2 and 3, respectively. The fitting region is again determined by V_T deduced from a Fowler-Nordheim plot. For the curves presented, we find $V_T = 0.6$ for device 2 and $V_T = 1.25$ V for device 3. The fits with free parameters and small initial A_{\square} to the three curves are shown in [Figure 8.7](#). The corresponding fit parameters are given in [Table 8.1](#) for all three devices. For these fits, d is about the same for all devices. The difference in resistance R between the junctions is accounted for by changes in A_{\square} . For all three devices, A_{\square} is small as compared to the maximum possible area of ≈ 100 nm² in our case (constriction width times atom diameter). This could indicate that the gap is not homogeneous in width over the gap length, which is in agreement with the analysis of the gaps by AFM. However, the area A_{\square} derived for device 3 is less than 1 Å² which is not realistic. One would expect Φ_b to maximally be the work function of graphite, which is 5 eV. We however obtain much lower values for Φ_b . This has been observed as well for multilayer graphene tunnel junctions [27] and electromigrated gold junctions [188] and has been attributed to the presence of adsorbates or defects.

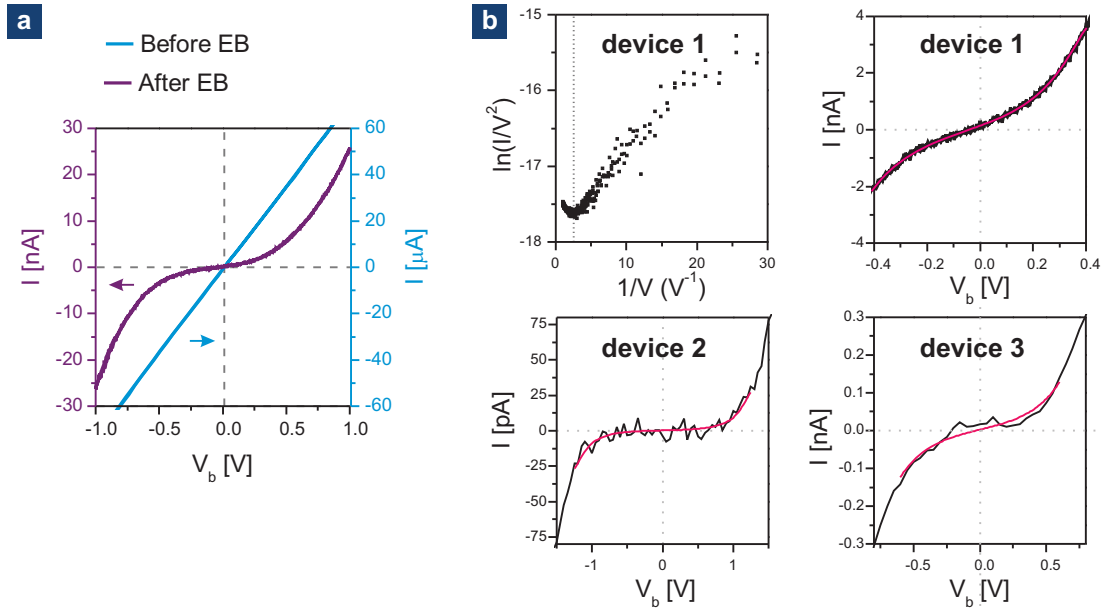


FIGURE 8.7.: **a** $I - V$ curves before (blue, right axis) and after (purple, left axis) the breaking process. After the breaking tunneling behavior is observed. **b** $\ln(I/V^2)$ versus $(1/V)$ (left panel) and low bias region with Simmons fit (right panel) of the same curve as in **a**, as well as the $I - V$ characteristics of two additional devices. The curves are corrected for the offset of the current-voltage converter. [150] Reproduced by permission of The Royal Society of Chemistry (RSC)

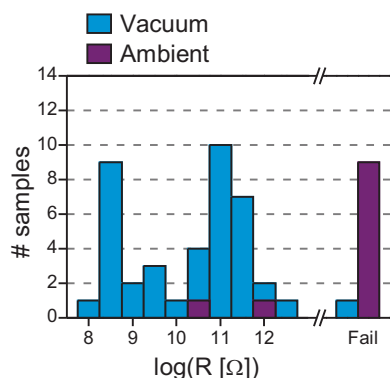
To demonstrate the robustness of d , we fit the curves to the Simmons model for a fixed area. For this we choose either $A_{\square} = 100 \text{ nm}^2$, which is approximately the maximum possible area for our devices or $A_{\square} = 0.01 \text{ nm}^2$, which would be comparable to the size of a single atom. Even with these extreme assumptions for A_{\square} and letting d and Φ_b free, d remains between 0.4 nm and 1.9 nm for all three devices. To test the robustness of d further, we additionally fix Φ_b at either 5 eV (approximately the work function of graphite) or at eV_T . For an energy barrier smaller than eV_T , the Simmons model would not be appropriate anymore. For these fits we get values for d between 0.3 nm and 2.2 nm. Overall, although this procedure can not provide a true physical value, it allows to determine a limit for the gap size, being between 0.3 nm and 2.2 nm. A narrow distribution of the gap size is expected as the current depends exponentially on the distance between the electrodes. A change in the gap size would lead to a much larger change in the tunnel current and it would not be measurable anymore for large d .

Of the 50 samples burned in vacuum ($1 \cdot 10^{-5}$ mbar), 49 showed measurable tunnel current after EB, corresponding to a yield of 98%. If a device did not show a tunneling current (we set the limit at 10 pA for ± 10 V bias), it is considered as fail. To test

TABLE 8.1.: Fit parameters for the devices shown in [Figure 8.7](#). The resistance obtained from a linear fit (± 0.3 V and the threshold voltage (V_T) as derived from transition voltage spectroscopy are given in the top line. V_T is used as the limit for the Simmons fits. [150] Reproduced by permission of The Royal Society of Chemistry (RSC)

device 1: $R = 220 \text{ M}\Omega$, $V_T = 0.40 \text{ V}$			
fixed parameters:	A_{\square}	Φ_b	d
none	0.35 nm^2	0.26 eV	1.3 nm
A_{\square}	100 nm^2	0.58 eV	1.6 nm
A_{\square}	0.01 nm^2	1.05 eV	0.4 nm
A_{\square}, Φ_b	100 nm^2	5 eV	0.6 nm
A_{\square}, Φ_b	0.01 nm^2	5 eV	0.3 nm
A_{\square}, Φ_b	100 nm^2	0.4 eV	2.1 nm
A_{\square}, Φ_b	0.01 nm^2	0.4 eV	0.5 nm
device 2: $R = 19 \text{ G}\Omega$, $V_T = 0.60 \text{ V}$			
fixed parameters:	A_{\square}	Φ_b	d
none	0.02 nm^2	0.35 eV	1.3 nm
A_{\square}	100 nm^2	0.78 eV	1.9 nm
A_{\square}	0.01 nm^2	0.34 eV	1.2 nm
A_{\square}, Φ_b	100 nm^2	5 eV	0.8 nm
A_{\square}, Φ_b	0.01 nm^2	5 eV	0.4 nm
A_{\square}, Φ_b	100 nm^2	0.6 eV	2.2 nm
A_{\square}, Φ_b	0.01 nm^2	0.6 eV	0.9 nm
device 3: $R = 100 \text{ G}\Omega$, $V_T = 1.25 \text{ V}$			
fixed parameters:	A_{\square}	Φ_b	d
none	0.002 nm^2	0.65 eV	1.2 nm
A_{\square}	100 nm^2	1.35 eV	1.8 nm
A_{\square}	0.01 nm^2	0.81 eV	1.3 nm
A_{\square}, Φ_b	100 nm^2	5 eV	0.9 nm
A_{\square}, Φ_b	0.01 nm^2	5 eV	0.5 nm
A_{\square}, Φ_b	100 nm^2	1.25 eV	1.9 nm
A_{\square}, Φ_b	0.01 nm^2	1.25 eV	1.0 nm

FIGURE 8.8.: Statistical results of the EB process for vacuum and ambient conditions. The samples are sorted into two parts whether they show tunneling current between ± 10 V or not (failed). The resistance given results from a linear fit ± 0.3 V. [150] Reproduced by permission of The Royal Society of Chemistry (RSC)



the influence of oxygen we also performed EB at ambient conditions. From the ten samples burned in ambient conditions, only two showed a tunneling behavior. This, together with previous studies [25], indicates that the control of the partial pressure of oxygen is crucial for a successful EB procedure. As a control we burned 5 samples in N_2 . None of these devices showed tunneling behavior. This means that either the oxygen partial pressure was still too high or that the amount of N_2 also plays a role. Further experiments are needed to resolve this issue. One interesting approach would be the injection of O_2 pulses to not only control the speed but also the moment of the reaction.

If the EB process was successful a linear curve was fitted to ± 0.3 V to extract the final resistance. These final resistances range from $100\text{ M}\Omega$ to $100\text{ G}\Omega$, and are plotted in a logarithmic scale. The statistics for samples burned in vacuum and samples burned in ambient are shown in Figure 8.8. Our results show the very good reproducibility of the experimental approach implemented, which provides final resistance values after burning similar to what was observed for devices starting with few-layer graphene [27]. Our approach presents the major advantages to provide a very high yield and is based on single-layer CVD graphene which makes a large-scale fabrication possible.

8.5. Temperatures during electroburning

We saw in section 6.2 that the graphene Raman peaks shift with temperature. This effect can be used to determine the temperature of the graphene during the EB procedure. The spectra in the region of the 2D peak recorded during EB are plotted in Figure 8.9, the color code shows the increasing heating power P_{el} . A clear shift of the graphene 2D peak to lower wavenumbers is observed, highlighted by a dashed line. We note that the peak intensity decreases with increasing P_{el} due to focus drift during the measurement. The correction for this effect is discussed in appendix C. The corrected shift of the graphene 2D peak with P_{el} is shown in Figure 8.9 (top right)

panel, dots). Note that the power here is larger than in Figure 8.4 as we are now dealing with wider graphene constrictions to enable a better Raman performance. Applying our calibration of $-0.051 \text{ cm}^{-1}\text{K}^{-1}$ to this data leads to temperatures up to 570 K before the electrical breakdown, as plotted in Figure 8.9 (top right panel, blue squares). Graphene oxidation has been found to start at $\approx 470 \text{ K}$ and etch pits form spontaneously at $\approx 720 \text{ K}$ [189], which agrees well with our findings. The power needed to break the graphene is substantially higher in vacuum where values of 1000 K for supported and 2000 K for suspended graphene were reported [116, 190]. We note that this approach provides a temperature averaged over the laser spot size ($\approx 400 \text{ nm}$ diameter here). It is thus well possible that the effective temperature locally exceeds the values reported.

We now turn to the temperature behavior of the resistance in our devices. The heat generated in the constriction can be dissipated over different pathways, including the environment, the electrodes and the substrate. The heat flow to the environment can be assumed to be small, especially for the experiments performed in vacuum [116]. In graphene, most of the heat is relaxed over electron-phonon scattering [112]

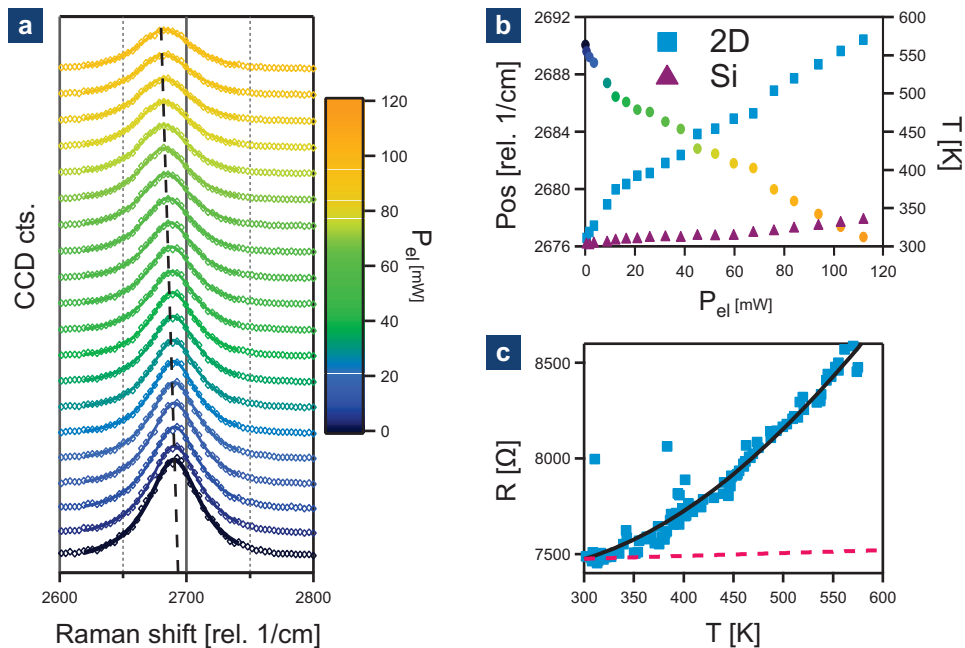


FIGURE 8.9.: **a** Raman spectra around the graphene 2D peak recorded during the EB process. The color code shows the increasing electrical power P_{el} . The dashed line serves as a guide to the eye. **b** Shift of the graphene 2D peak versus P_{el} (dots) (same color code as for **a**) and corresponding graphene (blue squares) and silicon (purple triangles) temperature. **c** Dependence of the graphene resistance on the temperature during EB, as well as a line with a slope of $0.15 \text{ }\Omega\text{K}^{-1}$ (pink dashed) and a fit according to Equation 8.1 (black solid). [150] Reproduced by permission of The Royal Society of Chemistry (RSC)

(see also [section 4.3](#)). The phonon mean free path λ_{ph} of supported graphene at room temperature has been found to be $\lambda_{ph} \approx 100$ nm [111]. We thus assume to be in a diffusive regime for heat transport. Three kind of phonons can contribute to this: acoustic and optical phonons of the graphene as well as remote interface phonons (RIPs) forming at the SiO₂ graphene interface [118–120]. As the electrodes are separated by ≈ 20 μ m we expect most of the heat to be dissipated over the substrate, not at the contacts [111, 116, 117]. This leads to a moderate heating of the whole chip, causing a shift of the Si Raman peak. The corresponding temperatures are plotted in [Figure 8.9](#) top right panel as purple triangles, which shows that for this device the substrate heats up by 34 K. The simplest model considering only scattering via low energy phonons (acoustic) would lead to a linear behavior of $R(T)$. However, if we consider $R(T)$ measured during EB ([Figure 8.9](#) lower right panel), a linear fit leads to a proportionality factor $\alpha = 3.9$ ΩK^{-1} . This value is more than one order of magnitude larger than reported [118, 121]. We therefore consider the following model for the temperature dependence of the graphene resistivity on a SiO₂ surface: [118, 119]

$$\rho(T) = \underbrace{\rho_0}_{\rho_A} + \underbrace{\alpha T + \beta \left(\frac{1}{e^{E_0/k_B T} - 1} \right)}_{\rho_B}, \quad (8.1)$$

where ρ_0 is the residual resistivity at low temperature, E_0 is a phonon energy and α and β are constants. ρ_A is the resistivity due to acoustic phonon scattering and ρ_B is the resistivity due to scattering with optical phonons and/or RIPs. The pink dashed line in [Figure 8.9](#) lower right panel shows the evolution of ρ_A where we used the literature value of $\alpha = 0.15$ ΩK^{-1} [118, 121]. This shows that this term is actually negligible here. Fitting our data to equation 8.1 leads to $\rho_0 = 7349$ Ω , $\beta = 18438$ Ω and $E_0 = 140.7$ meV (black curve). β depends on the carrier density n , which we assume to be approximately constant at high doping. The surface phonons of SiO₂ are predicted at ≈ 59 meV and ≈ 155 meV [118, 119] and the graphene A'_1 phonon, which has the largest electron-phonon coupling, is at ≈ 149 meV [181]. Our value for E_0 is similar to the above phonon energies. This confirms that electron scattering via optical phonons and/or RIPs is dominant in our graphene devices. Note that this analysis is only valid for measurements performed far from the CNP, at a saturating charge carrier density.

In this chapter, we demonstrated an effective procedure for the fabrication of nanometer-sized gaps in monolayer graphene with a very high yield. The use of CVD graphene allows the production of a large number of devices. These achievements are major requirements for the development of graphene-based molecular electronics. Using Raman spectroscopy, we inferred the local temperature at the graphene constriction up to the electrical breakdown. The temperature dependence of the junction resistance is in agreement with a heat dissipation mechanism dominated by

the coupling of the graphene to the substrate. The next step is now to investigate the stability and gate behavior of the graphene electrodes.

Towards molecular measurements

As we demonstrated in [150] (see chapter 8), we developed a simple and reproducible method to fabricate graphene electrodes with nanometer-size separation. The goal is to use them to contact a few to single molecules. To reach this goal, several conditions have to be fulfilled. First, the electrodes have to be stable over time [167, 171]. Furthermore, the electrodes tunneling properties should not be influenced by the application of a back gate voltage [171] or preferably should be individually gateable. The molecules have to bind to the graphene electrodes [165, 170] and should be long enough to bridge the gap reliably.

In this chapter we address the above mentioned issues like stability and gating of the gaps. We also show preliminary results for molecules contacted within our graphene electrodes.

9.1. Stability and gating

We performed long term characterization of our gaps to test their stability. We found that the stability varied from device to device. Whereas some of them survived for 10 days or more, some broke spontaneously after a few hours. Even if a longer lifetimes would be desirable, this is enough to perform molecular measurements. Figure 9.1 shows a color-scale plot of $I - V$ curves recorded over more than two days for a typical device. For this measurement, 20 $I - V$ curves (forward and backward sweep) were recorded fast (ca. 1 s per curve). From these sweeps an average curve is calculated and plotted. Beforehand we also subtract the current offset coming from the current-voltage converter. This procedure is repeated every 30 min. During the whole time the sample was kept under vacuum ($\approx 10^{-5}$ mbar). As there is no difference between the forward and the backward sweep, herein we only show the plots for the forward sweeps. To characterize the device, we mainly look at the bias voltage V_b at which the current increase gets strongly enhanced (current onset). This current onset can be seen by the color change in the color-scale plots. For the device shown in Figure 9.1, the current onset shifts to slightly higher voltages over time, as indicated by a guide to the eye (dotted lines). After 48 hours the

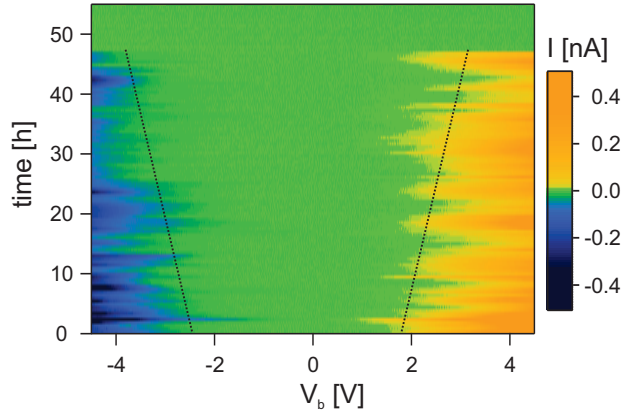


FIGURE 9.1.: Color-scale plot showing drift in the $I - V$ characteristics of a device over time. 20 $I - V$ curves were recorded every 30 min and the average is shown. The dotted line is a guide to the eye for the current onset. After 48 h the conductivity dropped suddenly below the limit of detection (10 pA). The current is plotted in a linear scale with a logarithmic color scale.

device broke spontaneously, not showing any measurable current anymore (± 10 pA at $V_b = 10$ V). The current onset changes almost from curve to curve. We attribute this to sudden changes in the device structure. This can be seen better on curves recorded subsequently as for example in [Figure 9.2](#) right panel (indicated with an arrow). One possible explanation for these instabilities is the folding of graphene as observed by previously [\[185\]](#). The folding could be induced through the large electric field applied over the gap when performing the $I - V$ measurements. Furthermore, applying voltages above 5 V leads to a sudden increase in conductance for $\approx 20\%$ of the curves, where $1 \text{ k}\Omega < R < 1 \text{ M}\Omega$ after the increase. In some cases applying an electrostatic backgate to these devices leads to a similar behavior as for graphene. Since we could have amorphous carbon inside the gaps (see [section 8.4](#)) graphene fusion is a possible explanation. Graphene fusion was already observed earlier under ultra high vacuum conditions for overlapping graphene layers [\[182\]](#). In this paper they show, that in overlapping regions the graphene can heal to form a continuous layer, due to the high temperatures reached through Joule heating. For these junctions, we sometimes observe V_b dependent conductance switching. These effects are further discussed in [appendix F](#).

In principle the gaps do not show any gating behavior directly after burning. However, as the $I - V$ characteristics of the gaps change over time or sudden jumps can occur, it is not easy to distinguish these effects from gating. [Figure 9.2](#) shows gate dependent $I - V$ characteristics of a device different to the one in [Figure 9.1](#). The data on the left panel was recorded as a fast scan (recording time for whole plot 2 min), meaning that one single $I - V$ curve (forward and backward sweep) per V_g is recorded and no averaging is performed. No gating effects, drift or jumps due to instabilities are visible. In the right panel, 40 $I - V$ curves were recorded per V_g value

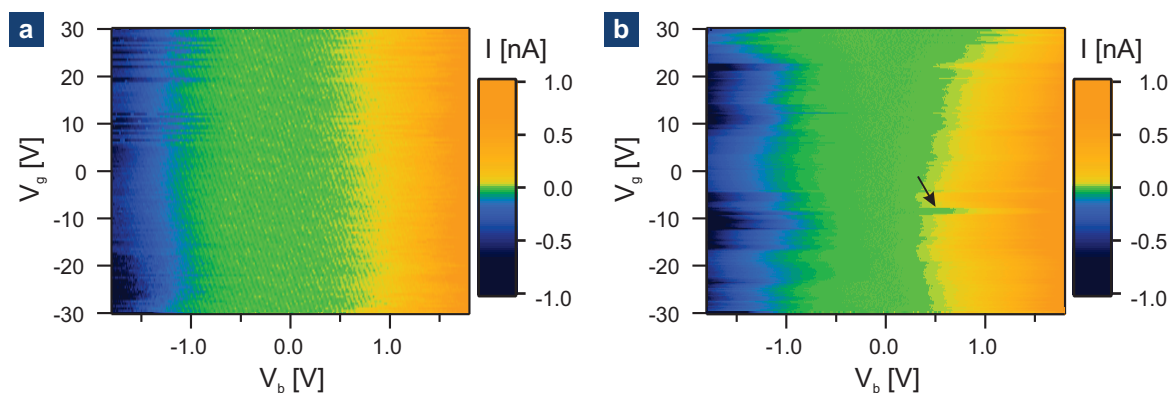


FIGURE 9.2.: Gate dependence of the $I - V$ curves of a device. **a** recorded fast (2 min recording time for the whole plot, no averaging). The pattern in the low conductance region is due to noise. **b** recorded slow (80 min recording time for the whole plot, averaged over 40 curves per gate value). No noise pattern is visible, but the onset voltage drifts with time and instabilities (as marked with the arrow) can occur. The current is plotted in a linear scale with a logarithmic color scale.

and the average curve was taken for the color-scale plot (recording time for whole plot 80 min). During this time scale drift or abrupt changes of the current onset can occur, as are observed in the color-scale plot. One of this abrupt changes is marked with an arrow in [Figure 9.2](#) right panel. For measurements performed on a short timescale (a few minutes) normally no drift or jumps are observed.

As a consequence, one has to be aware that the graphene gaps are not a completely stable system and the timescale on which measurements are performed can have a huge effect on the outcome. Performing measurements on a short timescale ensures that instabilities or drift do not affect the result. On the other hand measurements which are averaged over many confirmations may show the behavior of the statistically most relevant confirmation. In any case, the gaps should be carefully characterized prior to the measurements of molecules.

9.2. Contacting molecules

In this section we show the first measurements of molecules contacted within our graphene gaps. We use an OPE-like molecule (OPE Rod 1, $C_{130}H_{158}$, 1720 g/mol), for which the structure is shown in [Figure 9.3](#). It is composed of five conjugated subunits and two phenanthrene anchor groups. Phenanthrene anchor groups have been shown to $\pi - \pi$ stack to CNTs [[25](#), [26](#)]. Thus a good binding to graphene can

also be expected. The binding energy of similar anchor groups has been calculated and was deduced as $\approx 0.5 - 1.0$ eV [164, 165]. The length of the molecule is 3.9 nm, long enough to at least bridge some of our gaps. Recently the conductance properties of CNT-OPE Rod 1-CNT junctions have been studied, showing a resistance ranging from $G\Omega$ to $T\Omega$ [26]. The OPE Rod 1 molecules were synthesized in the group of Prof. Marcel Mayor at the University of Basel. UV-Vis spectra and electrochemical measurements of the molecule were performed by Dr. Loïc Le Pleux and are shown in [appendix G](#). They showed that the free molecule has a HOMO-LUMO gap of $E_{0-0} = 3.02$ eV.

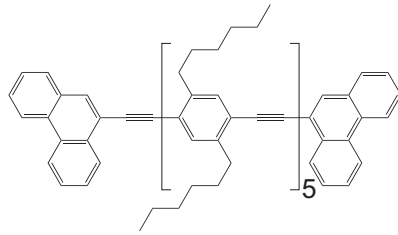


FIGURE 9.3.: Structure of the OPE-like molecule, which was deposited on the graphene nanogaps.

9.2.1. Experimental conditions

20 gaps were prepared by the EB process described in [chapter 8](#) and their $I - V$ and gate characteristics were measured. As a control, we first rinsed the gaps with dichloromethane and characterized them again. Approximately half of the samples showed an increase in resistance after rinsing with the solvent. Some contamination or carbonaceous species may have been present in the gap or on the graphene after burning. Washing them away with solvent seems to lead to an increase of the tunnel barrier or the electrodes work function. To deposit the molecules, a 0.25 mM solution of OPE Rod 1 in dichloromethane was prepared. A droplet of the solution is placed on the sample for 5 minutes followed by rinsing the sample with dichloromethane for another 5 minutes to remove unbound molecules. All the electrical measurements are performed in vacuum afterwards.

9.2.2. Current-voltage characteristics

Most of the devices do not show a significant change of the conductance after depositing the molecules. This is expected, as the conductance value observed for the molecules in CNT junctions [26] is in the same range as the conductance of the bare graphene nanogaps [150]. But for 8 out of the 20 devices we observed a change in the shape of the $I - V$ curves. These $I - V$ curves show step-like features. An example is shown in [Figure 9.4](#) top left panel (pink curve, averaged over 100 curves). In this case also an enhancement in conductance in comparison with the junction directly after

EB (dark blue curve) and rinsing with solvent (turquoise curve) is observed. Step features in $I - V$ curves were predicted [45, 51] and observed [49, 50] in molecular junctions and were attributed to resonant transport (see also section 1.3). For the gaps without molecules deposited (> 100 gaps were investigated) we never observed similar features. The numerical $\frac{dI}{dV}$ of the same $I - V$ curve is shown in Figure 9.4 top right panel. The steps in the $I - V$ curve appear as peaks in the $\frac{dI}{dV}$. They are observed at -0.51 V and 0.28 V. The asymmetry of the peaks in the $\frac{dI}{dV}$ suggests a difference in the coupling to the left and to the right electrode, which could be due to a difference in shape of the graphene electrodes. The overall shape of the curves is similar for the 8 devices mentioned above, but the position of the peaks in the $\frac{dI}{dV}$ can be quite different ranging from $\approx \pm 0.3$ V to $\approx \pm 1.5$ V. These values are in agreement with $E_{0-0} = 3.02$ eV as the maximum position for the resonance can be E_{0-0} , if it is assumed that the bias drops symmetrically over both contacts. The different positions of the resonance can be explained by a different coupling to the leads, which can shift the molecular levels. Most of the $I - V$ curves observed are strongly asymmetric, we attribute this to a difference in the coupling to the electrodes. It is possible that the EB procedure leads to an asymmetry in the electrode shape, which could favor an asymmetric coupling. The $I - V$ characteristic of additional devices and a model reproducing the shape of the curves reasonably well are provided in appendix H. Furthermore, the signal sometimes changes between normal tunneling behavior and the step-like features. This could mean that the molecule is not bound to the graphene in a stable way. Figure 9.4 lower left panel shows a fast gate scan (no averaging, 1 min recording time) of the device after rinsing with solvent. The current onset is seen at $\approx \pm 1$ V. No dependence of the $I - V$ characteristic on V_g is observed. Figure 9.4 lower right panel shows two consecutively recorded gate sweeps (no averaging, 1 min recording time) for the same device after the deposition of molecules. The current onset clearly changed to smaller values of V_g . Furthermore, more fluctuations are visible for the measurements concerning the molecules. However it is hard to judge if these fluctuations come from the gate applied or from fluctuations and further studies are needed.

Even if no clear gating of the molecular junctions could be observed, the fact that we only observed the step-like features in the $I - V$ curves after depositing molecules on the gaps, is a strong indication that indeed we were able to contact molecules with our graphene electrodes. Additional measurements are needed to reproduce the step-like features in the $I - V$ characteristics of the junctions and analyze them further. The stability issues could be addressed by performing the measurements at lower temperature or by using molecules with larger π -systems as binding groups.

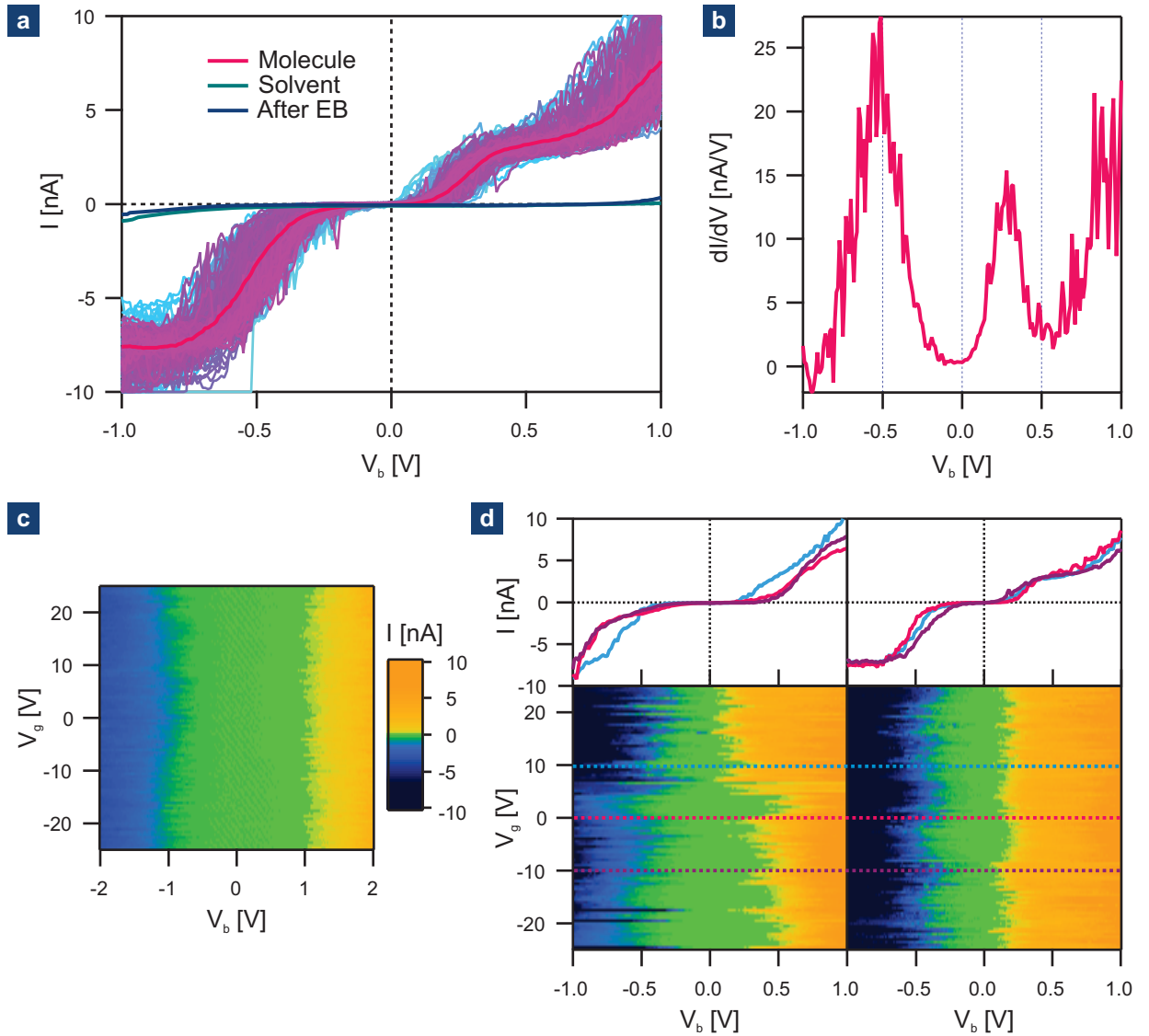


FIGURE 9.4.: **a** Averaged $I - V$ curve after EB (dark blue), rinsing with solvent (turquoise) and adding the molecules (100 single curves and their average in pink). An enhancement in conductance and step-like features are observed after adding the molecules. **b** $\frac{dI}{dV}$ of the averaged $I - V$ curve measured after adding the molecules. **c** Fast recorded gate sweep of the junction after rinsing with solvent. **d** Two fast gate sweeps recorded consecutively after adding the molecules. Averages of 5 curves at different V_g are shown on top, their position in the color-scale plot is indicated. The color scale of the current is the same as in **c**

PART III

BACKMATTER

Summary and outlook

During this PhD work we were able to implement two new strategies to contact molecules. These complementary techniques allow us to gain more insight into the charge transfer properties of molecular junctions.

First, a setup for conducting atomic force microscopy was built and used to investigate the electromechanical properties of gold-gold and gold-molecule-gold junctions [74]. Measuring electrical transport and mechanical properties of molecular junctions simultaneously is a powerful method to learn more about contact formation and breaking. We introduced two-dimensional histograms to correlate force and conductance data. Using this representation, we can clearly identify the force-conductance region where molecular junctions are formed. Furthermore our measurements allow us to determine the force needed to break the junctions apart. We also showed that the mechanism of junction formation is a dynamic process and we proposed a scenario where the molecules can migrate along the metal contacts, due to the mobility of the surface atoms.

Second a reproducible and simple process to fabricate nanometer-sized gaps in monolayer graphene was implemented [150]. This includes establishing a reliable process for the chemical vapor deposition of graphene and the subsequent transfer of the graphene onto an insulating substrate. To fabricate the gaps in the graphene, we use an electroburning process. This means that current is increased until electrical breakdown. The use of CVD graphene allows the production of large numbers of devices. Together with the very high yield we achieved for the electroburning, this is one of the major requirements for the development of graphene-based molecular electronics. Using Raman spectroscopy, we inferred the local temperature at the graphene constriction up to the electrical breakdown. The temperature dependence of the junction resistance is in agreement with a heat dissipation mechanism dominated by the coupling of the graphene to the substrate. Further we addressed the stability of the graphene gaps, a necessity for molecular measurements and in first experiments we could demonstrate the utility of our gaps for contacting molecules.

Now we have two new techniques in our hands to contact molecules. Both offer plenty of possible experiments. With the C-AFM for example it would be interesting to study different binding groups or molecules which form junctions through $\pi - \pi$

stacking [93]. One could also test the influence of molecular bridges on the stability of gold junctions [88]. To minimize the instabilities present in measurements on molecules contacted within the graphene gaps, the junctions could be stabilized by measuring at lower temperatures. Also the use of extended anchor groups was proposed to suppress conductance fluctuations [170]. The graphene gaps could allow the tuning of electron transport through a molecule via applying an electrostatic gate [27]. Fabricating a gate close to the molecule would enhance the coupling between the gate and the molecule, this could facilitate gating at room temperature. The ultimate device would allow separate gating of the electrodes and the molecule. A very interesting approach is also the combination of the two presented techniques. One could use the C-AFM (or other scanning probe techniques) to image the molecule in the junction or use it as a local gate. A molecule which bridges the graphene gap and has a third contact group could be contacted with a C-AFM as well to form a three-terminal device. Also more complex structures could be imaged.

In conclusion, we established two promising techniques which offer various possibilities to study the properties of molecular junctions in more detail.

Bibliography

- [1] A. Aviram and M. A. Ratner, *Molecular rectifiers*, *Physical Chemical Letters* **29**, 277 (1974).
- [2] G. Binnig, H. Rohrer, C. Gerber, and E. Weibel, *Surface studies by scanning tunneling microscopy*, *Physical Review Letters* **49**, 57 (1982).
- [3] C. Joachim, J. K. Gimzewski, R. R. Schlittler, and C. Chavy, *Electronic transparency of a single C₆₀ molecule*, *Physical Review Letters* **74**, 2102 (1995).
- [4] B. Q. Xu and N. J. Tao, *Measurement of single-molecule resistance by repeated formation of molecular junctions*, *Science* **301**, 1221 (2003).
- [5] C. Muller, J. van Ruitenbeek, and L. de Jongh, *Experimental observation of the transition from weak link to tunnel junction*, *Physica C* **191**, 485 (1992).
- [6] M. A. Reed, *Conductance of a molecular junction*, *Science* **278**, 252 (1997).
- [7] W. Haiss, H. van Zalinge, D. Bethell, J. Ulstrup, D. J. Schiffrin, and R. J. Nichols, *Thermal gating of the single molecule conductance of alkanedithiols*, *Faraday Discussions* **131**, 253 (2006).
- [8] C. Li, I. Pobelov, T. Wandlowski, A. Bagrets, A. Arnold, and F. Evers, *Charge transport in single au / alkanedithiol / au junctions: coordination geometries and conformational degrees of freedom*, *Journal of the American Chemical Society* **130**, 318 (2008).
- [9] X. L. Li, J. He, J. Hihath, B. Q. Xu, S. M. Lindsay, and N. J. Tao, *Conductance of single alkanedithiols: conduction mechanism and effect of molecule-electrode contacts*, *Journal of the American Chemical Society* **128**, 2135 (2006).
- [10] W. Haiss, M. S., E. Leary, H. van Zalinge, S. J. Higgins, L. Bouffier, and R. J. Nichols, *Impact of junction formation method and surface roughness on single molecule conductance*, *The Journal of Physical Chemistry C* **113**, 5823 (2009).

-
- [11] F. von Wrochem, D. Gao, F. Scholz, H.-G. Nothofer, G. Nelles, and J. M. Wessels, *Efficient electronic coupling and improved stability with dithiocarbamate-based molecular junctions*, *Nature Nanotechnology* **5**, 618 (2010).
- [12] I. Diez-Perez, J. Hihath, T. Hines, Z.-S. Wang, G. Zhou, K. Müllen, and N. Tao, *Controlling single-molecule conductance through lateral coupling of π orbitals*, *Nature Nanotechnology* **6**, 226 (2011).
- [13] M. Magoga and C. Joachim, *Conductance of molecular wires connected or bonded in parallel*, *Physical Review B* **59**, 16011 (1999).
- [14] M. T. González, J. Brunner, R. Huber, S. M. Wu, C. Schönenberger, and M. Calame, *Conductance values of alkanedithiol molecular junctions*, *New Journal of Physics* **10**, 065018 (2008).
- [15] C. R. Arroyo, E. Leary, A. Castellanos-Gómez, G. Rubio-Bollinger, M. T. González, and N. Agraït, *Influence of binding groups on molecular junction formation*, *Journal of the American Chemical Society* **133**, 14313 (2011).
- [16] J. Zhou, G. Chen, and B. Xu, *Probing the molecule-electrode interface of single-molecule junctions by controllable mechanical modulations*, *The Journal of Physical Chemistry C* **114**, 8587 (2010).
- [17] T. Konishi, M. Kiguchi, M. Takase, F. Nagasawa, H. Nabika, K. Ikeda, K. Uosaki, K. Ueno, H. Misawa, and K. Murakoshi, *Single molecule dynamics at a mechanically controllable break junction in solution at room temperature*, *Journal of the American Chemical Society* **135**, 1009 (2012).
- [18] B. Q. Xu, X. Y. Xiao, and N. J. Tao, *Measurements of single-molecule electromechanical properties*, *Journal of the American Chemical Society* **125**, 16164 (2003).
- [19] F. Chen, J. F. Zhou, G. J. Chen, and B. Q. Xu, *A novel highly integrated spm system for single molecule studies*, *IEEE Sensors Journal* **10**, 485 (2010).
- [20] M. Frei, S. V. Aradhya, M. Koentopp, M. S. Hybertsen, and L. Venkataraman, *Mechanics and chemistry: single molecule bond rupture forces correlate with molecular backbone structure*, *Nano Letters* **11**, 1518 (2011).
- [21] Y. S. Park, A. C. Whalley, M. Kamenetska, M. L. Steigerwald, M. S. Hybertsen, C. Nuckolls, and L. Venkataraman, *Contact chemistry and single-molecule conductance: a comparison of phosphines, methyl sulfides, and amines*, *Journal of the American Chemical Society* **129**, 15768 (2007).

- [22] M. Ratner, *A brief history of molecular electronics*, *Nature Nanotechnology* **8**, 378 (2013).
- [23] K. Moth-Poulsen and T. Bjørnholm, *Molecular electronics with single molecules in solid-state devices*, *Nature Nanotechnology* **4**, 551 (2009).
- [24] X. Guo, J. P. Small, J. E. Klare, Y. Wang, M. S. Purewal, I. W. Tam, B. H. Hong, R. Caldwell, L. Huang, S. O'Brien, J. Yan, R. Breslow, S. J. Wind, J. Hone, P. Kim, and C. Nuckolls, *Covalently bridging gaps in single-walled carbon nanotubes with conducting molecules*, *Science* **311**, 356 (2006).
- [25] C. W. Marquardt, S. Grunder, A. Błaszczuk, S. Dehm, F. Hennrich, H. V. Löhneysen, M. Mayor, and R. Krupke, *Electroluminescence from a single nanotube-molecule-nanotube junction*, *Nature Nanotechnology* **5**, 863 (2010).
- [26] C. Thiele, H. Vieker, A. Beyer, B. S. Flavel, F. Hennrich, D. Muñoz Torres, T. R. Eaton, M. Mayor, M. M. Kappes, A. Götzhäuser, H. V. Löhneysen, and R. Krupke, *Fabrication of carbon nanotube nanogap electrodes by helium ion sputtering for molecular contacts*, *Applied Physics Letters* **104**, 103102 (2014).
- [27] F. Prins, A. Barreiro, J. W. Ruitenbergh, J. S. Seldenthuis, N. Aliaga-Alcalde, L. M. K. Vandersypen, and H. S. J. van der Zant, *Room-temperature gating of molecular junctions using few-layer graphene nanogap electrodes*, *Nano Letters* **11**, 4607 (2011).
- [28] G. Wang, Y. Kim, M. Choe, T.-W. Kim, and T. Lee, *A new approach for molecular electronic junctions with a multilayer graphene electrode*, *Advanced Materials* **23**, 755 (2011).
- [29] Y. Wen, J. Chen, Y. Guo, B. Wu, G. Yu, and Y. Liu, *Multilayer graphene-coated atomic force microscopy tips for molecular junctions*, *Advanced Materials* **24**, 3482 (2012).
- [30] Y. Cao, S. Dong, S. Liu, L. He, L. Gan, X. Yu, M. L. Steigerwald, X. Wu, Z. Liu, and X. Guo, *Building high-throughput molecular junctions using indented graphene point contacts*, *Angewandte Chemie (International ed. in English)* **51**, 12228 (2012).
- [31] S. Seo, M. Min, S. M. Lee, and H. Lee, *Photo-switchable molecular monolayer anchored between highly transparent and flexible graphene electrodes*, *Nature Communications* **4**, 1920 (2013).
- [32] W. Fu, C. Nef, O. Knopfmacher, A. Tarasov, M. Weiss, M. Calame, and C. Schönenberger, *Graphene transistors are insensitive to pH changes in solution*, *Nano Letters* **11**, 3597 (2011).

- [33] W. Fu, C. Nef, A. Tarasov, M. Wipf, R. Stoop, O. Knopfmacher, M. Weiss, M. Calame, and C. Schönenberger, *High mobility graphene ion-sensitive field-effect transistors by noncovalent functionalization*, *Nanoscale* **5**, 12104 (2013).
- [34] X. Li, W. Cai, J. An, S. Kim, J. Nah, D. Yang, R. Piner, A. Velamakanni, I. Jung, E. Tutuc, S. K. Banerjee, L. Colombo, and R. S. Ruoff, *Large-area synthesis of high-quality and uniform graphene films on copper foils*, *Science* **324**, 1312 (2009).
- [35] Y. Lee, S. Bae, H. Jang, S. Jang, S.-E. Zhu, S. H. Sim, Y. I. Song, B. H. Hong, and J.-H. Ahn, *Wafer-scale synthesis and transfer of graphene films*, *Nano Letters* **10**, 490 (2010).
- [36] C. Mattevi, H. Kim, and M. Chhowalla, *A review of chemical vapour deposition of graphene on copper*, *Journal of Materials Chemistry* **21**, 3324 (2011).
- [37] K. V. Emtsev, A. Bostwick, K. Horn, J. Jobst, G. L. Kellogg, L. Ley, J. L. McChesney, T. Ohta, S. a. Reshanov, J. Röhrl, E. Rotenberg, A. K. Schmid, D. Waldmann, H. B. Weber, and T. Seyller, *Towards wafer-size graphene layers by atmospheric pressure graphitization of silicon carbide*, *Nature Materials* **8**, 203 (2009).
- [38] N. Agraït, A. L. Yeyati, and J. M. van Ruitenbeek, *Quantum properties of atomic-sized conductors*, *Physics Reports* **377**, 81 (2003).
- [39] R. Landauer, *Spatial variation of currents and fields due to localized scatterers*, *IBM Journal of Research and Development* **1**, 223 (1957).
- [40] E. Scheer, N. Agraït, J. Cuevas, A. Yeyati, B. Ludoph, M. Alvaro, G. Rubio-Bollinger, J. M. van Ruitenbeek, and C. Urbina, *The signature of chemical valence in the electrical conduction through a single-atom contact*, *Nature* **394**, 154 (1998).
- [41] N. Agraït, J. G. Rodrigo, and S. Vieira, *Conductance steps and quantization in atomic-size contacts*, *Physical Review B* **47**, 12345 (1993).
- [42] J. G. Simmons, *Generalized formula for the electric tunnel effect between similar electrodes separated by a thin insulating film*, *Journal of Applied Physics* **34**, 1793 (1963).
- [43] J. Beebe, B. Kim, J. Gadzuk, C. Daniel Frisbie, and J. Kushmerick, *Transition from direct tunneling to field emission in metal-molecule-metal junctions*, *Physical Review Letters* **97**, 026801 (2006).

- [44] J.-P. L. M. Verdaguer, *Electrons in molecules from basic principles to molecular electronics*, 1st ed. (Oxford University Press, 2014).
- [45] A. Troisi and M. A. Ratner, *Molecular signatures in the transport properties of molecular wire junctions: what makes a junction "molecular"?*, *Small* **2**, 172 (2006).
- [46] Q. Sun, A. Selloni, and G. Scoles, *Electron tunneling through molecular media: a density functional study of Au/Dithiol/Au systems*, *ChemPhysChem* **6**, 1906 (2005).
- [47] H. Song, M. A. Reed, and T. Lee, *Single molecule electronic devices*, *Advanced Materials* **23**, 1583 (2011).
- [48] R. Smit, Y. Noat, and C. Untiedt, *Measurement of the conductance of a hydrogen molecule*, *Nature* **419**, 906 (2002).
- [49] C. Kergueris, J.-P. Bourgoin, S. Palacin, D. Esteve, C. Urbina, M. Magoga, and C. Joachim, *Electron transport through a metal-molecule-metal junction*, *Physical Review B* **59**, 12505 (1999).
- [50] J. Reichert, R. Ochs, D. Beckmann, H. Weber, M. Mayor, and H. Löhneysen, *Driving Current through Single Organic Molecules*, *Physical Review Letters* **88**, 176804 (2002).
- [51] M. Galperin, M. A. Ratner, and A. Nitzan, *Hysteresis, switching, and negative differential resistance in molecular junctions: a polaron model*, *Nano Letters* **5**, 125 (2005).
- [52] A. S. Blum, J. G. Kushmerick, D. P. Long, C. H. Patterson, J. C. Yang, J. C. Henderson, Y. Yao, J. M. Tour, R. Shashidhar, and B. R. Ratna, *Molecularly inherent voltage-controlled conductance switching*, *Nature Materials* **4**, 167 (2005).
- [53] I. Franco, C. B. George, G. C. Solomon, G. C. Schatz, and M. A. Ratner, *Mechanically activated molecular switch through single-molecule pulling*, *Journal of the American Chemical Society* **133**, 2242 (2011).
- [54] M. Tsutsui, M. Taniguchi, and T. Kawai, *Quantitative evaluation of metal-molecule contact stability at the single-molecule level*, *Journal of the American Chemical Society* **131**, 10552 (2009).
- [55] W. Hong, D. Z. Manrique, P. Moreno-García, M. Gulcur, A. Mishchenko, C. J. Lambert, M. R. Bryce, and T. Wandlowski, *Single molecular*

- conductance of tolanes: experimental and theoretical study on the junction evolution dependent on the anchoring group*, *Journal of the American Chemical Society* **134**, 2292 (2012).
- [56] Z.-L. Cheng, R. Skouta, H. Vazquez, J. R. Widawsky, S. Schneebeli, W. Chen, M. S. Hybertsen, R. Breslow, and L. Venkataraman, *In situ formation of highly conducting covalent Au-C contacts for single-molecule junctions*, *Nature Nanotechnology* **6**, 353 (2011).
- [57] W. Chen, J. R. Widawsky, H. Vázquez, S. T. Schneebeli, M. S. Hybertsen, R. Breslow, and L. Venkataraman, *Highly conducting π -conjugated molecular junctions covalently bonded to gold electrodes.*, *Journal of the American Chemical Society* **133**, 17160 (2011).
- [58] O. Tal, M. Kiguchi, W. H. A. Thijssen, D. Djukic, C. Untiedt, R. H. M. Smit, and J. M. V. Ruitenbeek, *Molecular signature of highly conductive metal-molecule-metal junctions*, *Reviews of Modern Physics* **80**, 1 (2009).
- [59] P. Makk, Z. Balogh, S. Csonka, and A. Halbritter, *Pulling platinum atomic chains by carbon monoxide molecules*, *Nanoscale* **4**, 4739 (2012).
- [60] S. V. Aradhya, M. Frei, A. Halbritter, and L. Venkataraman, *Correlating structure, conductance, and mechanics of silver atomic-scale contacts*, *ACS Nano* **7**, 3706 (2013).
- [61] D. J. Wold, R. Haag, M. A. Rampi, and C. D. Frisbie, *Distance dependence of electron tunneling through self-assembled monolayers measured by conducting probe atomic force microscopy: Unsaturated versus saturated molecular junctions*, *The Journal of Physical Chemistry B* **106**, 10 (2002).
- [62] R. Huber, M. T. González, S. Wu, M. Langer, S. Grunder, V. Horhoiu, M. Mayor, M. R. Bryce, C. Wang, R. Jitchati, C. Schönenberger, and M. Calame, *Electrical conductance of conjugated oligomers at the single molecule level*, *Journal of the American Chemical Society* **130**, 1080 (2008).
- [63] V. Kaliginedi, P. Moreno-García, H. Valkenier, W. Hong, V. M. García-Suárez, P. Buitter, J. L. H. Otten, J. C. Hummelen, C. J. Lambert, and T. Wandlowski, *Correlations between molecular structure and single-junction conductance: a case study with oligo(phenylene-ethynylene)-type wires*, *Journal of the American Chemical Society* **134**, 5262 (2012).
- [64] L. Venkataraman, J. E. Klare, C. Nuckolls, M. S. Hybertsen, and M. L. Steigerwald, *Dependence of single-molecule junction conductance on molecular conformation*, *Nature* **442**, 904 (2006).

- [65] S. V. Aradhya, J. S. Meisner, M. Krikorian, S. Ahn, R. Parameswaran, M. L. Steigerwald, C. Nuckolls, and L. Venkataraman, *Dissecting contact mechanics from quantum interference in single-molecule junctions of stilbene derivatives*, *Nano Letters* **12**, 1643 (2012).
- [66] C. M. Guédon, H. Valkenier, T. Markussen, K. S. Thygesen, J. C. Hummelen, and S. J. van der Molen, *Observation of quantum interference in molecular charge transport*, *Nature Nanotechnology* **7**, 305 (2012).
- [67] C. R. Arroyo, S. Tarkuc, R. Frisenda, J. S. Seldenthuis, C. H. M. Woerde, R. Eelkema, F. C. Grozema, and H. S. J. van der Zant, *Signatures of quantum interference effects on charge transport through a single benzene ring*, *Angewandte Chemie (International ed. in English)* **52**, 3152 (2013).
- [68] E. A. Osorio, T. Bjornholm, J. M. Lehn, M. Ruben, and H. S. J. van der Zant, *Single-molecule transport in three-terminal devices*, *Journal of Physics-Condensed Matter* **20**, 013001 (2008).
- [69] I. Diez-Perez, Z. Li, S. Guo, C. Madden, H. Huang, and Y. Che, *Ambipolar transport in an electrochemically gated single-molecule*, *ACS Nano* **6**, 7044 (2012).
- [70] S. J. van der Molen, J. Liao, T. Kudernac, J. S. Agustsson, L. Bernard, M. Calame, B. J. V. Wees, B. L. Feringa, and C. Scho, *Light-controlled conductance switching of ordered metal - molecule - metal devices*, *Nano Letters* **9**, 76 (2009).
- [71] G. Binnig, C. Quate, and C. Gerber, *Atomic force microscope*, *Physical Review Letters* **56**, 930 (1986).
- [72] G. Rubio, N. Agrait, and S. Vieira, *Atomic-sized metallic contacts: Mechanical properties and electronic transport*, *Physical Review Letters* **76**, 2302 (1996).
- [73] T. Todorov and A. Sutton, *Jumps in electronic conductance due to mechanical instabilities*, *Physical Review Letters* **70**, 2138 (1993).
- [74] C. Nef, P. L. T. M. Frederix, J. Brunner, C. Schönenberger, and M. Calame, *Force-conductance correlation in individual molecular junctions*, *Nanotechnology* **23**, 365201 (2012).
- [75] X. D. Cui, A. Primak, X. Zarate, J. Tomfohr, O. F. Sankey, A. L. Moore, T. A. Moore, D. Gust, G. Harris, and S. M. Lindsay, *Reproducible measurement of single-molecule conductivity*, *Science* **294**, 571 (2001).

- [76] Z. Huang, F. Chen, P. A. Bennett, and N. J. Tao, *Single molecule junctions formed via au-thiol contact: stability and breakdown mechanism*, *Journal of the American Chemical Society* **129**, 13225 (2007).
- [77] H. J. Butt and M. Jaschke, *Calculation of thermal noise in atomic force microscopy*, *Nanotechnology* **6**, 1 (1995).
- [78] J. C. Love, L. A. Estroff, J. K. Kriebel, R. G. Nuzzo, and G. M. Whitesides, *Self-assembled monolayers of thiolates on metals as a form of nanotechnology*, *Chemical Reviews* **105**, 1103 (2005).
- [79] P. D. Bosshart, F. Casagrande, P. L. T. M. Frederix, M. Ratera, C. A. Bippes, D. J. Müller, M. Palacin, A. Engel, and D. Fotiadis, *High-throughput single-molecule force spectroscopy for membrane proteins*, *Nanotechnology* **19**, 384014 (2008).
- [80] A. Stalder, U. Du, and I. Introduction, *Study of plastic flow in ultrasmall Au contacts*, *Journal of Vacuum Science and Technology B* **14**, 1259 (1996).
- [81] H. Ohnishi, Y. Kondo, and K. Takayanagi, *Quantized conductance through individual rows of suspended gold atoms*, *Nature* **395**, 2 (1998).
- [82] W. Haiss, R. J. Nichols, H. van Zalinge, S. J. Higgins, D. Bethell, and D. J. Schiffrin, *Measurement of single molecule conductivity using the spontaneous formation of molecular wires*, *Physical Chemistry Chemical Physics* **6**, 4330 (2004).
- [83] H. B. Akkerman and B. de Boer, *Electrical conduction through single molecules and self-assembled monolayers*, *Journal of Physics: Condensed Matter* **20**, 013001 (2008).
- [84] M. T. González, S. Wu, R. Huber, S. van der Molen, C. Schönenberger, and M. Calame, *Electrical conductance of molecular junctions by a robust statistical analysis*, *Nano Letters* **6**, 2238 (2006).
- [85] G. Rubio-Bollinger, S. R. Bahn, N. Agraït, K. W. Jacobsen, and S. Vieira, *Mechanical properties and formation mechanisms of a wire of single gold atoms*, *Physical Review Letters* **87**, 026101 (2001).
- [86] M. Okamoto and K. Takayanagi, *Structure and conductance of a gold atomic chain*, *Physical Review B* **60**, 7808 (1999).
- [87] M. R. Sørensen, M. Brandbyge, and K. W. Jacobsen, *Mechanical deformation of atomic-scale metallic contacts: structure and mechanisms*, *Physical Review B* **57**, 3283 (1998).

- [88] E. H. Huisman, M. L. Trouwborst, F. L. Bakker, B. de Boer, B. J. van Wees, and S. J. van der Molen, *Stabilizing single atom contacts by molecular bridge formation*, *Nano Letters* **8**, 3381 (2008).
- [89] W. R. French, C. R. Iacovella, and P. T. Cummings, *The influence of molecular adsorption on elongating gold nanowires*, *The Journal of Physical Chemistry C* **115**, 18422 (2011).
- [90] M. Brandbyge, J. Schiøtz, M. R. Sørensen, P. Stoltze, K. W. Jacobsen, J. K. Nørskov, L. Olesen, E. Laegsgaard, I. Stensgaard, and F. Besenbacher, *Quantized conductance in atom-sized wires between two metals*, *Physical Review B* **52**, 8499 (1995).
- [91] D. Krüger, H. Fuchs, R. Rousseau, D. Marx, and M. Parrinello, *Pulling monatomic gold wires with single molecules: an ab initio simulation*, *Physical Review Letters* **89**, 186402 (2002).
- [92] E. Huisman, *Electron transport through single organic molecules and self-assembled monolayers*, *Ph.D. thesis*, Rijksuniversiteit Groningen (2010).
- [93] S. Wu, R. Huber, M. T. González, S. Grunder, M. Mayor, C. Schönenberger, and M. Calame, *Molecular junctions based on aromatic coupling*, *Nature Nanotechnology* **3**, 569 (2008).
- [94] S. Martin, I. Grace, M. R. Bryce, C. Wang, R. Jitchati, A. S. Batsanov, S. J. Higgins, C. J. Lambert, and R. J. Nichols, *Identifying diversity in nanoscale electrical break junctions*, *Journal of the American Chemical Society* **132**, 9157 (2010).
- [95] M. T. González, E. Leary, R. García, P. Verma, M. Á. Herranz, G. Rubio-Bollinger, N. Martín, and N. Agraït, *Break-junction experiments on acetyl-protected conjugated dithiols under different environmental conditions*, *The Journal of Physical Chemistry C* **115**, 17973 (2011).
- [96] K. S. Novoselov, A. K. Geim, S. V. Morozov, D. Jiang, Y. Zhang, S. V. Dubonos, I. V. Grigorieva, and A. A. Firsov, *Electric field effect in atomically thin carbon films*, *Science* **306**, 666 (2004).
- [97] C. Lee, X. Wei, J. W. Kysar, and J. Hone, *Measurement of the elastic properties and intrinsic strength of monolayer graphene*, *Science* **321**, 385 (2008).
- [98] S. Das Sarma, S. Adam, E. Hwang, and E. Rossi, *Electronic transport in two-dimensional graphene*, *Reviews of Modern Physics* **83**, 407 (2011).

-
- [99] G. J. A. Dresselhaus, Mildred S. Dresselhaus, *Group theory, application to the physics of condensed matter* (Springer-Verlag Berlin Heidelberg, 2008).
- [100] P. Wallace, *The band theory of graphite*, *Physical Review* **71**, 622 (1947).
- [101] A. H. Castro Neto, N. M. R. Peres, K. S. Novoselov, and A. K. Geim, *The electronic properties of graphene*, *Reviews of Modern Physics* **81**, 109 (2009).
- [102] N. O. Weiss, H. Zhou, L. Liao, Y. Liu, S. Jiang, Y. Huang, and X. Duan, *Graphene: an emerging electronic material*, *Advanced Materials* **24**, 5782 (2012).
- [103] K. S. Novoselov, Z. Jiang, Y. Zhang, S. V. Morozov, H. L. Stormer, U. Zeitler, J. C. Maan, G. S. Boebinger, P. Kim, and A. K. Geim, *Room-temperature quantum hall*, *Science* **315**, 2007 (2007).
- [104] N. Tombros, A. Veligura, J. Junesch, M. H. D. Guimarães, I. J. Vera-Marun, H. T. Jonkman, and B. J. van Wees, *Quantized conductance of a suspended graphene nanoconstriction*, *Nature Physics* **7**, 697 (2011).
- [105] P. Rickhaus, R. Maurand, M.-H. Liu, M. Weiss, K. Richter, and C. Schönberger, *Ballistic interferences in suspended graphene*, *Nature Communications* **4**, 2342 (2013).
- [106] A. L. Grushina, D.-K. Ki, and A. F. Morpurgo, *A ballistic pn junction in suspended graphene with split bottom gates*, *Applied Physics Letters* **102**, 223102 (2013).
- [107] M. I. Katsnelson, K. S. Novoselov, and A. K. Geim, *Chiral tunnelling and the Klein paradox in graphene*, *Nature Physics* **2**, 620 (2006).
- [108] J.-A. Yan, W. Ruan, and M. Chou, *Phonon dispersions and vibrational properties of monolayer, bilayer, and trilayer graphene: Density-functional perturbation theory*, *Physical Review B* **77**, 125401 (2008).
- [109] A. C. Ferrari and D. M. Basko, *Raman spectroscopy as a versatile tool for studying the properties of graphene*, *Nature Nanotechnology* **8**, 235 (2013).
- [110] L. Malard, M. Pimenta, G. Dresselhaus, and M. Dresselhaus, *Raman spectroscopy in graphene*, *Physics Reports* **473**, 51 (2009).
- [111] M.-H. Bae, Z. Li, Z. Aksamija, P. N. Martin, F. Xiong, Z.-Y. Ong, I. Knezevic, and E. Pop, *Ballistic to diffusive crossover of heat flow in graphene ribbons.*, *Nature Communications* **4**, 1734 (2013).

- [112] A. A. Balandin, *Thermal properties of graphene and nanostructured carbon materials*, *Nature Materials* **10**, 569 (2011).
- [113] A. A. Balandin, S. Ghosh, W. Bao, I. Calizo, D. Teweldebrhan, F. Miao, and C. N. Lau, *Superior thermal conductivity of single-layer graphene*, *Nano Letters* **8**, 902 (2008).
- [114] S. Ghosh, W. Bao, D. L. Nika, S. Subrina, E. P. Pokatilov, C. N. Lau, and A. a. Balandin, *Dimensional crossover of thermal transport in few-layer graphene*, *Nature Materials* **9**, 555 (2010).
- [115] J. H. Seol, I. Jo, A. L. Moore, L. Lindsay, Z. H. Aitken, M. T. Pettes, X. Li, Z. Yao, R. Huang, D. Broido, N. Mingo, R. S. Ruoff, and L. Shi, *Two-dimensional phonon transport in supported graphene*, *Science* **328**, 213 (2010).
- [116] M. Freitag, M. Steiner, Y. Martin, V. Perebeinos, Z. Chen, J. C. Tsang, and P. Avouris, *Energy dissipation in graphene field-effect transistors*, *Nano Letters* **9**, 1883 (2009).
- [117] M.-H. Bae, Z.-Y. Ong, D. Estrada, and E. Pop, *Imaging, simulation, and electrostatic control of power dissipation in graphene devices.*, *Nano Letters* **10**, 4787 (2010).
- [118] J.-H. Chen, C. Jang, S. Xiao, M. Ishigami, and M. S. Fuhrer, *Intrinsic and extrinsic performance limits of graphene devices on SiO₂*, *Nature Nanotechnology* **3**, 206 (2008).
- [119] S. Fratini and F. Guinea, *Substrate-limited electron dynamics in graphene*, *Physical Review B* **77**, 195415 (2008).
- [120] A. S. Price, S. M. Hornett, A. V. Shytov, E. Hendry, and D. W. Horsell, *Nonlinear resistivity and heat dissipation in monolayer graphene*, *Physical Review B* **85**, 161411 (2012).
- [121] D. K. Efetov and P. Kim, *Controlling electron-phonon interactions in graphene at ultrahigh carrier densities*, *Physical Review Letters* **105**, 256805 (2010).
- [122] Y. Hernandez, V. Nicolosi, M. Lotya, F. M. Blighe, Z. Sun, S. De, I. T. McGovern, B. Holland, M. Byrne, Y. K. Gun'Ko, J. J. Boland, P. Niraj, G. Duesberg, S. Krishnamurthy, R. Goodhue, J. Hutchison, V. Scardaci, A. C. Ferrari, and J. N. Coleman, *High-yield production of graphene by liquid-phase exfoliation of graphite*, *Nature Nanotechnology* **3**, 563 (2008).

- [123] J. Chan, A. Venugopal, A. Pirkle, S. McDonnell, D. Hinojos, C. W. Magnuson, R. S. Ruoff, L. Colombo, R. M. Wallace, and E. M. Vogel, *Reducing extrinsic performance-limiting factors in graphene grown by chemical vapor deposition.*, *ACS Nano* **6**, 3224 (2012).
- [124] C.-M. Seah, S.-P. Chai, and A. R. Mohamed, *Mechanisms of graphene growth by chemical vapour deposition on transition metals*, *Carbon* **70**, 1 (2014).
- [125] X. Li, Y. Zhu, W. Cai, M. Borysiak, B. Han, D. Chen, R. D. Piner, L. Colombo, and R. S. Ruoff, *Transfer of large-area graphene films for high-performance transparent conductive electrodes*, *Nano Letters* **9**, 4359 (2009).
- [126] X. Li, C. W. Magnuson, A. Venugopal, J. An, J. W. Suk, B. Han, M. Borysiak, W. Cai, A. Velamakanni, Y. Zhu, L. Fu, E. M. Vogel, E. Voelkl, L. Colombo, and R. S. Ruoff, *Graphene films with large domain size by a two-step chemical vapor deposition process*, *Nano Letters* **10**, 4328 (2010).
- [127] Z. Yan, J. Lin, Z. Peng, Z. Sun, Y. Zhu, L. Li, C. Xiang, E. L. Samuel, C. Kittrell, and J. M. Tour, *Toward the synthesis of wafer-scale single-crystal graphene on copper foils*, *ACS Nano* **6**, 9110 (2012).
- [128] L. Gao, W. Ren, H. Xu, L. Jin, Z. Wang, T. Ma, L.-P. Ma, Z. Zhang, Q. Fu, L.-M. Peng, X. Bao, and H.-M. Cheng, *Repeated growth and bubbling transfer of graphene with millimetre-size single-crystal grains using platinum*, *Nature Communications* **3**, 699 (2012).
- [129] S. Bhaviripudi, X. Jia, M. S. Dresselhaus, and J. Kong, *Role of kinetic factors in chemical vapor deposition synthesis of uniform large area graphene using copper catalyst*, *Nano Letters* **10**, 4128 (2010).
- [130] K. S. Kim, Y. Zhao, H. Jang, S. Y. Lee, J. M. Kim, K. S. Kim, J.-H. Ahn, P. Kim, J.-Y. Choi, and B. H. Hong, *Large-scale pattern growth of graphene films for stretchable transparent electrodes*, *Nature* **457**, 706 (2009).
- [131] S. Bae, H. Kim, Y. Lee, X. Xu, J.-S. Park, Y. Zheng, J. Balakrishnan, T. Lei, H. R. Kim, Y. I. Song, Y.-J. Kim, K. S. Kim, B. Ozyilmaz, J.-H. Ahn, B. H. Hong, and S. Iijima, *Roll-to-roll production of 30-inch graphene films for transparent electrodes.*, *Nature Nanotechnology* **5**, 574 (2010).
- [132] J. W. Suk, A. Kitt, C. W. Magnuson, Y. Hao, S. Ahmed, J. An, A. K. Swan, B. B. Goldberg, and R. S. Ruoff, *Transfer of CVD-grown monolayer graphene onto arbitrary substrates*, *ACS Nano* **5**, 6916 (2011).

- [133] X. Liang, B. a. Sperling, I. Calizo, G. Cheng, C. A. Hacker, Q. Zhang, Y. Obeng, K. Yan, H. Peng, Q. Li, X. Zhu, H. Yuan, A. R. H. Walker, Z. Liu, L.-M. Peng, and C. A. Richter, *Toward clean and crackless transfer of graphene*, *ACS Nano* **5**, 9144 (2011).
- [134] Y. Wang, Y. Zheng, X. Xu, E. Dubuisson, Q. Bao, J. Lu, and K. P. Loh, *Electrochemical delamination of CVD-grown graphene film: toward the recyclable use of copper catalyst*, *ACS Nano* **5**, 9927 (2011).
- [135] W. Lin, T. Chen, J. Chang, J. Taur, and Y. Lo, *A direct and polymer-free method for transferring graphene grown by chemical vapor deposition to any substrate*, *ACS Nano* **8**, 1784 (2014).
- [136] M. Jang, T. Q. Trung, J.-H. Jung, B.-Y. Kim, and N.-E. Lee, *Improved performance and stability of field-effect transistors with polymeric residue-free graphene channel transferred by gold layer*, *Physical Chemistry Chemical Physics* **16**, 4098 (2014).
- [137] M. Ishigami, J. H. Chen, W. G. Cullen, M. S. Fuhrer, and E. D. Williams, *Atomic structure of graphene on SiO₂*, *Nano Letters* **7**, 1643 (2007).
- [138] Y.-D. Lim, D.-Y. Lee, T.-Z. Shen, C.-H. Ra, J.-Y. Choi, and W. J. Yoo, *Si-compatible cleaning process for graphene using low-density inductively coupled plasma.*, *ACS nano* **6**, 4410 (2012).
- [139] P. Blake, E. W. Hill, A. H. Castro Neto, K. S. Novoselov, D. Jiang, R. Yang, T. J. Booth, and A. K. Geim, *Making graphene visible*, *Applied Physics Letters* **91**, 063124 (2007).
- [140] Z. H. Ni, H. M. Wang, J. Kasim, H. M. Fan, T. Yu, Y. H. Wu, Y. P. Feng, and Z. X. Shen, *Graphene thickness determination using reflection and contrast spectroscopy*, *Nano Letters* **7**, 2758 (2007).
- [141] R. R. Nair, P. Blake, A. N. Grigorenko, K. S. Novoselov, T. J. Booth, T. Stauber, N. M. R. Peres, and A. K. Geim, *Fine structure constant defines visual transparency of graphene*, *Science* **320**, 1308 (2008).
- [142] F. Schedin, A. K. Geim, S. V. Morozov, E. W. Hill, P. Blake, M. I. Katsnelson, and K. S. Novoselov, *Detection of individual gas molecules adsorbed on graphene*, *Nature Materials* **6**, 652 (2007).
- [143] J. Moser, A. Barreiro, and A. Bachtold, *Current-induced cleaning of graphene*, *Applied Physics Letters* **91**, 163513 (2007).
- [144] A. K. Geim and K. S. Novoselov, *The rise of graphene*, *Nature Materials* **6**, 183 (2007).

- [145] M. Dresselhaus, A. Jorio, and R. Saito, *Characterizing graphene, graphite, and carbon nanotubes by raman spectroscopy*, *Annual Review of Condensed Matter Physics* **1**, 89 (2010).
- [146] S.-L. Zhang, *Raman spectroscopy and its application in nanostructures* (John Wiley & Sons, Ltd., 2012).
- [147] I. Calizo, F. Miao, W. Bao, C. N. Lau, and A. a. Balandin, *Variable temperature Raman microscopy as a nanometrology tool for graphene layers and graphene-based devices*, *Applied Physics Letters* **91**, 071913 (2007).
- [148] D. Abdula, T. Ozel, K. Kang, D. G. Cahill, and M. Shim, *Environment-induced effects on the temperature dependence of raman spectra of single-layer graphene*, *The Journal of Physical Chemistry C* **112**, 20131 (2008).
- [149] D.-H. Chae, B. Krauss, K. von Klitzing, and J. H. Smet, *Hot phonons in an electrically biased graphene constriction*, *Nano Letters* **10**, 466 (2010).
- [150] C. Nef, L. Pósa, P. Makk, W. Fu, A. Halbritter, C. Schönenberger, and M. Calame, *High-yield fabrication of nm-size gaps in monolayer CVD graphene.*, *Nanoscale* **6**, 7249 (2014).
- [151] R. A. Cowley, *Raman scattering from crystals of the diamond structure*, *Journal de Physique* **26**, 659 (1965).
- [152] M. Balkanski, R. F. Wallis, and E. Haro, *Anharmonic effect in light scattering due to optical phonons in silicon*, *Physical Review B* **28**, 1928 (1983).
- [153] A. K. Geim, *Graphene: status and prospects*, *Science* **324**, 1530 (2009).
- [154] K. S. Novoselov, V. I. Fal'ko, L. Colombo, P. R. Gellert, M. G. Schwab, and K. Kim, *A roadmap for graphene*, *Nature* **490**, 192 (2012).
- [155] P. K. Ang, W. Chen, A. T. S. Wee, and K. P. Loh, *Solution-gated epitaxial graphene as pH sensor*, *Journal of the American Chemical Society* **130**, 14392 (2008).
- [156] Y. Ohno, K. Maehashi, Y. Yamashiro, and K. Matsumoto, *Electrolyte-gated graphene field-effect transistors for detecting pH and protein adsorption*, *Nano Letters* **9**, 3318 (2009).
- [157] M. Dankerl, M. V. Hauf, A. Lippert, L. H. Hess, S. Birner, I. D. Sharp, A. Mahmood, P. Mallet, J.-Y. Veullen, M. Stutzmann, and J. A. Garrido, *Graphene solution-gated field-effect transistor array for sensing applications*, *Advanced Functional Materials* **20**, 3117 (2010).

- [158] Y. Liu, X. Dong, and P. Chen, *Biological and chemical sensors based on graphene materials*, *Chemical Society Reviews* **41**, 2283 (2012).
- [159] O. Knopfmacher, A. Tarasov, W. Fu, M. Wipf, B. Niesen, M. Calame, and C. Schönenberger, *Nernst limit in dual-gated Si-nanowire FET sensors*, *Nano Letters* **10**, 2268 (2010).
- [160] L. Bousse, N. F. De Rooij, and P. Bergveld, *Operation of chemically sensitive field-effect sensors as a function of the insulator-electrolyte interface*, *IEEE Transactions on Electron Devices* **30**, 1263 (1983).
- [161] Z. Cheng, Q. Li, Z. Li, Q. Zhou, and Y. Fang, *Suspended graphene sensors with improved signal and reduced noise*, *Nano Letters* **10**, 1864 (2010).
- [162] I. Heller, S. Chatoor, J. Männik, M. A. G. Zevenbergen, C. Dekker, and S. G. Lemay, *Influence of electrolyte composition on liquid-gated carbon nanotube and graphene transistors*, *Journal of the American Chemical Society* **132**, 17149 (2010).
- [163] W. M. Siu and R. S. C. Cobbold, *Basic properties of the electrolyte-SiO₂-Si system : physical and theoretical aspects*, *IEEE Transactions on Electron Devices* **26**, 1805 (1979).
- [164] S. Chakarova-Käck, E. Schröder, B. Lundqvist, and D. Langreth, *Application of van der Waals density functional to an extended system: adsorption of benzene and naphthalene on graphite*, *Physical Review Letters* **96**, 146107 (2006).
- [165] S. Bailey, D. Visontai, C. J. Lambert, M. R. Bryce, H. Frampton, and D. Chappell, *A study of planar anchor groups for graphene-based single-molecule electronics*, *The Journal of Chemical Physics* **140**, 054708 (2014).
- [166] D. B. Farmer and R. G. Gordon, *Atomic layer deposition on suspended single-walled carbon nanotubes via gas-phase noncovalent functionalization*, *Nano Letters* **6**, 699 (2006).
- [167] E. Lörtscher, *Wiring molecules into circuits*, *Nature Nanotechnology* **8**, 381 (2013).
- [168] D. Carrascal, V. García-Suárez, and J. Ferrer, *Impact of edge shape on the functionalities of graphene-based single-molecule electronics devices*, *Physical Review B* **85**, 195434 (2012).
- [169] D. Ryndyk, J. Bundesmann, M.-H. Liu, and K. Richter, *Edge state effects in junctions with graphene electrodes*, *Physical Review B* **86**, 195425 (2012).

- [170] C. G. Péterfalvi and C. J. Lambert, *Suppression of single-molecule conductance fluctuations using extended anchor groups on graphene and carbon-nanotube electrodes*, *Physical Review B* **86**, 085443 (2012).
- [171] E. Burzurí, F. Prins, and H. S. J. van der Zant, *Characterization of nanometer-spaced few-layer graphene electrodes*, *Graphene* **01**, 26 (2012).
- [172] D. C. Bell, M. C. Lemme, L. A. Stern, J. R. Williams, and C. M. Marcus, *Precision cutting and patterning of graphene with helium ions*, *Nanotechnology* **20**, 455301 (2009).
- [173] A. Abbas, G. Liu, B. Liu, L. Zhang, and H. Liu, *Patterning, characterization, and chemical sensing applications of graphene nanoribbon arrays down to 5 nm using helium ion beam lithography*, *ACS Nano* **8**, 1538 (2014).
- [174] N. Kalhor, S. A. Boden, and H. Mizuta, *Sub-10nm patterning by focused He-ion beam milling for fabrication of downscaled graphene nano devices*, *Microelectronic Engineering* **114**, 70 (2014).
- [175] H. Park, A. K. L. Lim, A. P. Alivisatos, J. Park, and P. L. McEuen, *Fabrication of metallic electrodes with nanometer separation by electromigration*, *Applied Physics Letters* **75**, 301 (1999).
- [176] H. Park, J. Park, A. K. L. Lim, E. H. Anderson, A. P. Alivisatos, and P. L. McEuen, *Nanomechanical oscillations in a single-C60 transistor*, *Nature* **407**, 57 (2000).
- [177] Z. M. Wu, M. Steinacher, R. Huber, M. Calame, S. J. van der Molen, and C. Schönberger, *Feedback controlled electromigration in four-terminal nanojunctions*, *Applied Physics Letters* **91**, 053118 (2007).
- [178] P. Collins, M. Hersam, M. Arnold, R. Martel, and P. Avouris, *Current saturation and electrical breakdown in multiwalled carbon nanotubes*, *Physical Review Letters* **86**, 3128 (2001).
- [179] Z. Yao, C. Kane, and C. Dekker, *High-field electrical transport in single-wall carbon nanotubes*, *Physical Review Letters* **84**, 2941 (2000).
- [180] I. Meric, M. Y. Han, A. F. Young, B. Ozyilmaz, P. Kim, and K. L. Shepard, *Current saturation in zero-bandgap, top-gated graphene field-effect transistors*, *Nature Nanotechnology* **3**, 654 (2008).
- [181] A. Barreiro, M. Lazzeri, J. Moser, F. Mauri, and A. Bachtold, *Transport properties of graphene in the high-current limit*, *Physical Review Letters* **103**, 2 (2009).

- [182] A. Barreiro, F. Börrnert, M. H. Rümmeli, B. Büchner, and L. M. K. Vandersypen, *Graphene at high bias: cracking, layer by layer sublimation, and fusing*, *Nano Letters* **12**, 1873 (2012).
- [183] F. Börrnert, A. Barreiro, D. Wolf, M. I. Katsnelson, B. Büchner, L. M. K. Vandersypen, and M. H. Rümmeli, *Lattice expansion in seamless bilayer graphene constrictions at high bias*, *NanoLetters* **12**, 4455 (2012).
- [184] R. Murali, Y. Yang, K. Brenner, T. Beck, and J. D. Meindl, *Breakdown current density of graphene nanoribbons*, *Applied Physics Letters* **94**, 243114 (2009).
- [185] J. Moser and A. Bachtold, *Fabrication of large addition energy quantum dots in graphene*, *Applied Physics Letters* **95**, 173506 (2009).
- [186] A. Barreiro, R. Ruruli, E. R. Hernández, and A. Bachtold, *Structured graphene devices for mass transport*, *Small* **7**, 775 (2011).
- [187] K. S. Novoselov, D. Jiang, F. Schedin, T. J. Booth, V. V. Khotkevich, S. V. Morozov, and A. K. Geim, *Two-dimensional atomic crystals*, *Proceedings of the National Academy of Sciences* **102**, 10451 (2005).
- [188] A. Mangin, A. Anthore, M. L. Della Rocca, E. Boulat, and P. Lafarge, *Reduced work functions in gold electromigrated nanogaps*, *Physical Review B* **80**, 235432 (2009).
- [189] L. Liu, S. Ryu, M. R. Tomasik, E. Stolyarova, N. Jung, M. S. Hybertsen, M. L. Steigerwald, L. E. Brus, and G. W. Flynn, *Graphene oxidation: thickness-dependent etching and strong chemical doping*, *Nano Letters* **8**, 1965 (2008).
- [190] V. E. Dorgan, A. Behnam, H. J. Conley, K. I. Bolotin, and E. Pop, *High-field electrical and thermal transport in suspended graphene*, *Nano Letters* **13**, 4581 (2013).
- [191] L. Grüter, M. T. González, R. Huber, M. Calame, and C. Schönberger, *Electrical conductance of atomic contacts in liquid environments*, *Small* **1**, 1067 (2005).
- [192] J. Xia, F. Chen, J. Li, and N. Tao, *Measurement of the quantum capacitance of graphene*, *Nature Nanotechnology* **4**, 505 (2009).
- [193] M. Paulsson, F. Zahid, and S. Datta, *Resistance of a molecule* (2003).
- [194] S. Datta, *Electrical resistance: an atomistic view*, *Nanotechnology* **15**, 433 (2004).

Mechanically controlled break junction measurements

Two molecules were measured in a mechanically controlled break junction (MCBJ) in liquid environment. The MCBJ system used herein is described in detail in [191]. The molecules were especially designed to have a large coupling to the gold electrodes via the π -system of the basket-like endgroups. They were synthesized in the group of Prof. Rainer Herges at the University of Kiel and are shown in Figure A.1 left panel.

0.25 mM solutions of the molecules in tetrahydrofuran/mesitylene (1 : 4) were prepared for both molecules. The solution of the (TATA)²-BP showed a light pink color which changed to an intense pink over time. This was further investigated using UV-Vis spectroscopy. For this a 8.33 μ M solution in tetrahydrofuran/mesitylene (1 : 4) was measured with a UV-1800 Shimadzu spectrophotometer. A spectrum

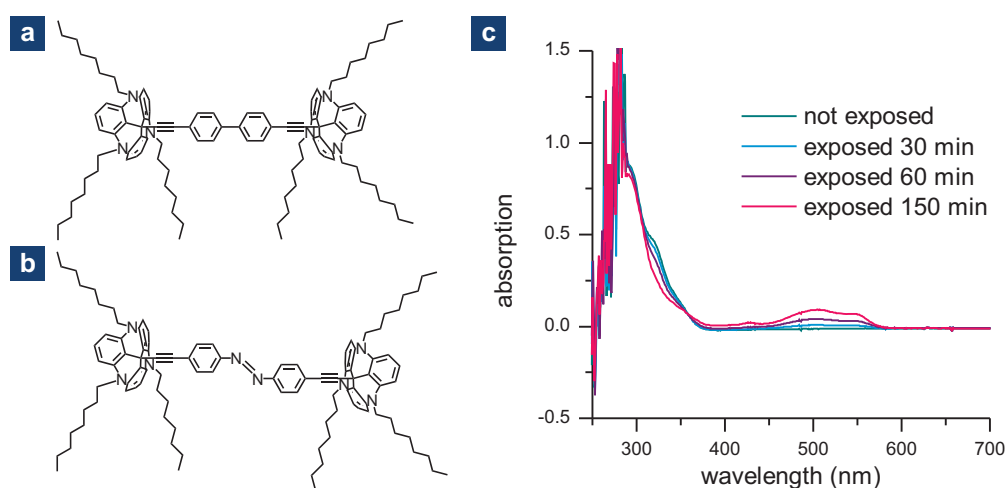


FIGURE A.1.: Structure of the **a** (TATA)²-BP and **b** (TATA)²-AZO molecules. Structure of the **c** UV-Vis spectra of the compound shown in Structure of the **a** before and after UV-irradiation.

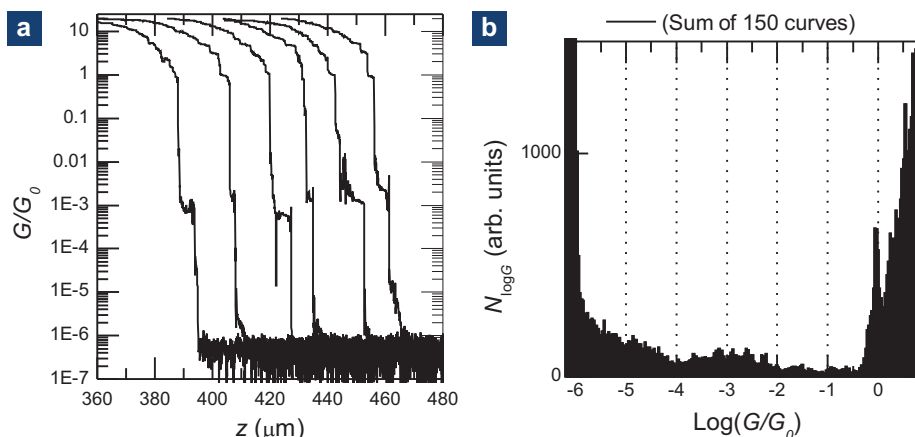


FIGURE A.2.: MCBJ measurements of the $(\text{TATA})^2\text{-BP}$ molecule. **a** Examples of conductance versus distance traces showing small plateaus at $\approx 10^{-3}G_0$. **b** 1D conductance histogram composed of 150 traces.

was recorded every hour for one day, but no change in the spectrum could be observed. A second measurement series was performed to test if the compound is UV-sensitive. For this the solution was irradiated with a UV-lamp (365 nm) for half an hour between recording the spectra. The absorption maximum was at 290 nm for all measurements. Before UV-irradiation a shoulder at 330 nm was present. With prolonged UV-irradiation this shoulder disappeared and a broad feature at 500 nm appeared. The spectra are shown in Figure A.1 right panel. However, it is not clear how the structure of the molecule changes with UV-irradiation. The $(\text{TATA})^2\text{-AZO}$ solution has a yellow color which did not change with time.

Conductance versus distance traces (compare with chapter 2) were recorded. Note that z does not correspond directly to the electrode separation here and a conversion factor of $\approx 10^{-5}$ has to be taken into account [191]. To perform the measurements, the junction is closed to $20 G_0$ with a velocity of $31.2 \mu\text{m/s}$ or $5 \mu\text{m/s}$ and a voltage of 0.1 V was applied. No plateaus in the conductance versus distance traces are observed for the $(\text{TATA})^2\text{-BP}$ molecule at both closing speeds. Thus also no peaks appear in the one-dimensional conductance histograms. If the measurement is performed after the exposure of the molecule to UV-light, short plateaus at $\approx 10^{-3}G_0$ are observed in $\approx 10\%$ of the curves (some examples are shown in Figure A.2 left panel). In the 1D conductance histogram only a slight peak is observed at the same value (see Figure A.2 right panel), as the number of plateaus is small. The measurements of the $(\text{TATA})^2\text{-AZO}$ did neither lead to plateaus nor to a conductance peak in the histogram.

Unfortunately the molecules do not couple well enough to the electrodes to perform stable measurements.

Experimental details of the graphene transfer

In this chapter we describe the experimental conditions used for transferring the graphene after CVD growth from the Cu foil to an insulating substrate. A brief description of the process is described in [section 5.3](#). Our process is based on the work of Li et al. [[125](#)]. The parameters for the process used at present are summarized in [Table B.1](#)

1. A PMMA (molecular weight: 50 kD, speed: 4000 rpm, ramp: 4 s, duration: 40 s) layer of 300 nm thickness is used as supporting layer during transfer. Note that no curing is performed after the spin coating, but the polymer layer is dried under ambient conditions. Heavier PMMA (molecular weight: 950 kD) and Formvar were tested as transfer layers as well, but the cleanest results were achieved with the 50 kD PMMA.
2. To achieve a uniform wet etching of the copper, the graphene layer on the backside of the Cu foil has to be removed. For this we use an argon/oxygen (Ar/O₂) plasma in a reactive ion etcher (base pressure: $5 \cdot 10^{-5}$ mTorr, etching pressure: 250 mTorr, Ar: 22.2 sccm, O₂: 8 sccm, power: 30 W, duration: 30 s).
3. The PMMA/graphene/Cu stack is then placed on the Cu etchant, where it floats until the Cu is etched away fully. As etchant we use either 0.1 M iron nitrate (Fe(NO₃)₃) dissolved in water (H₂O) or 0.1 M aluminum persulfate ((NH₄)₂S₂O₈) in H₂O. Etching of a 25 μm thick Cu foil in the Fe(NO₃)₃ solution takes ≈ 12 h and ≈ 4 h in the (NH₄)₂S₂O₈ solution. As the etching in (NH₄)₂S₂O₈ seemed to be a bit cleaner and is faster, it is preferred. After the Cu is etched the PMMA/graphene stack is washed in several water baths. This is done by either exchanging the etchant through deionized water with a syringe or transferring the stack to clean water with a spoon.
4. Then the floating PMMA/graphene stack can be either fished with a substrate or the substrate is placed below and the water is gently removed. As the

supporting PMMA layer is thin, the stack has to be handled with care. We use doped Si wafers with a 300 nm thick thermal SiO₂ layer. The specific thickness of the oxide allows the visualization of monolayer graphene [139, 140]. Prior to the transfer, the wafer pieces were cleaned by sonication in acetone and isopropanol followed by a Ar/O₂ plasma (base pressure: $5 \cdot 10^{-5}$ mTorr, etching pressure: 25 mTorr, Ar: 22.2 sccm, O₂: 8 sccm, power: 30 W, duration: 150 s).

5. The sample is dried over night in ambient conditions. As a last step, the PMMA layer has to be dissolved. For this the sample is immersed into 50 °C warm acetone and left there for ≈ 1 h, the sample is then rinsed with acetone and isopropanol followed by blow drying with nitrogen N₂. To relax the PMMA it was proposed to add a drop of PMMA or heat the sample above the PMMA glass transition temperature prior to dissolving it [125, 133].

Transfer yield is only $\approx 50\%$. In the other cases the graphene is not clean enough over a larger area or does show a lot of holes. In some cases the surface cleanliness could be enhanced through annealing in hydrogen flow (20 sccm, 0.03 mbar, 150 °C).

1. spin coating of polymer layer	PMMA 50 kD, 300 nm (speed: 4000 rpm, ramp: 4 s, duration: 40 s)
2. etching graphene on backside of Cu foil	Ar/O ₂ plasma (base pressure: $5 \cdot 10^{-5}$ mTorr, etching pressure: 250 mTorr, Ar: 22.2 sccm, O ₂ : 8 sccm, power: 30 W, duration: 30 s)
3. etching Cu foil and subsequent washing in H ₂ O bath	0.1 M (NH ₄) ₂ S ₂ O ₈ in H ₂ O, ca. 4 h (for 25 μ m thick Cu foil)
4. transfer to Si/SiO ₂ wafer	oxide thickness: 300 nm, wafer cleaning: Ar/O ₂ plasma, base pressure: $5 \cdot 10^{-5}$ mTorr, etching pressure: 25 mTorr, Ar: 22.2 sccm, O ₂ : 8 sccm, power: 30 W, duration: 150 s
5. dry sample and remove PMMA	drying: in ambient conditions over night, removing PMMA: immersion in 50 °C warm acetone for 1 h, rinse with 2-propanol, dry in N ₂ flow

TABLE B.1.: Summary of the experimental details of the different transfer steps.

Experimental setup for Raman spectroscopy

Herein we describe the experimental details of the Raman microscope used for all the measurements shown in this thesis. We also describe the process used to correct for the focus drift which occur in long lasting measurements.

The experimental apparatus for Raman spectroscopy consists of a light source, sample optics, a spectral dispersion device and spectral acquisition. Phase coherence and monochromaticity make lasers the preferred light source for Raman spectroscopy. The role of the sample optics is to focus the light on the sample and to collect the scattered light. A confocal microscope offers a good lateral resolution for this purpose. The spectral dispersion device segments the scattered light according to its wavelength. For this, a diffraction grating or an interferometer can be used. In the spectral acquisition the spectrum is then recorded and translated to an electric signal. Nowadays, mainly CCD chips serve this purpose.

Our measurement setup

We use a WITec alpha300r confocal Raman microscope together with an Olympus MPlanFL 100x objective for characterization and an Olympus LMPlanIR 50x or an Zeiss EC Epiplan-Neofluar 50x long working distance objective for combined optical and electrical measurements. The laser is a frequency-doubled Nd:YAG laser with a wavelength of 532 nm. If not mentioned otherwise the laser power was set to 2 mW. The system is equipped with a UHTS 300 spectrometer with two grating options (600 and 1800 grooves per mm) and a coolable CCD detector with a resolution of 1024 x 127 pixel and peak quantum efficiency of 95%. A piezoelectric and a motorized scan stage allow the scanning of the surface. To externally heat the samples, and combine optical with electrical measurements a Linkam HFS600E-PB4 probe stage is available.

Correction of the focus drift

In Raman measurements of CVD graphene on a Si/SiO₂ wafer, we observed a shift of the peak positions while moving the microscope in z -direction, perpendicular to the sample surface (Figure C.1 blue solid squares). In section 6.3 we saw that heating changes the peak positions. Thus this shift could be due to laser induced heating, where the heat induced in the graphene changes with the focus position. For measurements conducted over times longer than 30 min (where the drift in the z -direction can be up to a few hundred nm), we had to correct for this effect. As an example we take the 2D-band of graphene (see also section 6.2), as shown in Figure C.1. This measurement was performed by first focusing on the graphene and setting this position as $z_F = 0$. Then the microscope was moved out of focus and a Raman spectrum was recorded every 100 nm in z -direction. The slight difference between $z_F = 0$ and the optimal focus position z_0 (where the peak area is at the maximum, the area is plotted as turquoise open squares) could come from inaccuracies in the system, drift or not optimal focusing. The observed peak shift (blue solid squares) follows a Lorentzian (black dashed line). The change of the area of the 2D-band can be used to calculate the actual focus position. The dependence of the peak area on the focus can be derived from the intensity of a Gaussian beam

$$I(z) = \frac{I_0}{1 + \left(\frac{z_F - z_0}{z_R}\right)^2}, \quad (\text{C.1})$$

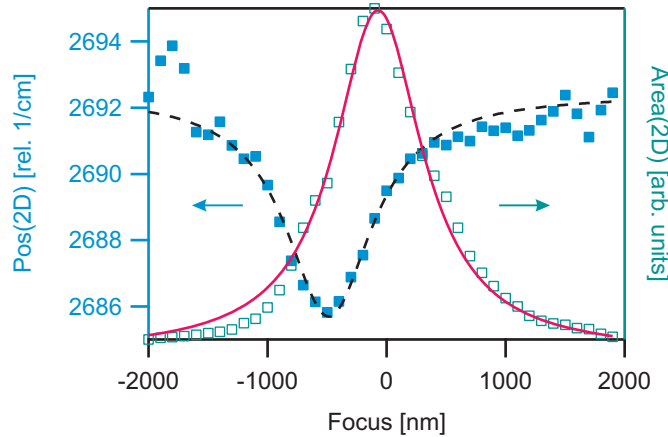


FIGURE C.1.: Dependence of the graphene 2D peak position (blue solid squares) and area (turquoise open squares) on the focus position. A Lorentzian fit to the peak position and a fit of equation C.1 (black dashed line) are shown as well. [150] Reproduced by permission of The Royal Society of Chemistry (RSC)

where I_0 is the intensity at optimal focus, z_0 is the position of the optimal focus, z_F is the actual focus position and z_R is the distance from the optimal focus where only the half intensity of the beam is left [146]. The area of the 2D-peak with changing focus and a fit to Equation C.1 are shown in Figure C.1 (turquoise open squares, pink solid line). A possible explanation for the change in peak position with changing focus could be laser induced heating, which would shift the the 2D-band to lower wavenumber (see section 6.3). Note that the ideal focus point (area is maximal) does not correspond to the point of lowest 2D-phonon energy. This would mean that the laser induced heating is most efficient if the focus point lies below the graphene surface and heat can also be absorbed via the substrate.

Capacitance measurements

The goal of these experiments is to determine the quantum capacitance C_q of graphene. One possibility to measure it are gate dependent capacitance measurements. For this a system is needed where a capacitor with a capacitance C is in series to the graphene. As only C_q is gate dependent it can be directly deduced from measuring the capacitance of the system versus a gate [192]. This is only possible if $C \geq C_q$ as otherwise the measurement will be dominated by the smaller C . We decided to try the measurements using capacitors formed from gold-molecule-graphene stacks, as we expect a large capacitance for such a system.

Capacitors are fabricated using gold as the bottom electrode, a hexadecanethiol SAM as insulator and graphene grown by CVD on Cu as top electrode. The gold electrodes were fabricated using standard UV lithography (see appendix I). The SAM is formed using a 1 mM solution of hexadecanethiol in ethanol and immersing the sample into the solution over night at 50 °C. The sample is rinsed in ethanol and dried. CVD graphene is grown and transferred onto the sample using our standard

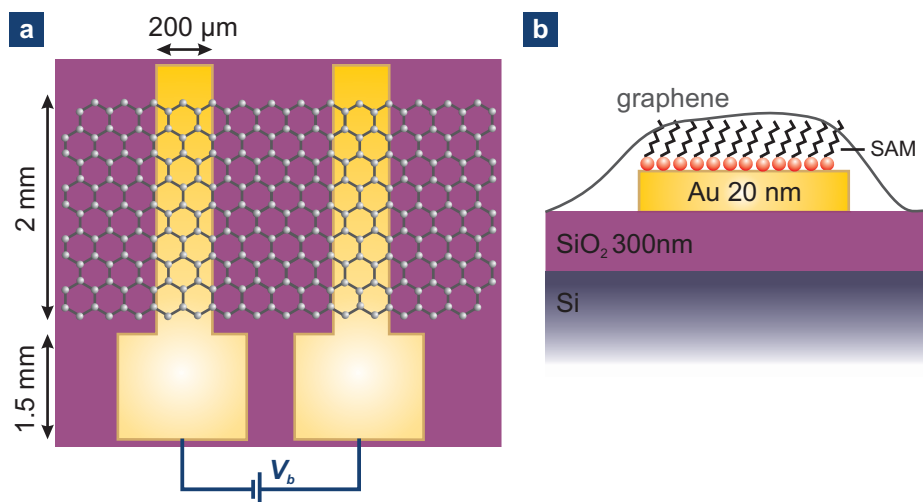


FIGURE D.1.: Schematic **a** top and **b** side view of a graphene capacitance device.

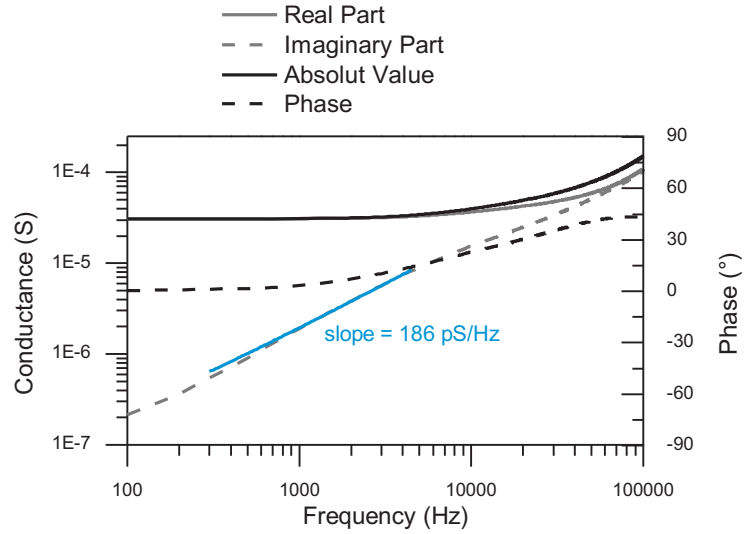


FIGURE D.2.: Frequency dependent impedance measurement performed on a graphene capacitor sample.

protocol (see [chapter 5](#)). A schematic top and side view of the device are shown in [Figure D.1](#).

A device consists of two capacitors in series and has a typical resistance between $10\text{ k}\Omega$ and $40\text{ k}\Omega$. Frequency dependent impedance measurements are performed to measure the capacitance of the device. They were done in ambient conditions at bias voltage of 1 mV . An example of such a measurement is shown in [Figure D.2](#). For the device shown, the capacitance of both capacitors in series is $\approx 186\text{ pF}$. Measuring several devices we obtain values for the capacitance normalized over the area, in the order of $C = 0.1\text{ }\mu\text{Fcm}^{-2}$. The quantum capacitance of graphene was reported as $C_q \approx 10\text{ }\mu\text{Fcm}^{-2}$ [[192](#)], which is still two orders of magnitude bigger. To increase C in our system we also prepared samples with dodecanethiol as the insulating layer. As this molecule is shorter, C should increase. Unfortunately we were not able to fabricate working devices with dodecanethiol as shortcuts between the graphene and the gold electrode were present. In conclusion, this system is not well suited to measure the quantum capacitance of graphene as originally intended.

Cutting graphene with a He-FIB

Helium-ion-beam lithography (HIBL) allows direct writing on graphene with a high resolution [172]. Thus we wanted to test if the system serves as a method to directly pattern graphene electrodes separated by less than 5 nm to be used in molecular electronics. The main challenge is to fabricate these electrodes in a reproducible process with a high yield (see as well [chapter 8](#)).

We performed tests with the ORION® Helium Ion Microscope (HIM, Zeiss, Germany) together with Dr. Ivan Shorubalko at the EMPA in Dübendorf. Several test structures were written and the best resolution for a single pixel line was found to be 5 – 10 nm at a dose of 2.0 nCcm^{-1} (see [Figure E.1](#) top left panel). It was not possible to define the width of the line more exact, as imaging with the HIM destroys the graphene even at low energies and fast scanning speeds (dose of $\approx 0.1 \text{ mCcm}^{-2}$). To be able to investigate the properties of the exposed graphene, squares of $2 \mu\text{m} \times 2 \mu\text{m}$ were exposed with different doses (from 1 mCcm^{-2} to 18 mCcm^{-2}). In optical microscopy only areas exposed with a high dose are distinguishable from non exposed parts of the graphene ([Figure E.1](#) top middle panel). In scanning electron microscopy (SEM) all squares show a contrast to non-exposed graphene ([Figure E.1](#) top right panel). To further investigate the effect of HIBL, Raman spectroscopy (see also [chapter 6](#)) was performed. [Figure E.1](#) lower panel shows the Raman spectra for graphene not exposed to the helium-ion beam, graphene imaged at low energies with the HIM and graphene exposed to different doses of HIBL. The G-band broadens with increasing dose, whereas the 2D-band disappears already at low doses. The D-band increases at low doses and disappears at higher doses. To better visualize these effects, Raman maps of the D-band and the broadened G-band (1450 – 1610 rel. 1/cm) are shown in [Figure E.1](#) lower panel. The enhancement of the D-band at lower doses indicates that defects are created in the graphene. For higher doses the D-band disappears completely in the exposed regions and a higher D-band density is observed around the exposed region. This means that the graphene is destroyed and the graphene in the neighboring areas becomes defective. The increase in width and intensity of the G-band at higher doses indicates that the graphene is not removed in the exposed regions but transformed into amorphous carbon, which does not exhibit a D- or 2D-band but shows a broad G-band [109].

We did not manage to achieve the resolution needed to fabricate graphene electrodes for molecular electronics with HIBL. However, high resolution HIBL on graphene and CNTs has been demonstrated recently [26, 173]

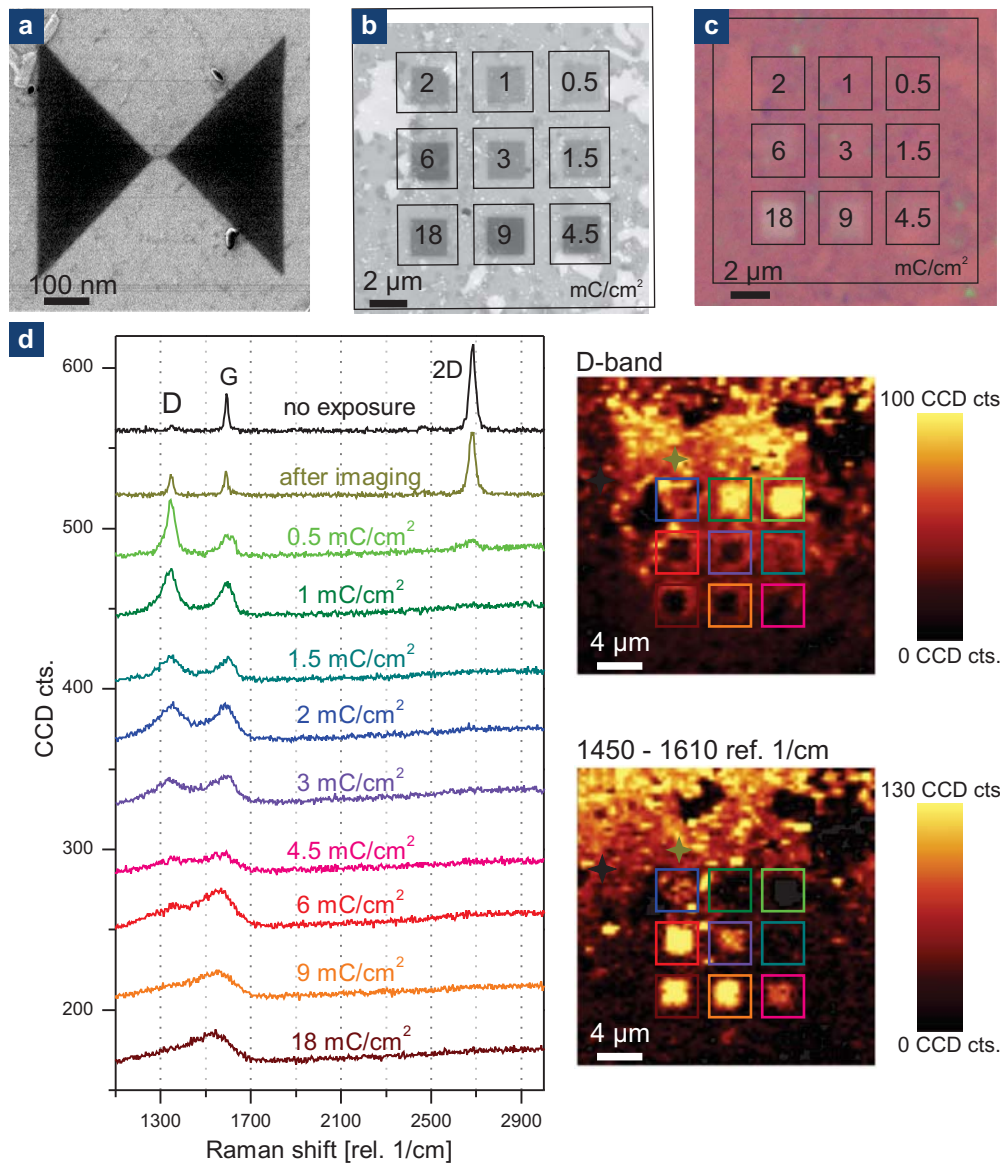


FIGURE E.1.: **a** helium-ion-beam image of a single pixel line written with HIBL. **b** Optical and **c** SEM image of graphene exposed to different doses of a helium-ion-beam. **d** Raman spectra of graphene exposed to HIBL at different doses. The maps on the right show the sum of the D-band and the broadened G-band (1450 – 1610 rel. 1/cm).

Graphene fusion and switching

As briefly mentioned in [section 9.1](#) for some electroburned graphene samples the conductance suddenly increase by several orders of magnitude while measuring $I - V$ characteristics. In this chapter we will further investigate this phenomenon.

When measuring the $I - V$ characteristics after EB at high voltages (> 5 V) approximately 20% of the devices exhibited a sudden increase in conductance. Their resistance decreased from $10^8 - 10^{11} \Omega$ to $10^4 - 10^6 \Omega$. Some of the devices even showed the same ambipolar behavior as graphene when measuring I versus V_g traces. An example is shown in [Figure F.1](#) left panel. The mobility deduced from a fit to the steepest slope and [Equation 4.6](#) is $\mu = 79.5 \text{ cm}^2 \text{ V}^{-1} \text{ s}^{-1}$. This is ten times smaller than the typical values for GFETs before EB. We think that possibly the graphene reformed as was shown by [\[182\]](#), but with defects which lower the mobility. We tried to burn these fused graphene junctions by again applying the EB procedure. We could not measure a tunneling current ($< 10 \text{ pA}$) for any of these samples.

A few of these devices showed switching between two conductance states when

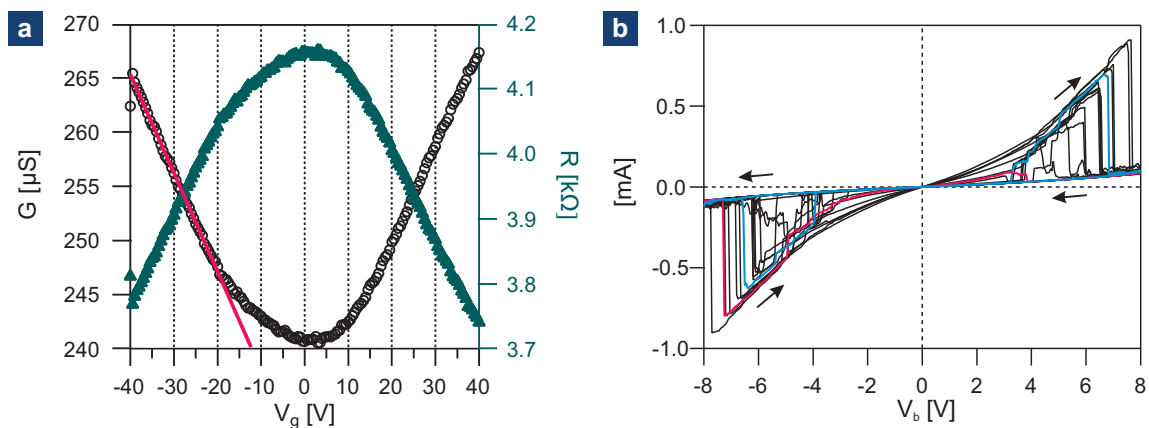


FIGURE F.1.: **a** Conductance and resistance of a fused graphene junction versus gate voltage. **b** $I - V$ curves of a device showing switching behavior after the reformation of the graphene in the junction.

performing $I - V$ sweeps. An example of such $I - V$ traces is shown in [Figure F.1](#). This figure shows 14 curves recorded subsequently on the same device. Two example curves are highlighted. For this example the two conductance states are at $17\text{ k}\Omega$ and $164\text{ k}\Omega$ (linear fit to $\pm 1\text{ V}$). But also conductance states between these values were observed. For most of the curves the junction starts in the low conductance state when starting at a highly negative V_b and switches to the high conductance state at a certain V_b . The junction stays in the high conductance state until V_b is large and then it switches back to the lower state. The high conductance state seems to be less stable than the low conductance state and the junction sometimes switches back to the low conductance state before high values of V_b are reached. The voltage at which the conductance state switches can vary over a large range and is not symmetric for positive and negative voltages. One idea to explain the switching would be an overlapping graphene area, where the overlap is changed through the high electric field applied or through thermal expansion and retraction. To really identify the mechanism behind or control the switching, further investigations are needed.

Level spectrum of the OPE Rod 1 molecule

Absorption and emission data of the OPE Rod 1 compound (for the structure see [Figure 9.3](#)) were recorded in acetonitrile using a UV-1800 Shimadzu spectrophotometer and a Horiba Jobin Yvon Fluoromax 4 fluorimeter, respectively. The energy of the zero-zero singlet transition (E_{0-0}) was calculated with the wavelength at the intersection (λ_{inter}) of the normalized emission and absorption spectra with the equation $E_{0-0} = \frac{hc}{\lambda_{inter}}$, where h is the Planck constant, c is the speed of light. Redox potentials $V_{+/0}$ of the OPE Rod 1 in solution were recorded in 0.1 M $(\text{Bu}_4\text{N})\text{PF}_6$ in acetonitrile as the supporting electrolyte with an Autolab PGSTAT 302N potentiostat with a saturated calomel electrode as reference. Values were calibrated against an external standard ferrocenium tetrafluoroborate ($\text{Fc}(\text{Cp})_2^{+/0}$). These measurements were performed by Dr. Loïc Le Pleux in the group of Prof. Marcel Mayor at the University of Basel.

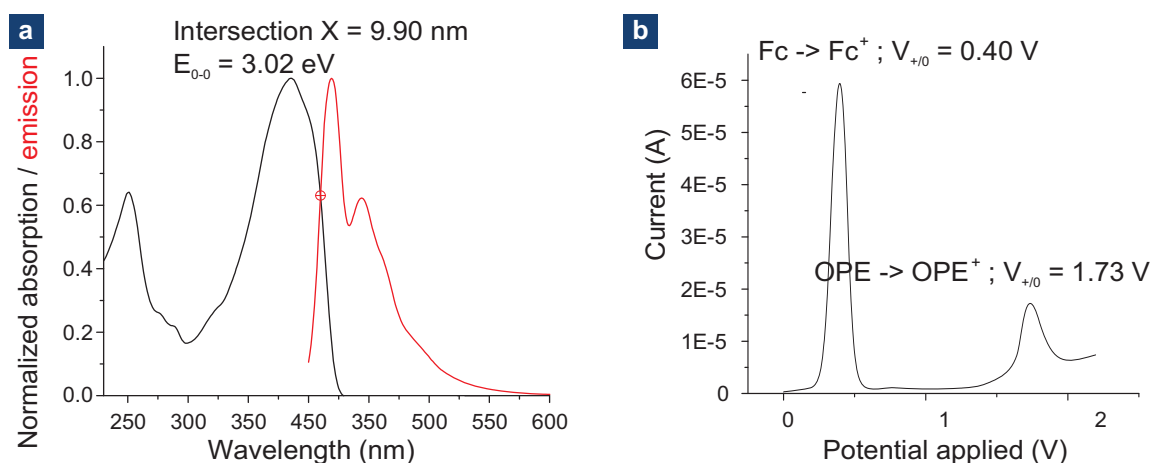


FIGURE G.1.: **a** Structure and absorption and emission spectra of the OPE Rod 1 molecule. **b** Redox potentials of the OPE Rod 1 molecule measured in solution (acetonitrile).

The zero-zero singlet transition gives the energy spacing between the HOMO and LUMO. In this case the free molecule has a HOMO-LUMO gap of 3.02 eV. The position of the levels can be calculated from the redox potential, where $E_{HOMO} = -e(V_{OPE^+/OPE} - V_{Fc^+/Fc}) + 5.10 \text{ eV} = -6.43 \text{ eV}$, where $V_{OPE^+/OPE}$ and $V_{Fc^+/Fc}$ are the redox potentials of $\text{Fe}(\text{Cp}_2^{+/0})$ and the OPE Rod 1 respectively. The 5.1 eV is the calibrated potential of the reference electrode. The level position of the LUMO is then given by $E_{LUMO} = E_{HOMO} + E_{0-0} = -3.41 \text{ eV}$. For an electrically contacted molecule, the positions of the levels could be altered due to interactions with the electrode (see [section 1.3](#)).

Molecular I-V curves

In [section 9.2](#) we demonstrated that we can contact molecules within graphene gaps. In this chapter we show $I - V$ curves on additional devices exhibiting the same step-like features as the device discussed in [section 9.2](#). Further we will briefly discuss a model with which this behavior can be reproduced.

[Figure H.1](#) shows $I - V$ curves of four different graphene devices. For all of them the tunneling curves after electroburning (averaged over 40 curves), after rinsing with solvent (averaged over 40 curves) and after depositing the molecules (single curves plus average) are given. The molecule and the procedure to deposit it is the same as described in [section 9.2](#). For three of the four devices presented the conductance is enhanced after depositing the molecules, whereas the device in the top right panel only shows a change in the shape of the $I - V$ curves, but no increase in conductance. The magnitude of the current observed at a distinct voltage can vary from junction to junction as seen best on the devices shown in the top panels. All junctions show a step-like feature in the positive bias (V_b) region, but the position of the step varies from 0.3 V to 1.5 V. For the device in the lower left panel not all $I - V$ curves which exhibit the step-like feature and its behavior can change between two steps. A similar behavior was also observed for other devices. We think that in this device the molecule is not bound to the graphene in a stable way. For devices where no molecules were deposited (> 100 gaps were investigated) we never observed similar behavior. Thus we attribute these features to transport through the molecules.

Step-like features in molecular $I - V$ curves have been reported before [[49](#), [50](#)]. In Ref. [[49](#)] they model their data by using a sequential tunneling model based on elastic scattering quantum chemistry. They treat the molecule as a quantum dot with a weak coupling to the electrodes and discrete energy levels.

We will now attempt to qualitatively explain our data by a simple toy model as described in Refs. [[193](#), [194](#)]. In this model a molecular junction is described as a single level (either the HOMO or the LUMO) coupled to the leads by two tunnel barriers as schematically depicted in the inset of [Figure H.2](#). In this simple picture there are two electrodes with the chemical potentials μ_L and μ_R , and they are biased, such that the molecular level (at energy ε) lies between them. The transfer rate for an electron from the molecule to the contacts is given by Γ_L/\hbar and Γ_R/\hbar , where $\Gamma_{L,R}$

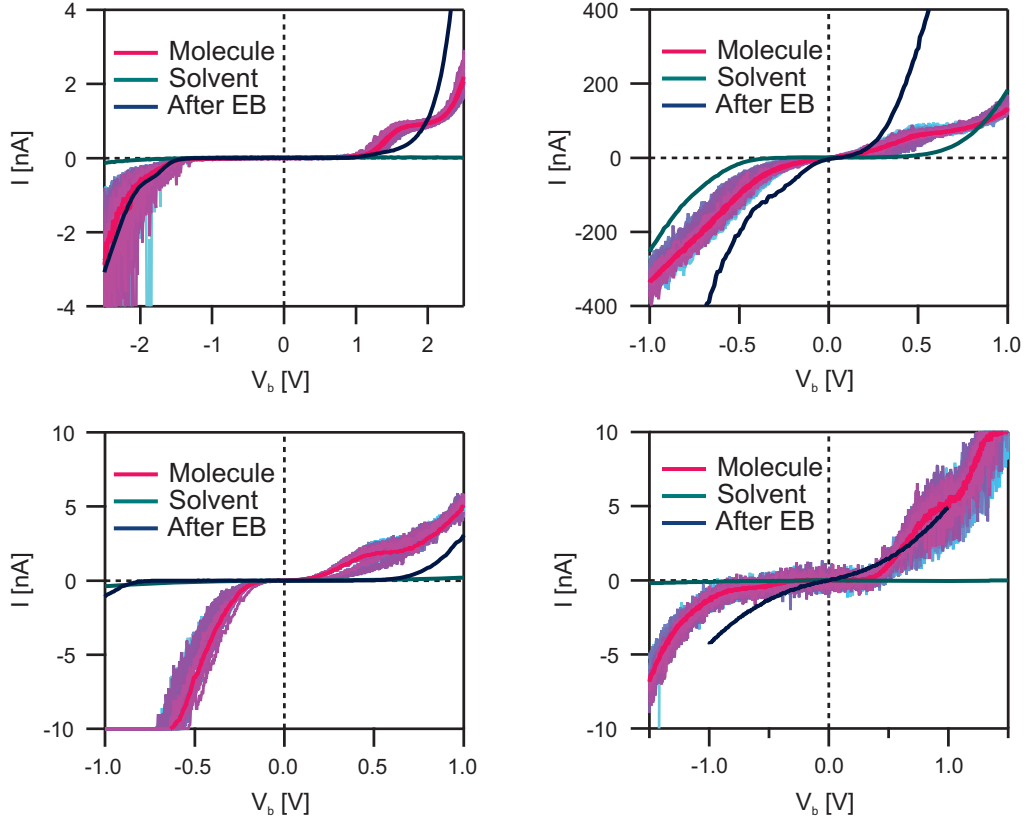


FIGURE H.1.: $I - V$ curve for four different graphene devices. $I - V$ curves averaged over 40 subsequently measured curves after EB and after rinsing with solvent are shown in dark blue and turquoise respectively. Single $I - V$ curves after applying the molecules and an average of the are shown in pink. All devices show step-like features in the molecular $I - V$ s.

is the coupling and \hbar is the Planck constant. The current I from the left to the right electrode is then given by

$$I = \frac{2e}{\hbar} \frac{\Gamma_L \Gamma_R}{\Gamma_L + \Gamma_R} [f_L(\varepsilon, \mu_L) - f_R(\varepsilon, \mu_R)], \quad (\text{H.1})$$

where f_L and f_R are the Fermi distribution of the left and the right electrode respectively. The number of electrons occupying the level N is

$$N = 2 \frac{\Gamma_L f(\varepsilon, \mu_L) + \Gamma_R f(\varepsilon, \mu_R)}{\Gamma_L + \Gamma_R}. \quad (\text{H.2})$$

We now want to include charging effects, which are due to the change in N with

respect to the equilibrium. Therefore we introduce the charging potential $U_{SFC} = U(N - 2f(\varepsilon_0, E_F))$, where U is the charging potential prefactor, ε_0 is the level position in equilibrium and E_F is the Fermi energy. This potential shifts the level according to $\varepsilon = \varepsilon_0 + U_{SFC}$. As the potential depends on N which itself depends on ε , an iterative self-consistent procedure can be used to calculate ε . In the case where $\Gamma_{L,R}$ and the thermal energy is smaller than U coulomb blockade can occur. This means that if an electron is located on the level, the next electron needs a higher energy to be added to the level due to coulomb-coulomb interaction. A further effect is the broadening of ε due to the coupling of the molecular level to the electrodes (see also [section 1.3](#)). This leads to a Lorentzian density of states $D(E)$:

$$D(E) = \frac{1}{2\pi} \frac{\Gamma_L + \Gamma_R}{(E - \varepsilon)^2 + ((\Gamma_L + \Gamma_R)/2)^2}. \quad (\text{H.3})$$

Introducing [Equation H.3](#) into [Equation H.1](#) gives

$$I = \frac{2e}{\hbar} \int_{-\infty}^{\infty} D(E) \frac{\Gamma_L \Gamma_R}{\Gamma_L + \Gamma_R} [f_L(E, \mu_L) - f_R(E, \mu_R)] dE. \quad (\text{H.4})$$

To simulate the behavior observed for the $I - V$ curves in our preliminary results, we can use this model, described as the *Unrestricted Broadened One-Level Model* in Ref. [193]. For this we assume that the voltage drops symmetrically over both barriers. The MATLAB[®] code is given in Ref. [193]. A curve for which we used $\varepsilon = -3.4$ eV (which is approximately the LUMO of our molecule), $E_F = -3.9$ eV, $\Gamma_L = 0.006$ eV, $\Gamma_R = 0.06$ eV and $U = 0.3$ eV is shown in [Figure H.2](#). The shape of our curves is well reproduced, however the current is at least one to three orders of magnitude too high. This could come from overestimating the coupling strength, however modeling I for small Γ is challenging, as too many iterations have to be performed until a self-consistent ε was found. The charging energy is in the similar range as for previously reported values [49].

In conclusion, the OPE Rod 1 molecules contacted within the graphene gaps exhibit reproducible step-like features in the $I - V$ curves. We can use the *Unrestricted Broadened One-Level Model* of Ref [193] to qualitatively explain the shape of the $I - V$ curves obtained. In this model, transport through a single level is assumed and level broadening as well as coulomb blockade are included. Without including coulomb blockade, only one step in current would be expected, as after the crossing of the level no additional states would be present. The second increase in current, observed in our junctions, thus can be explained by coulomb blockade. The asymmetry in the transport properties is due to a very asymmetric coupling of the molecule to the leads. To further test the mechanism behind the current steps, gate dependent measurements, which allow to shift the energy level of the molecule, would be needed.

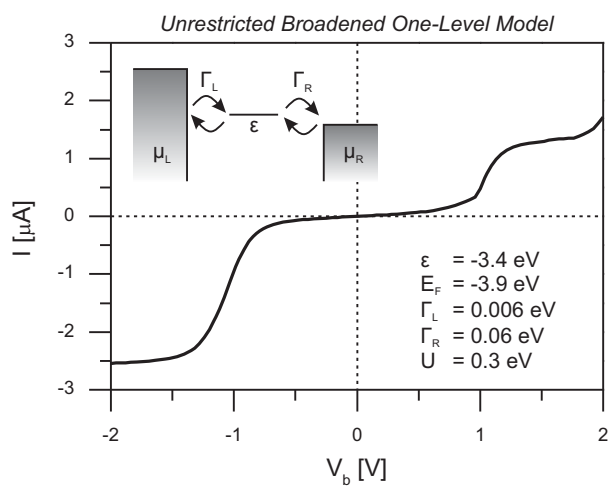


FIGURE H.2.: Modeled I – V curve showing step-like behavior using the *Unrestricted Broadened One-Level Model* as described in Ref. [193]. The inset shows a schematic representation of the one-level model.

Fabrication protocols

Wafer characteristics

Substrate material	highly doped Si
Dopant	p, boron
Resistivity	$\approx 10 \Omega\text{cm}$
Capping layer	300 nm thermally grown SiO_2

Wafer cleaning

- Sonicate for 10 min in acetone
- Sonicate for 10 min in 2-propanol, blow-dry
- 30 min UV-ozone cleaning (Model 42,220, Jelight Company, USA)

UV lithography

- Pre-bake sample for 30 min on hotplate at 200°C
- Spin coating UV resist (ma-N 415, micro resist technology GmbH, Germany) at 3000 rpm, 3 s ramp, 30 s spin (layer $\approx 1.5 \mu\text{m}$ thick)
- Bake for 90 s on hotplate at 95°C
- Exposure in UV mask aligner (MJB4, Süss MicroTec, Germany) for 8 s (365 nm, $33 \text{ mW}/\text{cm}^2$, hard contact 6 s)
- Development for ca. 80 s in ma-D 332s (micro resist technology GmbH), rinse with H_2O , blow-dry

E-beam lithography

- Spin coating e-beam resist (ZEP 520A, Zeon Co., Japan) at 4000 rpm, 4 s ramp, 40 s spin (layer \approx 350 nm thick)
- Bake for 180 s on hotplate at 180 ° C
- Exposure to e-beam (Zeiss Supra 40, Zeiss, Germany) with an extraction voltage of 10 kV and a dose of 34 $\mu\text{C}/\text{cm}^2$
- Development for ca. 60 s in amyl acetate, stop in methyl isobutyl ketone for 10 s, rinse in 2-propanol, blow-dry

Graphene etching

Reactive ion etching in Oxford Instruments Plasmalab^{80 Plus}: Base pressure $5 \cdot 10^{-5}$ mbar, process pressure 250 mTorr, Ar flow: 22.2 sccm, O₂ flow: 8 sccm, power: 30 W, time: 30 s

Metallisation

Titanium and gold were evaporated with an e-gun in a Sharon Vacuum (MA, USA) system. The vacuum during evaporation was $< 10^{-5}$ mTorr and the rates were kept at 1 Å/s.

Lift-off

For samples prepared with UV lithography lift-off is done by immersing the sample in acetone (50 ° C) for 30 min minimum, rinsing in 2-propanol, blow-dry.

For samples prepared with e-beam lithography lift off is done by immersing the sample in N-Methyl-2-pyrrolidon (70 ° C) for 10 min, immersing into acetone (50 ° C) for 30 min minimum, rinsing in 2-propanol, blow-dry.

Curriculum Vitae

Cornelia Nef

Born 22 September 1986 in Herisau (AR, Switzerland)

Education

- 2010 - 2014 PhD in experimental Physics at the University of Basel
PhD thesis in the group of Prof. C. Schönenberger and PD M. Calame: "Contacting strategies in molecular electronics"
- 2008 - 2010 Master in nanosciences major physics at the University of Basel
Master thesis in the group of Prof. C. Schönenberger: "Force spectroscopy of and charge transport in molecular junctions"
Project thesis in the group of Prof. U. Aebi: "Investigation of the nanomechanical properties of mouse myoblasts by IT-AFM"
Project thesis in the group of Prof. B. B. Nielsen (Århus University, Denmark): "Photoluminescence of a silicon nanocrystal monolayer"
- 2005 - 2008 Bachelor in nanosciences at the University of Basel
- 1999 - 2005 Matura at the Gymnasium St. Antonius Appenzell

Positions and professional experience

- 2010 - 2014 Teaching assistant for physics at the University of Basel
- 07 - 08 / 2006 Internship in the Advanced Fibers group at the EMPA St. Gallen

Awards

Deutsche Physikerinnentagung 2010 Price for the best poster presentation

Publication list

Publications in journals

S. Bouvron, R. Maurand, A. Graf, P. Erler, L. Gagnaniello, D. Wiedemann, C. Engesser, C. Nef, W. Fu, C. Schönenberger, F. Pauly, and Mikhail Fonin, *Gate-controlled shift of molecular orbitals in a scanning tunneling microscope*, submitted

C. Nef, L. Pósa, P. Makk, W. Fu, A. Halbritter, C. Schönenberger, and M. Calame, *High-yield fabrication of nm-sized gaps in monolayer CVD graphene*, *Nanoscale* **6**, 7249 (2014)

W. Fu, C. Nef, A. Tarasov, M. Wipf, R. Stoop, O. Knopfmacher, M. Weiss, M. Calame, and C. Schönenberger, *High mobility graphene ion-sensitive field-effect transistor by noncovalent functionalization*, *Nanoscale* **5**, 12104 (2013)

B. Eren, T. Glatzel, M. Kisiel, W. Fu, R. Pawlak, U. Gysin, C. Nef, L. Marot, M. Calame, C. Schönenberger, and E. Meyer, *Hydrogen plasma microlithography of graphene supported on a Si/SiO₂ substrate*, *Applied Physics Letters* **102**, 071602 (2013)

C. Nef, P. L. T. M. Frederix, J. Brunner, C. Schönenberger, and M. Calame, *Force-conductance correlation in individual molecular junctions*, *Nanotechnology* **23**, 365201 (2012)

W. Fu, C. Nef, O. Knopfmacher, A. Tarasov, M. Weiss, M. Calame, and C. Schönenberger, *Graphene Transistors are insensitive to pH changes in solution*, *Nano Letters* **11**, 3597 (2011)

Conference proceedings

K. Thodkar, F. Lüönd, F. Overney, C. Nef, M. Calame, and B. Jeanneret, *Ultrahigh quality CVD graphene for electrical quantum metrology*, IEEE Transactions on Instrumentation and Measurement, in preparation

W. Fu, C. Nef, A. Tarasov, M. Wipf, R.L. Stoop, O. Knopfmacher, M. Weiss, M. Calame, and C. Schönenberger, *Sensing with liquid-gated graphene field-effect transistors*, Conference on Nanotechnology (12th IEEE-NANO), pp 1-2 (2012)

Oral presentations

C. Nef, P. L. T. M. Frederix, J. Brunner, L. Pósa, C. Schönenberger, and M. Calame, *New contacting strategies and spectroscopic insight into molecular junctions*, Kick-off meeting European Commission FP7-INT MOLESCO, Madrid, March 31 - April 02, 2014

C. Nef, P. L. T. M. Frederix, J. Brunner, C. Schönenberger, and M. Calame, *Force spectroscopy of and charge transport in molecular junctions*, International Nanoscience Student Conference, Sursee, August 20 -23, 2009

Poster presentations

C. Nef, L. Pósa, W. Fu, P. Makk, A. Halbritter, M. Calame, and C. Schönenberger, *CVD graphene as a versatile material for molecular electronics and sensing*, European Conference on Molecular Electronics, London, September 03 - 07, 2013

C. Nef, W. Fu, M. Weiss, A. Kis, M. Calame, and C. Schönenberger, *Chemical vapor deposition of graphene: growth, transfer and characterization*, International Winterschool on Electronic Properties of Novel Materials, Kirchberg, March 03 - 10, 2012

C. Nef, P. L. T. M. Frederix, J. Brunner, C. Schönenberger, and M. Calame, *Force-conductance correlation in molecular junctions*, European Conference on Molecular Electronics, Barcelona, September 07 - 10, 2011

C. Nef, P. L. T. M. Frederix, J. Brunner, C. Schönenberger, and M. Calame, *Force-conductance correlation in molecular junctions*, 4. Deutsche Physikerinnentagung, Munich, November 04 - 07, 2010

C. Nef, P. L. T. M. Frederix, J. Brunner, C. Schönenberger, and M. Calame, *Force spectroscopy of and charge transport in molecular junctions*, International Conference on Molecular Electronics, Emmetten, January 05 - 09, 2010

Acknowledgments

I am very grateful to Christian Schönenberger and Michel Calame for giving me the opportunity to do a PhD in their group. Their ideas and motivation were always inspiring. Thank you Michel, for giving me freedom and support, both in the right amount. I thank Prof. András Halbritter and Prof. Ralph Krupke for being in my PhD committee and taking the time to read my thesis.

Further I want to express my gratitude to the people with whom I worked together closely: Patrick Frederix, Wangyang Fu, László Pósa and Jan Brunner. We shared many hours in the lab. A special thanks goes to Péter Makk for proofreading my thesis, helping me with various problems and being a good friend while climbing.

I want to acknowledge the people sharing the office with me: Jón Ágústsson, Toni Fröhlich, Oren Knopfmacher, Ralph Stoop, Alexey Tarasov, Kishan Thodkar, Anton Vladyka and Mathias Wipf. They all contributed to lively working days and many discussions about physics and other topics. The climbers and mountaineers in our group made sure I came back to the lab in one piece: Clevin Handschin, Thomas Hasler, Jörg Gramich, Romain Maurand, Jens Schindele and Simon Zihlmann. Not to forget all the other current and former members of the group: Gulibusitan Abulizi, Hagen Aurich, Claire Barrett, Andreas Baumgartner, Kristine Bedner, Matthias Bräuninger, Gábor Fábíán, Frank Freitag, Cezar Harabula, Lukas Hofstetter, Samuel d'Hollosy, Roman Huber, Minkyung Jung, Jan Mayer, Stefan Nau, Vishal Ranjan, Peter Rickhaus, Julia Samm, Veronica Savu, Samuel Vogel and Markus Weiss. As well as all the students who made an internship in our group during my time here. You all made working here so enjoyable!

I thank the groups of Prof. Marcel Mayor and Prof. Rainer Herges for the synthesis of the measured molecules and help in chemistry related questions, Dr. Ivan Shorubalko for performing HIBL and Dr. Monica Schönenberger for her support with AFM issues. I am also grateful to the support from the electronic and mechanical workshop. Especially I want to mention Michael Steinacher, Heinz Breitenstein, Silvester Jakob and Daniel Sacker. Not to forget Barbara Kammermann and Astrid Kalt from the secretary, they had a solution to every paperwork problem.

Mami, Papi and Mo, thank you for supporting me during the last years. I am grateful towards my friends and especially Ruth for always being good company. A special thank you goes to the Nanos, we had a great time! Finally, I thank Bruno for keeping me grounded and always being there for me on the other end of Switzerland.